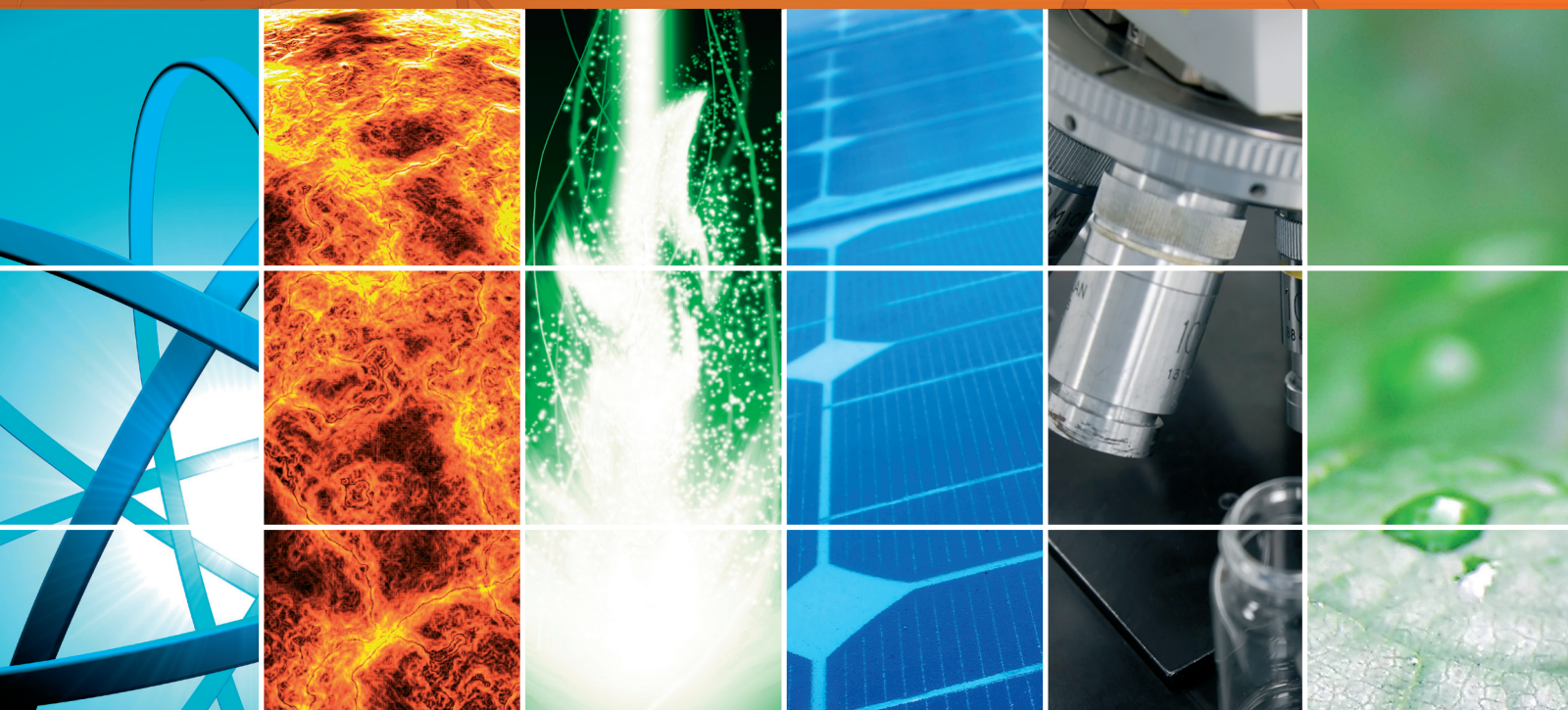


Materials, Designs, Fabrications, and Applications of Organic Electronic Devices

Guest Editors: Jwo-Huei Jou, Ramunas Lygaitis, K. R. Justin Thomas,
and Liang-Sheng Liao





**Materials, Designs, Fabrications,
and Applications of Organic Electronic Devices**

International Journal of Photoenergy

**Materials, Designs, Fabrications,
and Applications of Organic Electronic Devices**

Guest Editors: Jwo-Huei Jou, Ramunas Lygaitis,
K. R. Justin Thomas, and Liang-Sheng Liao



Copyright © 2014 Hindawi Publishing Corporation. All rights reserved.

This is a special issue published in "International Journal of Photoenergy." All articles are open access articles distributed under the Creative Commons Attribution License, which permits unrestricted use, distribution, and reproduction in any medium, provided the original work is properly cited.

Editorial Board

- M. S. Abdel-Mottaleb, Egypt
Xavier Allonas, France
Nicolas Alonso-Vante, France
Wayne A. Anderson, USA
Yanhui Ao, China
Vincenzo Augugliaro, Italy
Detlef W. Bahnemann, Germany
Mohammad A. Behnajady, Iran
Ignazio Renato Bellobono, Italy
Raghu N. Bhattacharya, USA
Pramod H. Borse, India
Gion Calzaferri, Switzerland
Adriana G. Casas, Argentina
Chuncheng Chen, China
Sung Oh Cho, Republic of Korea
Wonyong Choi, Republic of Korea
Věra Cimrová, Czech Republic
Juan M. Coronado, Spain
Ying Dai, China
Vikram Dalal, USA
Dionysios D. Dionysiou, USA
Pingwu Du, China
Mahmoud M. El-Nahass, Egypt
Polycarpos Falaras, Greece
Chris Ferekides, USA
Paolo Fornasiero, Italy
Hermenegildo García, Spain
Elisa Isabel Garcia-Lopez, Italy
Beverley Glass, Australia
M. A. Gondal, Saudi Arabia
Jr-Hau He, Taiwan
Shinya Higashimoto, Japan
Wing-Kei Ho, Hong Kong
Cheuk-Lam Ho, Hong Kong
Fuqiang Huang, China
Adel A. Ismail, Egypt
Chun-Sheng Jiang, USA
Misook Kang, Republic of Korea
Shahed Khan, USA
Jong Hak Kim, Republic of Korea
Sungjee Kim, Republic of Korea
Sun-Jae Kim, Republic of Korea
Cooper H. Langford, Canada
Tae-Woo Lee, Republic of Korea
Lecheng Lei, China
Zhaosheng Li, China
Xinjun Li, China
Yuexiang Li, China
Stefan Lis, Poland
Gongxuan Lu, China
Dongge Ma, China
Niyaz M. Mahmoodi, Iran
Nai Ki Mak, Hong Kong
Rajaram S. Mane, India
Dionissios Mantzavinos, Greece
Ugo Mazzucato, Italy
Sheng Meng, China
Jacek Miller, Poland
Claudio Minero, Italy
Jarugu N. Moorthy, India
Antoni Morawski, Poland
Franca Morazzoni, Italy
Fabrice Morlet-Savary, France
Mohammad Muneer, India
Kun Na, Republic of Korea
Ebinazar B. Namdas, Australia
Maria da Graça Neves, Portugal
Tebello Nyokong, South Africa
Kei Ohkubo, Japan
Haridas Pal, India
Leonidas Palilis, Greece
Leonardo Palmisano, Italy
Ravindra K. Pandey, USA
H. Park, Republic of Korea
David Lee Phillips, Hong Kong
Pierre Pichat, France
Gianluca Li Puma, UK
Xie Quan, China
Tijana Rajh, USA
Peter Robertson, UK
Avigdor Scherz, Israel
Elena Selli, Italy
Ganesh D. Sharma, India
Jinn Kong Sheu, Taiwan
Panagiotis Smirniotis, USA
Zofia Stasicka, Poland
Elias Stathatos, Greece
M. Swaminathan, India
Kazuhiro Takanabe, Saudi Arabia
K. R. Justin Thomas, India
Yang Tian, China
Gopal N. Tiwari, India
Nikolai V. Tkachenko, Finland
Ahmad Umar, Saudi Arabia
Veronica Vaida, USA
Roel van De Krol, Germany
Mark van Der Auweraer, Belgium
Sheng Wang, China
Xuxu Wang, China
Mingkuai Wang, China
Ezequiel Wolcan, Argentina
Man Shing Wong, Hong Kong
David Worrall, UK
Jeffrey C. S. Wu, Taiwan
Fahrettin Yakuphanoglu, Turkey
Yanfa Yan, USA
Jiannian Yao, China
Minjoong Yoon, Republic of Korea
Hongtao Yu, USA
Jimmy C. Yu, Hong Kong
Jiangbo Yu, USA
Ying Yu, China
Klaas Zachariasse, Germany
Juan Antonio Zapien, Hong Kong
Tianyou Zhai, China
Lizhi Zhang, China
Jincai Zhao, China
Yong Zhou, China
Guijiang Zhou, China
Rui Zhu, China

Contents

Materials, Designs, Fabrications, and Applications of Organic Electronic Devices, Jwo-Huei Jou, Ramunas Lygaitis, K. R. Justin Thomas, and Liang-Sheng Liao
Volume 2014, Article ID 512717, 2 pages

Enabling Lambertian-Like Warm White Organic Light-Emitting Diodes with a Yellow Phosphor Embedded Flexible Film, Cheng-Chang Chen, Huang-Yu Lin, Cheng-Hung Li, Jin-Han Wu, Zong-Yi Tu, Li-Ling Lee, Ming-Shan Jeng, Chien-Chung Lin, Jwo-Huei Jou, and Hao-Chung Kuo
Volume 2014, Article ID 851371, 6 pages

Top-Emission Organic Light Emitting Diode Fabrication Using High Dissipation Graphite Substrate, Yu-Sheng Tsai, Lin-Ann Hong, Jian-Ji Huang, Kuan-Hung Yeh, and Fuh-Shyang Juang
Volume 2014, Article ID 319390, 6 pages

Improvement in Brightness Uniformity by Compensating for the Threshold Voltages of Both the Driving Thin-Film Transistor and the Organic Light-Emitting Diode for Active-Matrix Organic Light-Emitting Diode Displays, Ching-Lin Fan, Hao-Wei Chen, Hui-Lung Lai, Bo-Liang Guo, and Bohr-Ran Huang
Volume 2014, Article ID 604286, 8 pages

OLED Fabrication by Using a Novel Planar Evaporation Technique, Fu-Ching Tung, Yi-Shan Wang, Shih-Hsiang Lai, Chien-Chih Chen, Szu-Hao Chen, Ching-Chiun Wang, Jwo-Huei Jou, and Sun-Zen Chen
Volume 2014, Article ID 683037, 8 pages

Organic Light-Emitting Diode with Color Tunable between Bluish-White Daylight and Orange-White Dusk Hue, Shih-Yun Liao, Sudhir Kumar, Hui-Huan Yu, Chih-Chia An, Ya-Chi Wang, Jhong-Wei Lin, Yung-Lee Wang, Yung-Chun Liu, Chun-Long Wu, and Jwo-Huei Jou
Volume 2014, Article ID 480829, 6 pages

Improvement in Device Performance and Reliability of Organic Light-Emitting Diodes through Deposition Rate Control, Shun-Wei Liu, Chih-Chien Lee, Yu-Ting Chung, Jiun-Haw Lee, Chin-Ti Chen, and Juen-Kai Wang
Volume 2014, Article ID 412084, 7 pages

Investigation Performance and Mechanisms of Inverted Polymer Solar Cells by Pentacene Doped P3HT:PCBM, Hsin-Ying Lee and Hung-Lin Huang
Volume 2014, Article ID 812643, 9 pages

Au-Loaded Titanium Dioxide Nanoparticles Synthesized by Modified Sol-Gel/Impregnation Methods and Their Application to Dye-Sensitized Solar Cells, Hathaithip Ninsonti, Weerasak Chomkitichai, Akira Baba, Natda Wetchakun, Wiyong Kangwansupamonkon, Sukon Phanichphant, Kazunari Shinbo, Keizo Kato, and Futao Kaneko
Volume 2014, Article ID 865423, 8 pages

A Reuse Evaluation for Solar-Cell Silicon Wafers via Shift Revolution and Tool Rotation Using Magnetic Assistance in Ultrasonic Electrochemical Micromachining, P. S. Pa
Volume 2013, Article ID 293859, 10 pages

Editorial

Materials, Designs, Fabrications, and Applications of Organic Electronic Devices

Jwo-Huei Jou,¹ Ramunas Lygaitis,² K. R. Justin Thomas,³ and Liang-Sheng Liao⁴

¹ Department of Material Science and Engineering, National Tsing Hua University, Hsinchu 30013, Taiwan

² Department of Polymer Chemistry and Technology, Kaunas University of Technology, Radvilenu Road 19, 50254 Kaunas, Lithuania

³ Organic Materials Laboratory, Department of Chemistry, Indian Institute of Technology, Roorkee 247667, India

⁴ Institute of Functional Nano and Soft Materials, Soochow University, Suzhou 215123, China

Correspondence should be addressed to Jwo-Huei Jou; jjou@mx.nthu.edu.tw

Received 4 August 2014; Accepted 4 August 2014; Published 14 August 2014

Copyright © 2014 Jwo-Huei Jou et al. This is an open access article distributed under the Creative Commons Attribution License, which permits unrestricted use, distribution, and reproduction in any medium, provided the original work is properly cited.

Organic electronic devices (OEDs) are pronounced combination of sustainable organic materials, easily processable, potentially low cost, high throughput, and large-area roll-to-roll fabrication techniques that open up the numerous new fields of applications. The estimated global revenue was \$16 billion for OEDs in 2013 and is expected to reach \$77 billion in 2023 [1]. According to projected revenue reports [1, 2], organic light emitting diodes (OLEDs) and organic photovoltaics (OPVs) contribution is to be over 50%, which clearly states that both OLEDs [3] and OPVs [4] will play a major role in OEDs growth. Nowadays, OED technology is on the boom of reliability for numerous cutting edge applications. OEDs are drastically increasing the usage in high-quality OLED based displays and lightings, OPVs, smart packaging, medical products, radio-frequency identity tags, organic memory devices, organic batteries, organic sensors, and so forth.

Amongst, OLED based displays have attracted the greatest attention owing to their numerous disruptive features, such as energy efficiency, potentially low cost, light weight, ultrathin, wide viewing angle, fast response time, and ultra-high contrast. OLED devices can be fabricated either by solution process or by thermal evaporation. Wet-process enables the formation of cost-effective large-size roll-to-roll fabrication, while dry-process possesses the formation of well-controlled, high-quality films with ultimate design freedom for devices. However, both techniques have some severe issues, which must be resolved sooner to realize

a commercially competitive display or lighting device. In their paper, F.-C. Tung et al. developed a large-area feasible novel thin-film deposition technique with a planar source loadable with any premeasured solvent mixed organic compounds, plausibly with no component number limitation. The innovative technology would offer an over 70% material utilization rate with ultimately high thin layer uniformity (~95%). In order to achieve high efficiency and long operation lifetime in OLEDs, S.-W. Liu et al. investigated the role of deposition rate during thermal evaporation in high vacuum. Optimization of the deposition rate was applied to control the layer interface by molecular packing of planar molecule, such as bis(10-hydroxybenzo[h]quinolinato)beryllium, which can effectively reduce the driving voltage and increase the device efficiency as well as operating lifetime. For example, the operating lifetime of the two-step deposition OLED was 4.6 times longer than that with a single deposition rate.

At the present time, active-matrix OLED (AM-OLED) is an extensively acceptable display technology for portable electronic devices and is swiftly penetrating in large-area displays. In C.-L. Fan et al.'s paper, the authors proposed a new pixel circuit design, which comprises five transistors and one capacitor to supply the uniform current, and driving method to enhance the brightness uniformity of AM-OLEDs. They have employed the automatic integrated circuit modelling simulation programme with integrated circuit emphasis simulator for the voltage programming method of the proposed pixel circuits. Y.-S. Tsai et al. demonstrated a synthetic

graphite fiber as the heat dissipation substrate for top-emission OLED to reduce the joule heating. High dissipation graphite substrate extensively reduces the substrate heating rate to $0.037^{\circ}\text{C}/\text{sec}$ and realized a lifetime of 1.875 times higher than that of typical glass substrate.

OLEDs are steadily penetrating in lighting industry owing to their several unique characteristics, like very high color rendering index, sunlight style emission [5], candle light style emission [6, 7], physiologically friendly energy saving, and potentially cost-effective. Color temperature of light plays a crucial role in regulating human's circadian rhythm. It is well known that current lighting sources provide only a fixed color temperature light emission. Hence, devising a cost-effective light source with color temperature tunability, which can cover the entire daylight locus, would be highly required. S.-Y. Liao et al. reported a cost-effective sunlight style OLED device with a wide color temperature span of 7,000 K. They have also reported that the color temperature span can be made much wider without any additional carrier modulation layer. In order to realize a low cost and simple flexible OLED lighting, C.-C. Chen et al. reported a warm white OLED device from blue OLED by using a yellow phosphor embedded polydimethylsiloxane (PDMS) film on glass substrate. The resultant OLED device has shown the chromaticity coordinates of 0.38 and 0.54 and color temperature of 4,200 K.

The global demand for energy is increasing very fast, whereas the fossil (petroleum and coal) energy resources are draining rapidly. OPV is one future technology with enormous potential to supply an alternative clean energy source, which is projected to reach a higher profitability at a lower level cost of electricity. In recent years, OPVs have gained widespread attention due to their numerous superlative features, such as low cost, large area, flexible, roll-to-roll fabrication, and tunable optical properties. H. Ninsonti et al. synthesized the gold loaded titanium dioxide (Au-loaded TiO_2) nanoparticles by the sol-gel technique to enhance the performance of dye-sensitized solar cells (DSSC). It is found that the 1.0 mol.% Au-loaded TiO_2 possesses the plasmon effect and scattering property. In their paper, H.-Y. Lee and H.-L. Huang reported an inverted polymer solar cell (PSC) by employing pentacene-doped P3HT:PCBM absorption layers. They have found that the power conversion efficiency of inverted pentacene-doped PSCs is over 27% higher than that of PSCs without the pentacene doping. In future, the recycling of solar-cell silicon wafers is highly demanded. P. S. Pa reported in their paper that an ultrasonic electrochemical micromachining with high magnetic strength has facilitated a large discharge effect and fast removal of epoxy and silicon nitride hybrid composite layer. It is found that this newly developed technique would lead to an easy recycling of defective or used silicon wafers in the OPV industries.

All these research articles present a pioneering observation into the state of the art, as well as promising prospect for next generation displays, lightings, and renewable green energy sources. As reported in respective research articles, the cost-effective, high performance mass production of OLEDs and OPVs can easily be enhanced by the novel materials synthesis, tailoring of device architectures, development of

new fabrication technologies, and materials recycling tools. This special issue is going to contribute significantly to the development and commercialization of OLEDs and OPVs.

Jwo-Huei Jou
Ramunas Lygaitis
K. R. Justin Thomas
Liang-Sheng Liao

References

- [1] R. Das and P. Harrop, "Printed, organic and flexible electronics: forecasts, players and opportunities 2013-2023," <http://www.idtechex.com/research/reports/printed-organic-and-flexible-electronics-forecasts-players-and-opportunities-2013-2023-000350.asp?viewopt=desc>.
- [2] <http://www.transparencymarketresearch.com/global-organic-electronics-market.html>.
- [3] M. C. Gather, A. Köhnen, and K. Meerholz, "White organic light-emitting diodes," *Advanced Materials*, vol. 23, no. 2, pp. 233-248, 2011.
- [4] W. Cao and J. Xue, "Recent progress in organic photovoltaics : device architecture and optical design," *Energy & Environmental Science*, vol. 7, pp. 2123-2144, 2014.
- [5] J.-H. Jou, M.-H. Wu, S.-M. Shen et al., "Sunlight-style color-temperature tunable organic light-emitting diode," *Applied Physics Letters*, vol. 95, no. 1, Article ID 013307, 2009.
- [6] J.-H. Jou, C.-Y. Hsieh, J.-R. Tseng et al., "Candle light-style organic light-emitting diodes," *Advanced Functional Materials*, vol. 23, no. 21, pp. 2750-2757, 2013.
- [7] J.-H. Jou, P.-W. Chen, and Y.-L. Chen, "OLEDs with chromaticity tunable between dusk-hue and candle-light," *Organic Electronics*, vol. 14, no. 1, pp. 47-54, 2013.

Research Article

Enabling Lambertian-Like Warm White Organic Light-Emitting Diodes with a Yellow Phosphor Embedded Flexible Film

Cheng-Chang Chen,¹ Huang-Yu Lin,² Cheng-Hung Li,¹ Jin-Han Wu,¹ Zong-Yi Tu,²
Li-Ling Lee,¹ Ming-Shan Jeng,¹ Chien-Chung Lin,³ Jwo-Huei Jou,⁴ and Hao-Chung Kuo²

¹ Green Energy and Environment Research Laboratories, Industrial Technology Research Institute (ITRI), 195, Section 4, Chung Hsing Road, Chutung 31040, Taiwan

² Department of Photonics and Institute of Electro-Optical Engineering, National Chiao Tung University, Hsinchu 30010, Taiwan

³ Institute of Photonic System, National Chiao Tung University, Tainan 711, Taiwan

⁴ Department of Materials Science and Engineering, National Tsing Hua University, Hsinchu 30013, Taiwan

Correspondence should be addressed to Chien-Chung Lin; chienchunglin@faculty.nctu.edu.tw

Received 14 March 2014; Revised 26 May 2014; Accepted 17 June 2014; Published 16 July 2014

Academic Editor: Liang-Sheng Liao

Copyright © 2014 Cheng-Chang Chen et al. This is an open access article distributed under the Creative Commons Attribution License, which permits unrestricted use, distribution, and reproduction in any medium, provided the original work is properly cited.

We demonstrate in this report a new constructive method of fabricating white organic light-emitting devices (OLEDs) with a flexible plastic film embedded with yellow phosphor. The flexible film is composed of polydimethylsiloxane (PDMS) and fabricated by using spin coating followed by peeling technology. From the results, the resultant electroluminescent spectrum shows the white OLED to have chromatic coordinates of 0.38 and 0.54 and correlated color temperature of 4200 K. The warm white OLED exhibits the yield of 10.3 cd/A and the luminous power efficiency of 5.4 lm/W at a luminance of 1000 cd/m². A desirable Lambertian-like far-field pattern is detected from the white OLEDs with the yellow phosphor containing PDMS film. This method is simple, reproducible, and cost-effective, proving to be a highly feasible approach to realize white OLED.

1. Introduction

In recently years, there have been great demands to replace the traditional lighting sources with more energy efficient ones. White organic light-emitting devices (OLEDs) are one of the most promising technologies for display and lighting applications owing to their advantages of low power consumption, large viewing angle, high contrast ratio, and short response time. Thus, the OLED has been considered as a possible solution for the next generation of light sources [1–3]. To meet the required standard, the electroluminescence (EL) of OLEDs should contain broad emissions that cover the entire visible range of the spectrum with Commission International de l'Éclairage (CIE) chromaticity coordinates of (0.33, 0.33).

Many methods have been developed to generate the white light emission of OLED by the partial energy transfer, such as host materials that are doped with fluorescence/phosphorescence dyes [4–13]. Several researchers have

developed the mixing of the EL from the host molecules with the excimer/excimer emissions to yield white light emission [14–16]. Other methods are to stack red-, green-, and blue-emissive components to fabricate OLEDs. By stacking RGB components and charge generation layer (CGL), a tandem structure could demonstrate good luminous efficiency [17–22]. However, the tandem structure has a major challenge of carrier transport in the junction interface and the multiple-stacking structure is complex.

On the other hand, the white light LEDs combined blue GaN chip and phosphors are quite common [23] and commercially available these days. This technology is mature and applied widely in many fields. In this study, a novel method to combine the feature of OLED and phosphor-based technology is proposed and demonstrated.

The fabrication of the phosphor embedded PDMS film of white OLED is easy to correlate the ordinary process of white OLED. A simplest white OLED consists of two kinds of emissive layer which can emit the complementary color light:

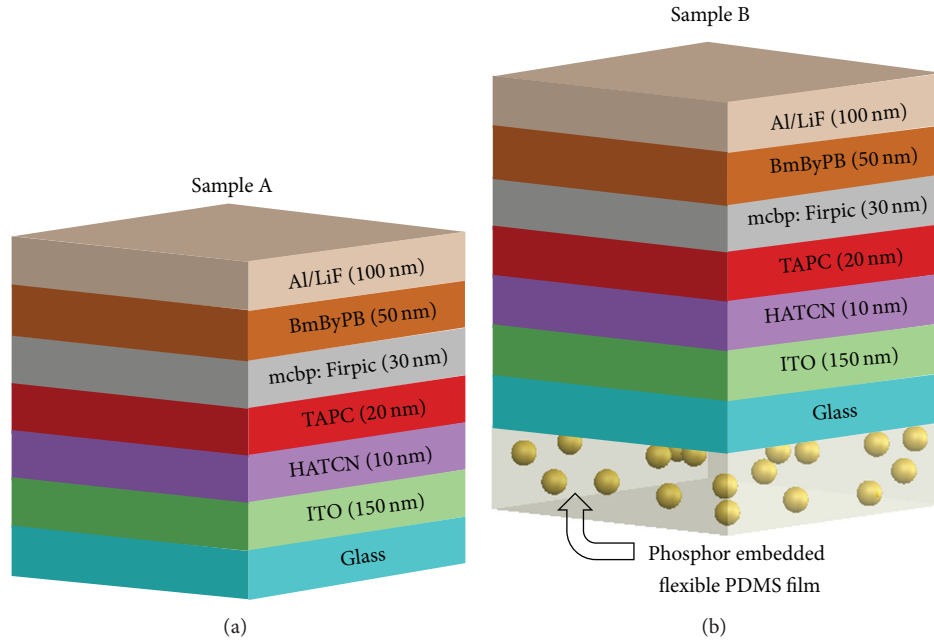


FIGURE 1: Schematic structures of OLEDs device (a) without a yellow phosphor embedded flexible film as a reference and (b) with a yellow phosphor embedded flexible film.

blue and yellow. Each layer of organic materials was subject to temperature-gradient sublimation under high vacuum before use. The organic layer and metal layers were deposited by vacuum vapor deposition in a vacuum chamber. Fabricating white OLED is complicated due to the modification of multi-emissive layers. The PDMS film is also easy to fabricate and has the ability to resist moisture and heat resistance. The large-area and cost-effective phosphor-embedded PDMS film is utilized to attach with regular OLED cell to provide a new direction for light sources. In the following test, the fabrication steps and results will be discussed in detail.

2. Materials and Fabrication Process

The blue fluorescence of the bottom-emitting OLEDs without PDMS film was fabricated as a reference. Each layer of organic materials was subject to temperature-gradient sublimation under high vacuum before use. OLEDs were fabricated on the ITO-coated glass substrates between the transparent bottom indium-tin-oxide (ITO) anode and the top metal cathode. The organic and metal layers were deposited by vacuum vapor deposition in a vacuum chamber with a base pressure of $<10^6$ torr. The deposition system permitted the fabrication of the complete device structure in a single vacuum pump-down without breaking vacuum. The deposition rate of organic layers was kept at ~ 0.1 nm/s. The active area of the device is 0.3×0.3 cm², which is defined by the shadow mask for cathode deposition. After fabricating the OLED devices, the method of glass-to-glass OLED package with desiccant was used in a glove box. Before packing, the glass would be pretreated by solvent cleaning and UV-curing in order to

remove the moisture and particle, increasing the adhesion between the glass lid and substrate, simultaneously. Then we used the packing machine to drop the UV glue on the substrate and made the glass lid and substrate closer by exerting forward force. Finally, the device was treated with UV curing of 110 seconds.

The OLED device structures were glass substrate/ITO (150 nm)/HATCN (10 nm)/TAPC (30 nm)/mcbp: Firpic (10 wt.%, 20 nm)/BmByPB (50 nm)/LiF (1 nm)/Al (100 nm)/. Indium-tin-oxide (ITO) was used as the bottom anode, Dipyrzino[2,3-f:2',3'-h]quinoxaline-2,3,6,7,10,11-hexacarbonitrile(HATCN) as the hole-injection layer, 4,4'-cyclohexylidenebis[N,N-bis(4-methylphenyl)benzenamine](TAPC) as the hole-transport layer, 3,5-di(9H-carbazol-9-yl)biphenyl(mcbp): bis(3,5-difluoro-2-(2-pyridyl)phenyl)-(2-carboxypyridyl)iridium(III)(Firpic) as the emitting layer, 1,3-bis[3,5-di(pyridin-3-yl)phenyl]benzene(BmByPB) as the electron-transport layer, thin LiF as the electron injection layer, and Al as the top cathode. Illustrations of the reference and white light OLEDs structures are shown in Figures 1(a) and 1(b), respectively.

The flexible PDMS film was fabricated using the spin coating and peeling technology as the following steps [23]. First, yellow phosphor ($Y_3Al_5O_{12}:Ce^{3+}$) with the particle size of $10 \mu\text{m}$ is blended with the silicone to form the phosphor-suspension slurry. Then the solution is dropped and spin coated for 500 rpm for 30 s on the glass substrate, and then baked it in an oven at about 80°C . Finally, the PDMS film is peeled off from the glass substrate then put the film on the OLED's glass substrate. Figure 2 shows the magnified image of the PDMS film from an angle-view. The size distribution of yellow phosphor embedded in PDMS film can also be seen

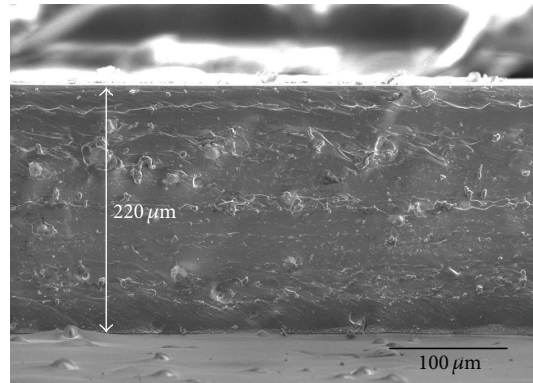


FIGURE 2: The angle-view SEM image of the yellow phosphor embedded flexible PDMS film.

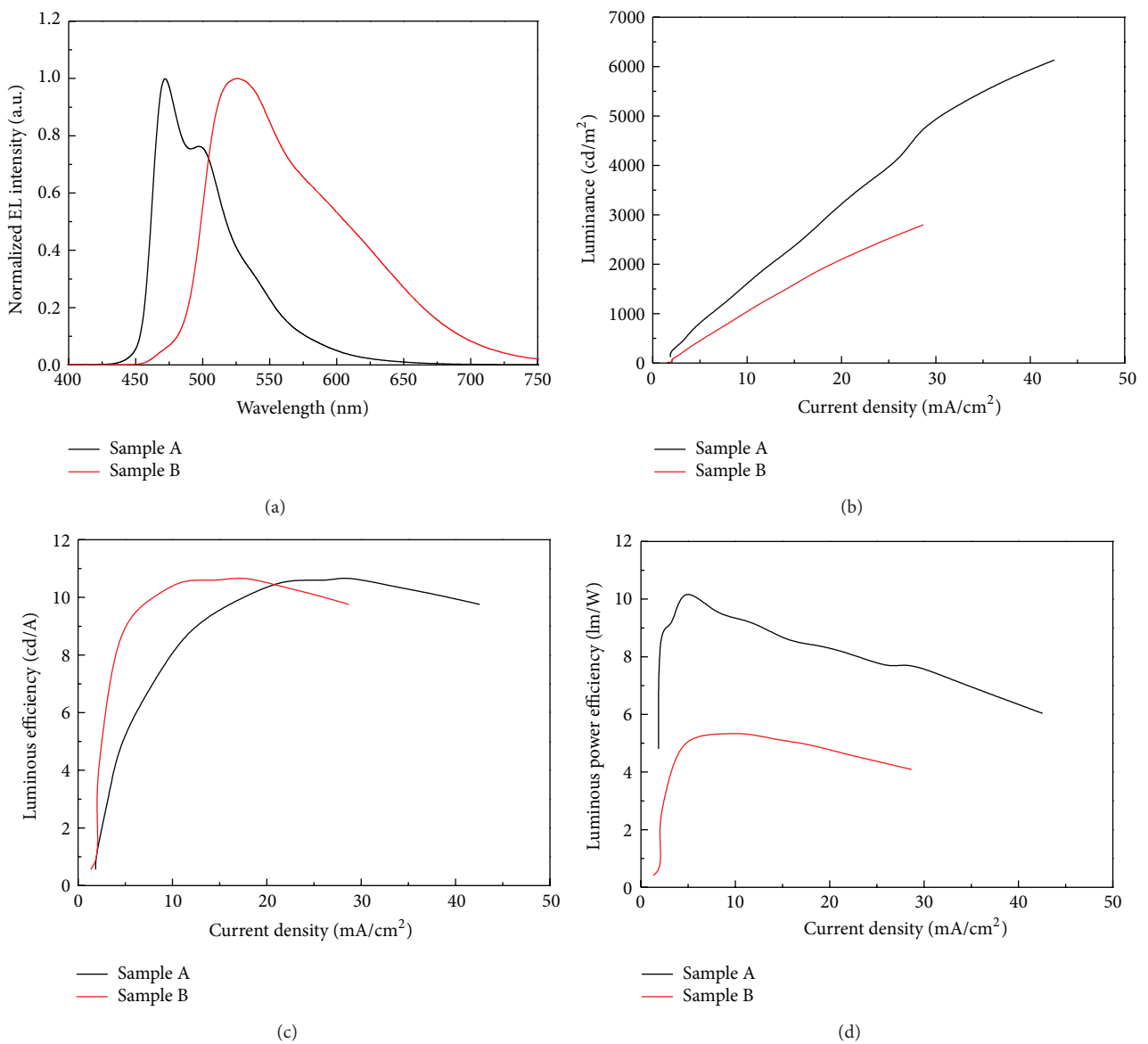


FIGURE 3: (a) The measured EL spectra in the normal direction of Sample A and Sample B. (b) Luminance, (c) current efficiency, and (d) luminous power efficiency characteristics of Sample A and Sample B as a function of current density.

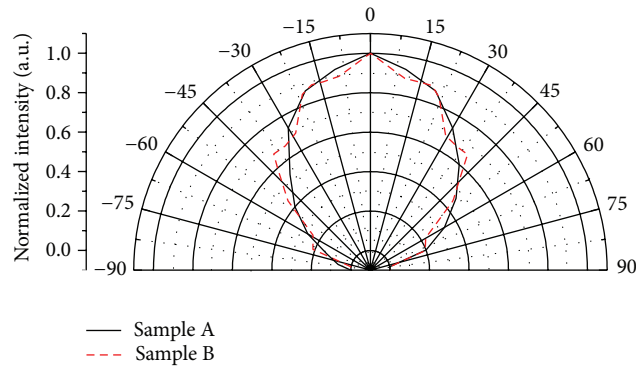


FIGURE 4: Measured far-field pattern for the OLEDs devices of Sample A and Sample B.

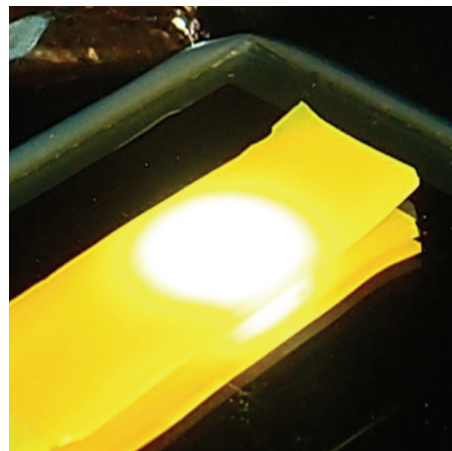
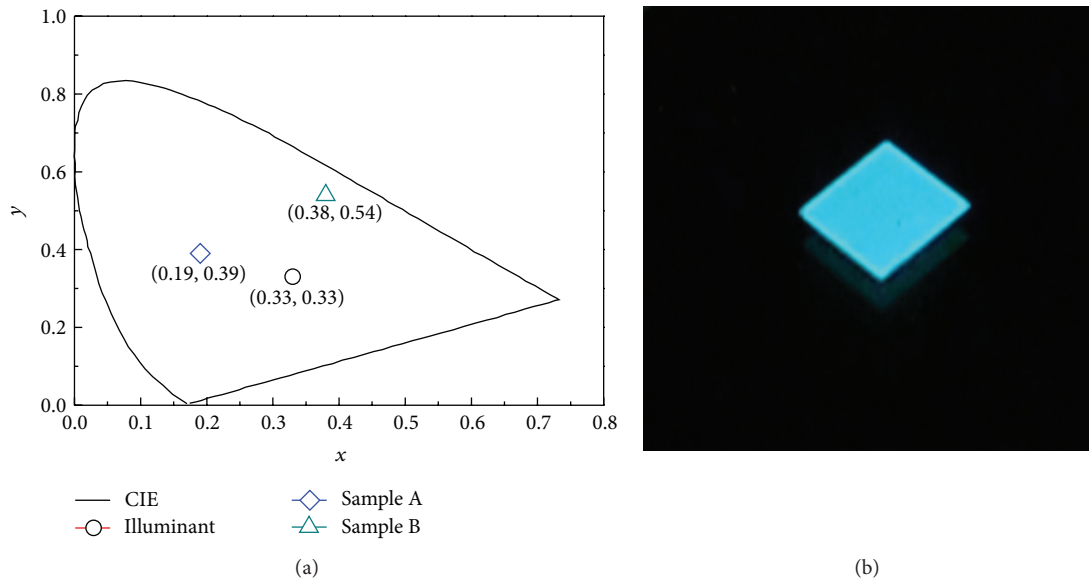


FIGURE 5: (a) The CIE coordinates of Sample A and Sample B. (b) The blue light photography of Sample A. (c) Warm white light photography of Sample B.

seen in Figure 2, in which yellow phosphor has a size of $10\ \mu\text{m}$. The thickness of the PDMS layer is measured approximately $220\ \mu\text{m}$.

3. Results and Discussion

To characterize the light emission properties of white organic light-emitting devices, a UV/VIS spectrometer was used and two OLEDs devices (samples A and B) were prepared. Sample B is the organic light-emitting diode with a yellow phosphor embedded PDMS film and Sample A has an identical OLEDs device without flexible PDMS film. Figure 3(a) shows the electroluminescent (EL) measured spectra from OLEDs devices of Sample A (black curve) and Sample B (red curve) in the normal direction. The wide spectral of the Sample B becomes broad and the emitting wavelength has a red shift that can be seen as energy transfer between the blue OLED and phosphor.

As expected, the emission peaks of Sample A are 470 nm and 500 nm. The emission peak of Sample B is 525 nm, and the spectrum has the visible range from 400 nm to 750 nm due to color mixing.

The luminance current efficiency and luminous power efficiency as a function of current density of the OLEDs device were investigated. Figures 3(b), 3(c), and 3(d) show the results of Sample A and Sample B measured in the normal direction. As presented, Sample A has high luminance and maximum luminous efficiency over $5,000\ \text{cd}/\text{m}^2$ and $16.5\ \text{cd}/\text{A}$. Sample B has a yield of $10.3\ \text{cd}/\text{A}$ at a luminance of $1000\ \text{cd}/\text{m}^2$. The maximum luminous power efficiencies of Sample A and Sample B are $9.4\ \text{lm}/\text{W}$ with the current density of $7.9\ \text{mA}/\text{cm}^2$ and $5.4\ \text{lm}/\text{W}$ with the current density of $9.9\ \text{mA}/\text{cm}^2$, respectively. The phosphorescence emission OLED containing FIrpic has the lifetime of 200 hr [24]. The lifetime of both Sample A and Sample B is the same.

The measured far-field emission profiles of Sample A and Sample B are shown in Figure 4. As shown in Figure 4, Sample A has the Lambertian-like radiation pattern at the full-width at half-maximum of $\pm 30^\circ$ along the surface normal view. A desirable Lambertian-like far-field pattern is also observed from Sample B due to the randomness particles of phosphor embedded flexible PDMS film. The CIE coordinates of EL at normal direction from Sample A and Sample B are at (0.19, 0.39) and (0.38, 0.54) with correlated color temperature of 4200 K, shown in Figure 5(a). The CIE coordinates of EL from sample A was obviously shifted and, hence, the corresponding emission color is changed.

Figures 5(b) and 5(c) show the photography of OLEDs devices during measurement. Blue light and warm white light regions are corresponding to Sample A and Sample B. The combination of OLEDs with a yellow phosphor embedded flexible film possesses many possibilities for in solid state lighting.

4. Conclusions

In summary, a warm white organic light-emitting diode was demonstrated by attaching a yellow phosphor embedded flexible PDMS film. The flexible PDMS film was fabricated

using the spin coating and peeling technology. From the measured results, the warm white organic light-emitting diode has an efficiency of $10.3\ \text{cd}/\text{A}$, luminous power efficiency of $5.4\ \text{lm}/\text{W}$, and the CIE coordinate of (0.38, 0.54) with correlated color temperature of 4200 K at a luminance of $1000\ \text{cd}/\text{m}^2$. We believe that this approach of the fabricating method offers a viable solution to realize that white OLEDs and Lambertian-like profile shaping are suitable for applications in lighting and displays.

Conflict of Interests

The authors declare that there is no conflict of interests regarding the publication of this paper.

Acknowledgment

The authors would like to gratefully acknowledge the Bureau of Energy, Ministry of Economic Affairs of Taiwan, for financially supporting this research.

References

- [1] J. Kido, M. Kimura, and K. Nagai, "Multilayer white light-emitting organic electroluminescent device," *Science*, vol. 267, no. 5202, pp. 1332–1334, 1995.
- [2] B. W. D'Andrade and S. R. Forrest, "White organic light-emitting devices for solid-state lighting," *Advanced Materials*, vol. 16, no. 18, pp. 1585–1595, 2004.
- [3] C. W. Ko and Y. T. Tao, "Bright white organic light-emitting diode," *Applied Physics Letters*, vol. 79, p. 4234, 2001.
- [4] J. Kido, K. Hongawa, K. Okuyama, and K. Nagai, "White light-emitting organic electroluminescent devices using the poly(N-vinylcarbazole) emitter layer doped with three fluorescent dyes," *Applied Physics Letters*, vol. 64, no. 7, pp. 815–817, 1994.
- [5] J. Kido, H. Shionoya, and K. Nagai, "Single-layer white light-emitting organic electroluminescent devices based on dye-dispersed poly(N-vinylcarbazole)," *Applied Physics Letters*, vol. 67, no. 16, p. 2281, 1995.
- [6] S. Tokito, T. Iijima, T. Tsuzuki, and F. Sato, "High-efficiency white phosphorescent organic light-emitting devices with greenish-blue and red-emitting layers," *Applied Physics Letters*, vol. 83, no. 12, pp. 2459–2461, 2003.
- [7] L. Wang, G. Lei, and Y. Qiu, "Bright white organic light-emitting diodes based on two blue emitters with similar molecular structures," *Journal of Applied Physics*, vol. 97, no. 11, Article ID 114503, 2005.
- [8] Y. Sun, N. C. Giebink, H. Kanno, B. Ma, M. E. Thompson, and S. R. Forrest, "Management of singlet and triplet excitons for efficient white organic light-emitting devices," *Nature*, vol. 440, no. 7086, pp. 908–912, 2006.
- [9] J. Huang, W. J. Hou, J. H. Li, G. Li, and Y. Yang, "Improving the power efficiency of white light-emitting diode by doping electron transport material," *Applied Physics Letters*, vol. 89, no. 13, Article ID 133509, 2006.
- [10] J. H. Seo, J. H. Park, Y. K. Kim et al., "Highly efficient white organic light-emitting diodes using two emitting materials for three primary colors (red, green, and blue)," *Applied Physics Letters*, vol. 90, no. 20, Article ID 203507, 2007.

- [11] J. H. Jou, M. H. Wu, C. P. Wang et al., "Efficient fluorescent white organic light-emitting diodes using co-host/emitter dual-role possessed di(triphenyl-amine)-1,4-divinyl-naphthalene," *Organic Electronics*, vol. 8, no. 6, pp. 735–742, 2007.
- [12] J. H. Jou, Y. S. Chiu, C. P. Wang, R. Y. Wang, and H. C. Hu, "Efficient, color-stable fluorescent white organic light-emitting diodes with single emission layer by vapor deposition from solvent premixed deposition source," *Applied Physics Letters*, vol. 8, Article ID 193501, 2006.
- [13] Y. C. Tsai and J. H. Jou, "Long-lifetime, high-efficiency white organic light-emitting diodes with mixed host composing double emission layers," *Applied Physics Letters*, vol. 89, Article ID 243521, 2006.
- [14] B. W. D'Andrade, J. Brooks, V. Adamovich, M. E. Thompson, and S. R. Forrest, "White light emission using triplet excimers in electrophosphorescent organic light-emitting devices," *Advanced Materials*, vol. 14, no. 15, pp. 1032–1036, 2002.
- [15] E. L. Williams, K. Haavisto, J. Li, and G. E. Jabbour, "Excimer-based white phosphorescent organic light emitting diodes with nearly 100 % internal quantum efficiency," *Advanced Materials*, vol. 19, no. 2, pp. 197–202, 2007.
- [16] J. Kalinowski, M. Cocchi, D. Virgili, V. Fattori, and J. A. G. Williams, "Mixing of excimer and exciplex emission: a new way to improve white light emitting organic electrophosphorescent diodes," *Advanced Materials*, vol. 19, no. 22, pp. 4000–4005, 2007.
- [17] Z. Shen, P. E. Burrows, V. Bulović, S. R. Forrest, and M. E. Thompson, "Three-color, tunable, organic light-emitting devices," *Science*, vol. 276, no. 5321, pp. 2009–2011, 1997.
- [18] L. S. Liao, K. P. Klubek, and C. W. Tang, "High-efficiency tandem organic light-emitting diodes," *Applied Physics Letters*, vol. 84, no. 2, pp. 167–169, 2004.
- [19] H. Kanno, R. J. Holmes, Y. Sun, S. Kena-Cohen, and S. R. Forrest, "White stacked electrophosphorescent organic light-emitting devices employing MoO₃ as a charge-generation layer," *Advanced Materials*, vol. 18, no. 3, pp. 339–342, 2006.
- [20] M. H. Ho, T. M. Chen, P. C. Yeh, S. W. Hwang, and C. H. Chen, "Highly efficient *p-i-n* white organic light emitting devices with tandem structure," *Applied Physics Letters*, vol. 91, no. 23, Article ID 233507, 2007.
- [21] T. W. Lee, T. Hoh, B. K. Choi, M. S. Kim, D. W. Shin, and J. Kido, "High-efficiency stacked white organic light-emitting diodes," *Applied Physics Letters*, vol. 92, no. 4, Article ID 043301, 2008.
- [22] L. Liao, W. K. Slusarek, T. K. Hatwar, M. L. Ricks, and D. L. Comfort, "Tandem organic light-emitting diode using hexaaza-triphenylene hexacarbonitrile in the intermediate connector," *Advanced Materials*, vol. 20, no. 2, pp. 324–329, 2008.
- [23] K. Chen, H. Chen, K. Tsai et al., "Resonance-enhanced full-color emission of quantum dot-based display technology using a pulsed spray method," *Advanced Functional Materials*, vol. 22, no. 24, pp. 5138–5143, 2012.
- [24] M. S. Weaver, Y. J. Tung, B. D'Andrade et al., "11.1: invited paper: advances in blue phosphorescent organic light-emitting devices," *SID Symposium Digest of Technical Papers*, vol. 37, no. 1, pp. 127–130, 2006.

Research Article

Top-Emission Organic Light Emitting Diode Fabrication Using High Dissipation Graphite Substrate

Yu-Sheng Tsai,¹ Lin-Ann Hong,¹ Jian-Ji Huang,² Kuan-Hung Yeh,¹ and Fuh-Shyang Juang¹

¹ Master of Electro-Optical and Materials Science, National Formosa University, Yunlin 632, Taiwan

² Department of Multimedia and Game Science, Chung Chou University of Science and Technology, Changhua 51003, Taiwan

Correspondence should be addressed to Lin-Ann Hong; jackie52046@yahoo.com.tw

Received 14 March 2014; Revised 14 May 2014; Accepted 22 May 2014; Published 2 July 2014

Academic Editor: K. R. Justin Thomas

Copyright © 2014 Yu-Sheng Tsai et al. This is an open access article distributed under the Creative Commons Attribution License, which permits unrestricted use, distribution, and reproduction in any medium, provided the original work is properly cited.

This study uses a synthetic graphite fiber as the heat dissipation substrate for top-emission organic light emitting diode (TEOLED) to reduce the impact from joule heat. UV glue (YCD91) was spin coated onto the substrate as the insulation layer. The TEOLED structure is (glass; copper; graphite) substrate/YCD91 glue/Al/Au/EHI608/TAPC/Alq₃/LiF/Al/Ag. The proposed graphite fiber substrate presents better luminous performance compared with glass and copper substrate devices with luminance of 3055 cd/m² and current efficiency of 6.11 cd/A at 50 mA/cm². When lighting period of different substrates TEOLED, the substrate case back temperature was observed using different lighting periods. A glass substrate element operating from 5 to 25 seconds at 3000 cd/m² luminance produced a temperature rate of 1.207°C/sec. Under 4000 cd/m² luminance the copper and graphite substrate temperature rates were 0.125°C/sec and 0.088°C/sec. Graphite component lifetime was determined to be 1.875 times higher than the glass components and 1.125 times higher than that of copper.

1. Introduction

Pope used anthracene monocrystals as luminescent materials in 1963 [1]. However, the operating voltage was higher with lower energy transformation efficiency and no application value [2]. Afterwards, Tang and VanSlyke, Kodak, USA, used vacuum evaporate plating to produce a multilayered OLED using small molecular organic Alq₃ as the luminescent and charge transfer material. This innovation greatly improved OLED component characteristics to less than 10 V operating voltage with a quantum efficiency and device structure close to 1%. Using non-mono-vacuum evaporate plating or close to amorphous organic semiconducting thin film technology created a device structure with heterogeneous multilayer organic film contact that greatly improved OLED device performance. This became the operating standard for current OLEDs [3, 4]. In 1990 the Cambridge research team successfully developed a yellow-green luminescence LED [5] using PPV luminescent material. Because these macromolecular polymer materials possess characteristics similar to semiconductors and have a simple manufacturing process, they attracted great interest as a potential OLED polymer.

The substrate selection process used for TEOLED should consider the surface evenness, resistance to bumping, light weight, and thin, waterproof, and anticorrosive properties. For example, a plastic substrate possesses light, thin, short, and small advantages with resistance to fracture and reability. However, most of these materials are not resistant to high temperature and are easily degraded by water and oxygen, further reducing the component service life [6]. Someone also attempted to produce OLEDs, a paper base, but there is still a long way to go before this product is ready for commercialization [7]. The introduction of metal foil as the substrate seems to solve the plastic substrate shortcomings with better energy dissipation that could strengthen the component operating time. However, the required surface polishing is something that requires great attention [8]. In 2001, Paulo N. M. Dos Anjos and others used ITO/NPB/Alq₃/Mg:Ag as the experimental structure and applied a buffer layer, CuPc, onto the ITO electrode. From the experimental result, we can see that the structure temperature is 70°C without applying a buffer layer, reducing the temperature to 22°C after applying the buffer layer [9].

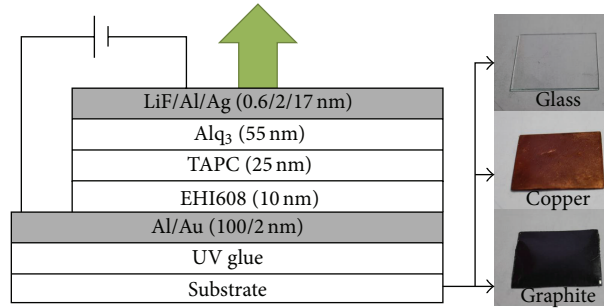


FIGURE 1: Component structure of TEOLED.

TABLE 1: Surface roughness characteristics of different substrates.

(a)

Number	Substrates	UV glue* (YCD91)	W/o UV glue (Rms: nm)	With UV glue (Rms: nm)
a	Glass	18 μm	4.37	2.97
b	Copper	19 μm	3.27	2.85
c	Graphite	21 μm	15.07	0.68

*Material composition (YCD91).

(b)

Oligomer-TM621	Monomer-2PEA	TMPTA-20EA	Photo initiator 184
40	30	30	1.5%

K. Sudheendra Rao et al. raised the device with structure ITO/m-MTDATA/NPB/Alq₃:C545T/Alq₃/LiF/Al. As a standard procedure Alq₃ is doped with C545T for optimized efficiency (12 cd/A) [10].

2. Experimental

The substrate is spin coated onto glass, copper, and graphite substrates at 1200 rpm for 15 seconds and at 2400 rpm for 20 seconds of UV glue (YCD91) (from Material and Chemical Research Laboratories, Industrial Technology Research Institute). YCD91 was exposed under UV light for 75 seconds to cure. Correct curing produces appropriate substrate material viscosity, which produces uniform spin coating. The treated substrates were placed into a metal thermal system and vacuumized to 6.65×10^{-4} Pa. Al and Au metals were then vacuum evaporated according to the sequence. The substrates were then placed in an organic evaporator and vacuumed to 6.65×10^{-4} Pa. Hole injection layer (HIL) material EHI608, hole transport layer (HTL) material TAPC, and emitting layer material (EML) or electron transport layer (ETL) Alq₃ were then vacuum evaporated according to the sequence. The LiF, Al, and Ag cathode metals were then vacuum evaporated in sequence. The finished TEOLED components were tested for luminous characteristics and temperature at the substrate back using multifunctional ammeter KEITHLEY 2400, spectrophotometer PR650, and IR camera NEC TH7716.

3. Results and Discussion

3.1. Characteristics Comparison of Different TEOLED Device Substrates. The TEOLED device structure is Al (100 nm)/Au (2 nm)/EHI608 (10 nm)/TAPC (25 nm)/Alq₃ (55 nm)/LiF (0.6 nm)/Al (2 nm)/Ag (17 nm) as indicated in Figure 1. The material thickness of each OLED layer is listed in Table 2. The UV glue (YCD91) material, including heat dissipation particles, was spin coated onto glass, copper, and graphite substrates and then left exposed in air for hardening. The substrate surface roughness was then analyzed using atomic force microscopy (AFM) as shown in Figure 2 and Table 1. The measurement results show that the Rms roughness of the glass, copper, and graphite substrates before spin coating was 4.37, 3.27, and 15.07 nm and 2.97, 2.85, and 0.68 nm after spin coating and drying. Because the graphite substrate is obtained from carbon fiber the surface roughness is quite high. After UV glue spin coating the material roughness was significantly reduced to Rms 0.68 nm. Table 2 shows the roughness comparison of each spin coated UV plastic substrate material.

The TEOLED device with the graphite substrate exhibited that operating voltage is 14.6 V, lower than that of the glass and copper substrates at 15 V and 15.5 V at 50 mA/cm². The luminance and current efficiency of the graphite substrate were 3054 cd/m² and 6.11 cd/A, respectively, compared with those of the copper substrate (2835 cd/m² and 5.67 cd/A) and the glass substrate (2730 cd/m² and 5.46 cd/A). Comparing the

TABLE 2: Parameter of each layer for TEOLED (unit: nm).

Number	Substrate (with UV glue)	Al	Au	HIL EHI608	HTL TAPC	EML/ETL Alq ₃	EIL LiF	Al	Ag
I	Glass								
II	Copper	100	2	10	25	55	0.6	2	17
III	Graphite								

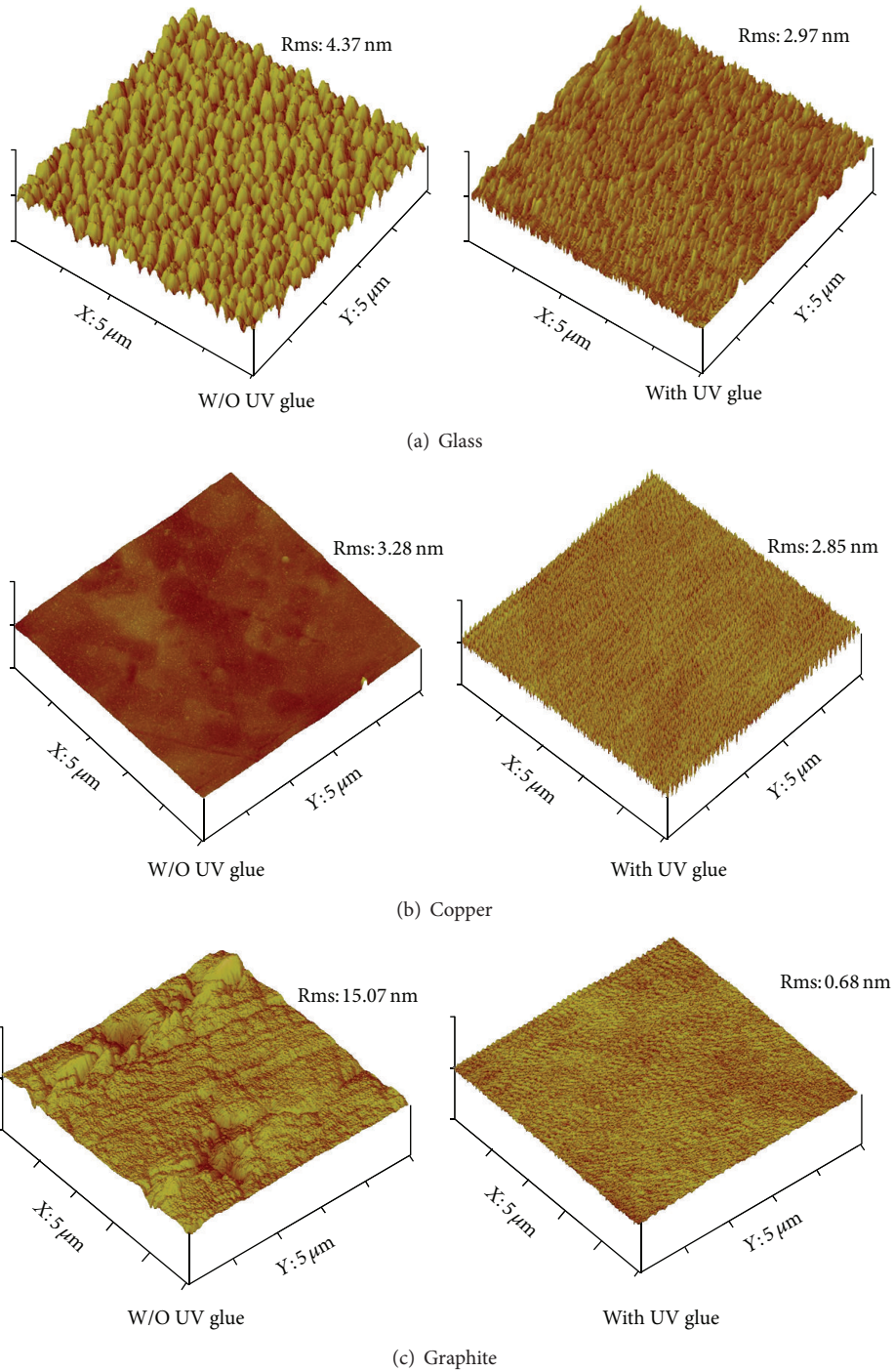


FIGURE 2: UV glue spin coated onto three substrates by AFM.

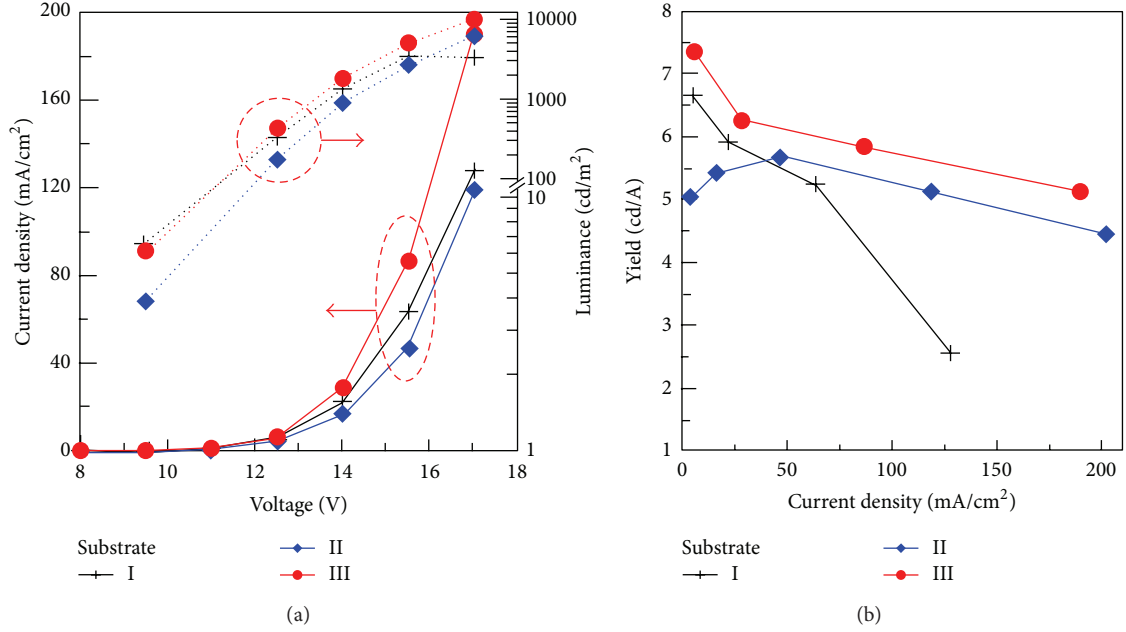


FIGURE 3: (a) Current density-voltage-luminance. (b) Current efficiency-current density of TEOLED.

TABLE 3: Thermal conductivity value for glass, copper, and graphite fiber.

Substrate materials	Thermal conductivity value (W/m*K)
Glass	1.38
Copper	398
Graphite fiber	400~500

luminous characteristics of graphite, copper, and glass, we can see that materials with higher substrate thermal conductivity coefficient achieve better luminous characteristics compared with the glass substrate. The heat dissipating substrate could also elevate the device stability, allowing operation at higher voltage.

The thermal conductivity coefficients for the graphite and copper substrates are much better than that of glass, as indicated in Table 3. From Figure 2 these three substrates are relatively closer in device characteristics at low voltage. However, under high voltage the thermal conductivity of glass restrained the device from dissipating heat, leading to organic layer material crystallization, making the overall device luminous characteristics worse. The graphite and copper substrate devices could maintain higher luminance and current efficiency under higher operating voltage. The thermal conductivity of graphite fiber is better than that of copper. At a current density from 50 to 175 mA/cm², Device III current efficiency roll-off is 18.1% while that of Device II is 21.3%, both better than Device I (roll-off is 51.3% at current density from 50 to 125 mA/cm²) (see Figure 3).

Using material with high thermal conductivity coefficient as the TEOLED substrate could make TEOLED devices achieve better luminous characteristics. At the same time it could also dissipate the heat, removing the negative impact

on device luminous characteristics at high voltage. The heat flow reference is defined in (1), within a setting time (t); the heat (Q) flows from the plane of a higher temperature (T_H) to the plane of a lower temperature (T_C) where A is the area, L the length, and k the material thermal conductivity. However, (1) is specifically for the rate of heat flow for a single layer material. The OLED device is composed of two electrodes and multiple organic layers. Therefore the above equation should be replaced with (2) [11]. Consider

$$H \left(= \frac{Q}{t} \right) = kA \frac{T_H - T_C}{L}, \quad (1)$$

$$H = \frac{A(T_H - T_C)}{\sum_i (L_i/k_i)}, \quad (2)$$

$$H_{(\text{glass;copper;graphite})}$$

$$= A(T_H - T_C)$$

$$\times \left(\frac{10 \times 10^{-9} \text{ m}}{k_{\text{EHI608}}} + \frac{25 \times 10^{-9} \text{ m}}{k_{\text{TAPC}}} + \frac{55 \times 10^{-9} \text{ m}}{k_{\text{Alq}_3}} \right. \\ \left. + \frac{2 \times 10^{-9} \text{ m}}{k_{\text{Au}}} + \frac{100 \times 10^{-9} \text{ m}}{k_{\text{Al}}} \right) \quad (3)$$

$$+ \left(\left(18 \times 10^{-6} \text{ glass}; 19 \times 10^{-6} \text{ copper}; \right.$$

$$21 \times 10^{-6} \text{ graphite m} \times (k_{\text{glue}})^{-1}$$

$$\left. + \frac{0.5 \times 10^{-3} \text{ m}}{k_{(\text{glass;copper;graphite})}} \right)^{-1}.$$

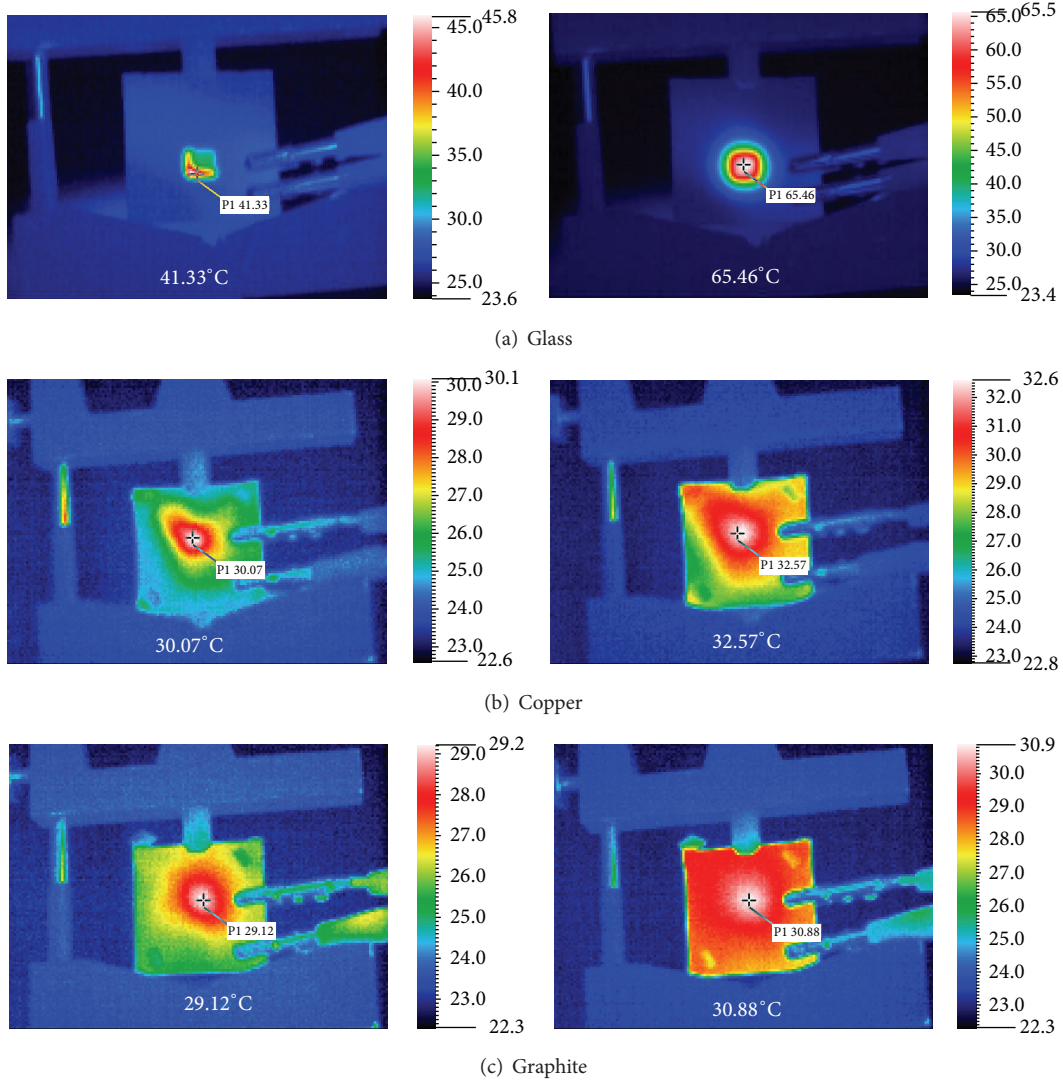


FIGURE 4: Temperature when (a) the glass (b) copper or (c) graphite substrate device is operated. Left is operated for 5 seconds; right is operated for 25 seconds.

Comparing (3) for the current TEOLED structure, the key factors affecting the heat flow rate are the thermal conductivity (k), substrate thickness (L), and UV glue materials. Since the thermal conductivity of graphite is about $k_{\text{graphite}} = 400\text{--}500\text{ W/m}\cdot\text{K}$, copper is about $k_{\text{copper}} = 397\text{ W/m}\cdot\text{K}$, glass is about $k_{\text{glass}} = 1.38\text{ W/m}\cdot\text{K}$, and UV glue is about $k_{\text{YCD91}} = 0.5\text{ W/m}\cdot\text{K}$, the rate of heat flow for TEOLED with a graphite substrate is better than that of both copper and glass substrates. Figure 4 shows the measured junction temperature and surface thermal distribution image results.

3.2. Heat Dissipation Test of TEOLED Devices. Substrate temperature tests were conducted using copper, graphite, and glass substrates on the emission area and substrate back after operating from 5 to 25 seconds. When the luminance was 3000 cd/m^2 (current density of 57 mA/cm^2) for the glass substrate device, the device highest temperature area was the emission area about 41.33°C as indicated in Figure 4(a). With 25-second operation the temperature increased to 65.46°C ,

concentrated in the emission area. When the copper substrate device was operated at 4000 cd/m^2 luminance (current density of 75 mA/cm^2), its back temperature was at 30.07°C as indicated in Figure 4(b). The temperature increased slightly to 32.57°C after lighting for 25 seconds. The temperature at the back of the substrate was 29.12°C when the graphite substrate component was operated at 4000 cd/m^2 luminance (current density of 68 mA/cm^2) as indicated in Figure 4(c). The temperature increased slightly to 30.88°C after lighting for 25 seconds. When the device was emitted for a certain period the device surface was cooler than that of copper and glass. The above study result shows that the high thermal conductivity characteristics of the graphite fiber substrate could effectively dissipate the heat produced from the device during high voltage operation.

Three TEOLEDs with different substrates were packaged in PET for component lifetime measurements. At 500 cd/m^2 of luminance, Figure 5 shows that the glass substrate had a lifetime of only 4 hours due to poor heat dissipation.

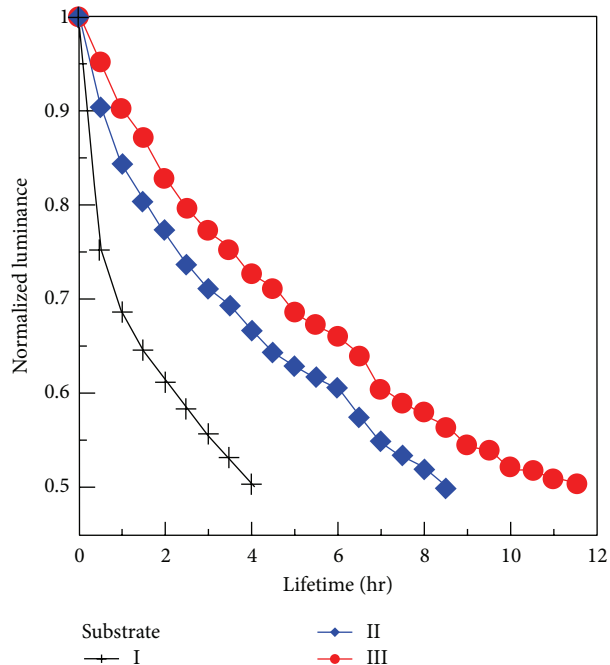


FIGURE 5: Component lifetime curves of the different substrates.

The graphite substrate component lifetime was 11.5 hours due to better cooling.

4. Conclusions

The TEOLED structure is (glass; copper; graphite) substrate/YCD91 glue/Al/Au/EHI608/TAPC/Alq₃/LiF/Al/Ag. From the experimental results the graphite fiber substrate produced better luminous performance compared with the glass and copper substrate devices at luminance of 3055 cd/m² and current efficiency of 6.11 cd/A at 50 mA/cm². At a current density from 50 to 175 mA/cm², Device III current efficiency roll-off was 18.1%. The substrate case back temperature was observed for different TEOLED substrates operated at several lighting periods. A glass substrate element operating from 5 to 25 seconds of luminance at 3000 cd/m² produced a temperature rate of 1.207°C/sec. Under luminance of 4000 cd/m² the copper and graphite substrate temperature rates were 0.125°C/sec and 0.088°C/sec. Glass, copper, and graphite comparative operating lifetimes were 4, 8.5, and 11.5 hours, respectively.

Conflict of Interests

The authors declare that there is no conflict of interests regarding the publication of this paper.

Acknowledgments

This work is sponsored by the Ministry of Science and Technology of Taiwan, Projects NSC99-2221-E-235-005, NSC101-2221-E-235-008, and NSC102-2221-E-150-066-MY2. Special

thanks are due to Shu-Ling Yeh researcher team from Material and Chemical Research Laboratories, Industrial Technology Research Institute, for the UV glue (YCD91).

References

- [1] M. Pope, H. P. Kallmann, and P. Magnante, "Electroluminescence in organic crystals," *The Journal of Chemical Physics*, vol. 38, no. 8, pp. 2042–2043, 1963.
- [2] A. Kraft, A. C. Grimsdale, and A. B. Holmes, "Electroluminescent conjugated polymers—seeing polymers in a new light," *Angewandte Chemie International Edition*, vol. 37, no. 4, pp. 402–428, 1998.
- [3] C. W. Tang and S. S. van Slyke, "Organic electroluminescent diodes," *Applied Physics Letters*, vol. 51, no. 12, pp. 913–915, 1987.
- [4] C. W. Tang, S. A. van Slyke, and C. H. Chen, "Electroluminescence of doped organic thin films," *Journal of Applied Physics*, vol. 65, no. 9, pp. 3610–3616, 1989.
- [5] J. J. Burroughes, D. D. C. Bradley, A. R. Brown et al., "Light-emitting diodes based on conjugated polymers," *Nature*, vol. 347, pp. 539–541, 1990.
- [6] G. Gustafsson, Y. Cao, G. M. Treacy, F. Klavetter, N. Colaneri, and A. J. Heeger, "Flexible light-emitting diodes made from soluble conducting polymers," *Nature*, vol. 357, no. 6378, pp. 477–479, 1992.
- [7] C. J. Lee, D. G. Moon, and J. I. Han, "Sports over a distance, portraits with a sense of their personal space, and telephones crossed with flotation tanks," in *Proceedings of the 3rd Workshop on Social Intelligence Design (SID '04)*, p. 1005, Seattle, DC, USA, May 2004.
- [8] C. C. Wu, S. D. Theiss, G. Gu et al., "Integration of organic LED's and amorphous Si TFT's onto flexible and lightweight metal foil substrates," *IEEE Electron Device Letters*, vol. 18, no. 12, pp. 609–612, 1997.
- [9] P. N. M. dos Anjos, H. Aziz, N.-X. Hu, and Z. D. Popovic, "Temperature dependence of electroluminescence degradation in organic light emitting devices without and with a copper phthalocyanine buffer layer," *Organic Electronics*, vol. 3, no. 1, pp. 9–13, 2002.
- [10] K. S. Rao and Y. N. Mohapatra, "Disentangling degradation and auto-recovery of luminescence in Alq₃ based organic light emitting diodes," *Journal of Luminescence*, vol. 145, pp. 793–796, 2014.
- [11] Y. Tsai, S. Wang, C. Chen et al., "Using copper substrate to enhance the thermal conductivity of top-emission organic light-emitting diodes for improving the luminance efficiency and lifetime," *Applied Physics Letters*, vol. 95, no. 23, Article ID 233306, 2009.

Research Article

Improvement in Brightness Uniformity by Compensating for the Threshold Voltages of Both the Driving Thin-Film Transistor and the Organic Light-Emitting Diode for Active-Matrix Organic Light-Emitting Diode Displays

Ching-Lin Fan,^{1,2} Hao-Wei Chen,² Hui-Lung Lai,¹ Bo-Liang Guo,¹ and Bohr-Ran Huang^{1,2}

¹ Department of Electronic and Computer Engineering, National Taiwan University of Science and Technology, Taipei 106, Taiwan

² Graduate Institute of Electro-Optical Engineering, National Taiwan University of Science and Technology, Taipei 106, Taiwan

Correspondence should be addressed to Ching-Lin Fan; clfan@mail.ntust.edu.tw

Received 14 February 2014; Revised 18 April 2014; Accepted 29 April 2014; Published 24 June 2014

Academic Editor: Liang-Sheng Liao

Copyright © 2014 Ching-Lin Fan et al. This is an open access article distributed under the Creative Commons Attribution License, which permits unrestricted use, distribution, and reproduction in any medium, provided the original work is properly cited.

This paper proposes a novel pixel circuit design and driving method for active-matrix organic light-emitting diode (AM-OLED) displays that use low-temperature polycrystalline-silicon thin-film transistors (LTPS-TFTs) as driving element. The automatic integrated circuit modeling simulation program with integrated circuit emphasis (AIM-SPICE) simulator was used to verify that the proposed pixel circuit, which comprises five transistors and one capacitor, can supply uniform output current. The voltage programming method of the proposed pixel circuit comprises three periods: reset, compensation with data input, and emission periods. The simulated results reflected excellent performance. For instance, when $\Delta V_{TH} = \pm 0.33$ V, the average error rate of the OLED current variation was low ($< 0.8\%$), and when $\Delta V_{TH,OLED} = +0.33$ V, the error rate of the OLED current variation was 4.7%. Moreover, when the $I \times R$ (current \times resistance) drop voltage of a power line was 0.3 V, the error rate of the OLED current variation was 5.8%. The simulated results indicated that the proposed pixel circuit exhibits high immunity to the threshold voltage deviation of both the driving poly-Si TFTs and OLEDs, and simultaneously compensates for the $I \times R$ drop voltage of a power line.

1. Introduction

The most critical advantage of organic light-emitting diode (OLED) displays over conventional liquid crystal displays (LCD) is that OLED displays do not require backlight module systems. OLED displays can exhibit high contrast, wide viewing angle, fast response time, and low power consumption. Moreover, OLED panels can be thinner and lighter than LCD panels [1–3]. OLED displays are currently designed to use passive-matrix (PM) or active-matrix (AM) modes. PM-OLED displays use a grid to supply charges to a pixel, and AM-OLED displays use low-temperature polycrystalline-silicon thin-film transistors (LTPS-TFTs) to provide a driving current. AM-OLED displays are becoming increasingly popular because they provide more favorable high image contrast and performance than PM-OLED displays do [1]. Moreover,

AM-OLEDs have the advantage of using less driving current compared with PM-OLEDs, which can increase the lifetime of OLED materials [1].

AM-OLEDs differ from LCDs because the value of the current flowing through the lighting element controls the luminance of each lighting element; that is, AM-OLEDs use current-controlled lighting elements. Thus, the brightness of an OLED is proportional to the amount of current passing through the diode. To obtain a uniform distribution of brightness, AM-OLED displays must uniformly deliver current to the OLED. However, the inevitable variation in the excimer laser annealing (ELA) process, which is used to form the poly-Si channel, causes a wide variety of electrical characteristics in individual LTPS-TFTs, resulting in a nonuniform driving current [4]. Furthermore, electrical performance degradation of AM-OLEDs caused by long-term operation decreases their

brightness, which can be the threshold voltage degradation of driving TFTs (DTFTs) and OLEDs in a pixel circuit [5, 6]. The voltage drop across the parasitic resistance of a power line, called $I \times R$ (current \times resistance) drop voltage, also causes nonuniform brightness in AM-OLED panels [7]. These differences in the threshold voltages of DTFTs and OLEDs and the $I \times R$ drop voltage of a power line cause different currents flowing into the OLED among the pixels. Tightening the threshold voltage variation and preventing the luminance degradation of OLEDs are very crucial to AM-OLED technology. It is reported that the two-TFT and one-capacitor (2T1C) pixel circuit suffers from pixel-to-pixel luminance nonuniformity because of the threshold voltage variation of DTFTs (shown in Figure 1). This issue is exacerbated as the size of a display increases. Instead of improving TFT processes, several studies have attempted to reduce the brightness variation across display panels by altering pixel circuit designs, which can use voltage driving, current driving, and digital driving compensation approaches [8–15]. The current driving method can minimize the shift in the DTFT threshold voltage; however, it requires a longer pixel charging time than that of voltage driving method because of the high parasitic capacitance of a data line. The digital compensation has two methods, such as area ratio grayscale method and time ratio grayscale method. These two methods have an advantage that OLED current can be partly uniform against the variation of the DTFT characteristic. However, the grayscale numbers of area ratio grayscale method and time ratio grayscale method are limited by the subarea number and the subframe number, respectively. Nowadays, the grayscale of display has already become a huge amount, so the digital methods were not suitable for application on the high resolution for AMOLED [15]. The voltage driving method can effectively manage the threshold voltage shift and also solve the nonuniform brightness problem. However, most studies have not simultaneously compensated for the threshold voltage variation of DTFTs and OLEDs and the $I \times R$ drop voltage [8–15].

This paper proposes a novel voltage programming AM-OLED pixel circuit to produce displays with uniform brightness. The proposed pixel circuit, which comprises five n-type LTPS-TFTs and one capacitor, can compensate for the nonuniformity of OLED currents caused by the threshold voltage variations of DTFTs and OLEDs. The pixel circuit can also simultaneously compensate for the OLED luminance degradation caused by the $I \times R$ drop voltage of a power line. The simulation results indicated that the proposed pixel circuit successfully supplies a highly stable OLED current and is suitable for larger AM-OLED displays.

2. Operation of the New Proposed Voltage Programming Pixel Circuit

To achieve a stable OLED current even through the DTFTs and OLEDs producing threshold voltage variations, a five-TFT and one-capacitor pixel circuit was designed. Figure 2(a) shows a schematic of the proposed pixel circuit, which includes one DTFT, four switching TFTs (Sw1 to Sw4), one

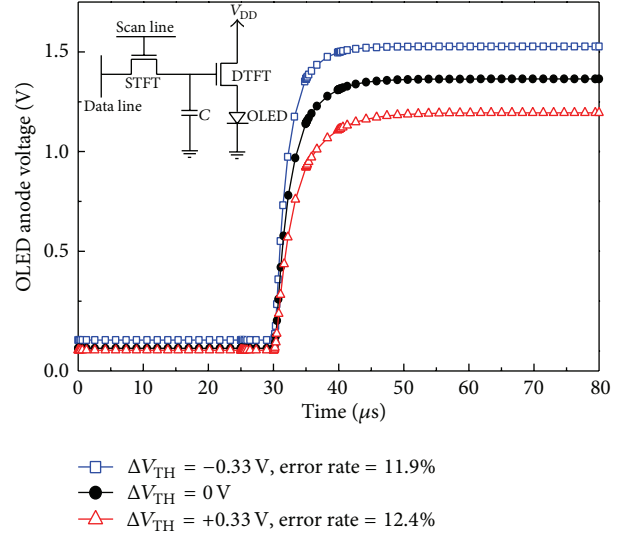


FIGURE 1: Anode voltages of OLEDs at various DTFT threshold voltage shifts ($\Delta V_{TH} = -0.33, 0, \text{ and } +0.33 \text{ V}$) for the conventional two-TFT driving scheme when $V_{DATA} = 3 \text{ V}$.

storage capacitor (C_{ST}), one OLED, and three signal lines (V_{SCAN1} , V_{SCAN2} , and V_{DATA}). Sw1 is used to turn the DTFT into a diode-connected structure; Sw2 detects the voltage between the gate and the drain (V_{GD}) in the DTFT; Sw3 controls the emission stage of the OLED; Sw4 is used to control data input. V_{SCAN1} and V_{SCAN2} are the control signals used to turn the switching TFTs (Sw1 to Sw4) on or off. V_{DATA} represents a data-voltage signal and V_{DD} refers to a constant-voltage source. The control-signal timing diagram for the proposed circuit is divided into three stages, as shown in Figure 2(b). The three circuit operations stages are Periods ①, ②, and ③, which refer to a reset period, a compensation period with data input, and an emission period, respectively. The equivalent circuits at each operation stage are shown in Figure 3. The operational method and compensation principle that apply to the proposed pixel circuit are described as follows.

2.1. Reset Period. The functions in this stage are precharging and resetting the voltage stored in C_{ST} . V_{SCAN1} and V_{SCAN2} are high and V_{DATA} is low; therefore, Sw1, Sw2, Sw3, and Sw4 are turned on. The voltage located at Node A is charged to V_{RESET} through Sw1 and Sw2. The voltage previously stored in C_{ST} is reset; therefore, the gate voltage of the DTFT connected to C_{ST} is also reset for initialization. This stage can be used to reset gate voltage of DTFT which is composed of the V_{DATA} and the compensated voltage in the previous emission period. In addition, the charging current will flow through the OLED in the reset period to cause the decreased contrast ratio except that extra scan lines for switch TFTs are added in the circuit [11, 16].

2.2. Compensation Period with Data Input. In this stage, the threshold voltage of the DTFT (V_{TH}) is detected by the

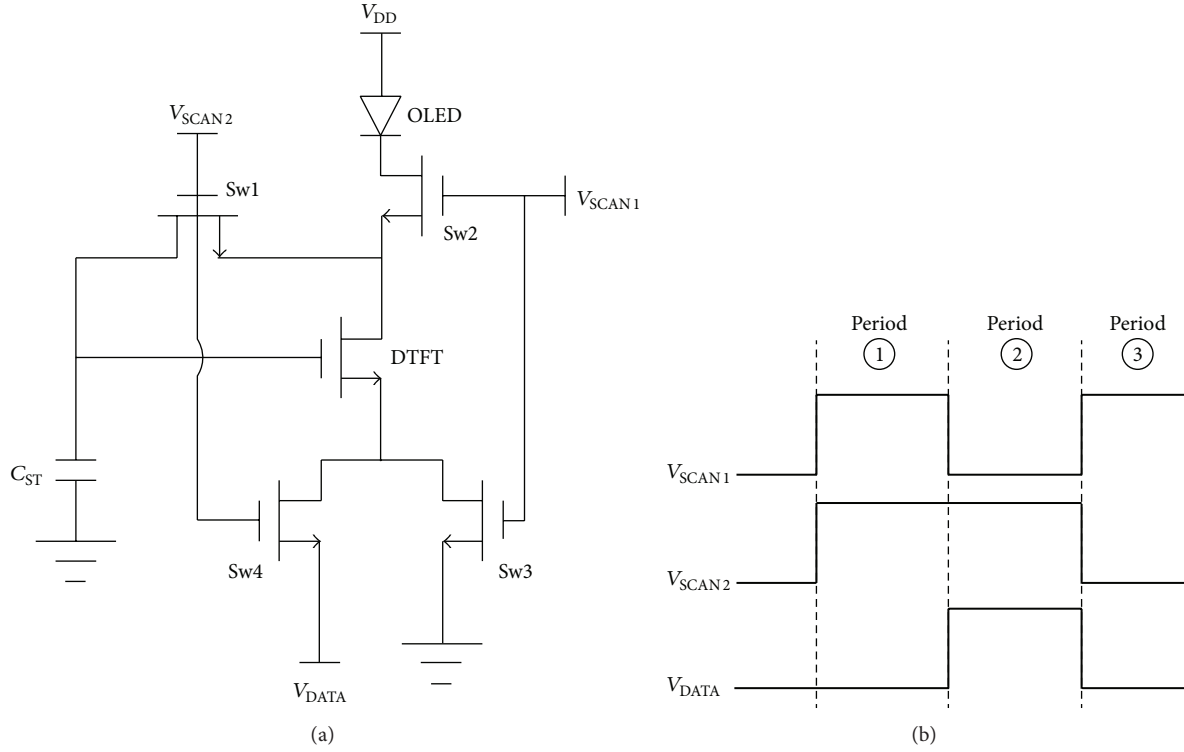


FIGURE 2: (a) Schematic diagram of the proposed pixel circuit and (b) its control-signal timing diagram.

compensation operation. When V_{SCAN1} returns to a low value, Sw2 and Sw3 are turned off. When V_{SCAN2} remains high, Sw1 and Sw4 stay on. At this moment, when a data voltage (V_{DATA}) is applied, the voltage at the source electrode of DTFT becomes V_{DATA} and the gate electrode of DTFT is charged to a higher potential, which is sufficiently high not to interfere with the compensation operation at this stage. Hence, the gate voltage of DTFT (V_A) is discharged through Sw1, DTFT, and Sw4 until the DTFT is turned off. The gate voltage of DTFT that has a diode-connect structure reaches $V_{DATA} + V_{TH}$, where V_{TH} is the DTFT threshold voltage. Because Node B is set to ground, the voltage across C_{ST} can be written as $V_A - V_B = V_{DATA} + V_{TH}$.

2.3. Emission Period. During the emission stage, when V_{SCAN1} becomes high, this turns on Sw2 and Sw3. V_{SCAN2} then returns to a low value, Sw1 and Sw4 are turned off, and V_{DATA} also decreases to a low value. Capacitor C_{ST} maintains the gate voltage of DTFT ($V_{DATA} + V_{TH}$) until the reset stage of next operation cycle. The OLED current (I_{OLED}), which equals the drain current of DTFT in the saturation region, can be written as

$$\begin{aligned}
 I_{OLED} &= \frac{1}{2} K_{DTFT} (V_{GS,DTFT} - V_{TH})^2 \\
 &= \frac{1}{2} K_{DTFT} ((V_{DATA} + V_{TH}) - V_{TH})^2 \quad (1) \\
 &= \frac{1}{2} K_{DTFT} (V_{DATA})^2,
 \end{aligned}$$

where

$$K_{DTFT} = \mu C_{ox} \frac{W}{L}. \quad (2)$$

Thus, I_{OLED} is independent of the DTFT and OLED threshold voltages and is only affected by the data voltage (V_{DATA}). The proposed pixel circuit effectively compensates for both the DTFT and OLED threshold voltage shifts and improves the display image quality for AM-OLED displays.

3. Simulation Result and Discussion

AIM-SPICE was used to simulate the proposed pixel circuit to investigate the compensation capability of the threshold voltage shifts of DTFTs and OLEDs. The AIM-SPICE poly-Si TFT model, poly-Si TFT model PSIA2 (level 16), was used in the simulation. The OLED was modeled using a diode-connected poly-Si TFT and a capacitor. Table 1 shows the simulation parameters. The simulated I - V curves of the poly-Si TFT (DTFT) and OLED with the parameters of Table 1 are shown in Figures 4(a) and 4(b), respectively.

Figure 5 shows the transient waveforms of each DTFT node when the data voltage (V_{DATA}) is 3 V. At the compensation stage with data input (Period ②), the DTFT gate voltage is discharged to $V_{DATA} + V_{TH} = 4$ V, where V_{TH} is the DTFT threshold voltage. During the emission stage (Period ③), the DTFT gate voltage is maintained at 4 V ($V_{DATA} + V_{TH}$) as the DTFT V_{GS} . Thus, the proposed circuit successfully compensates for the threshold voltage degradation of DTFTs

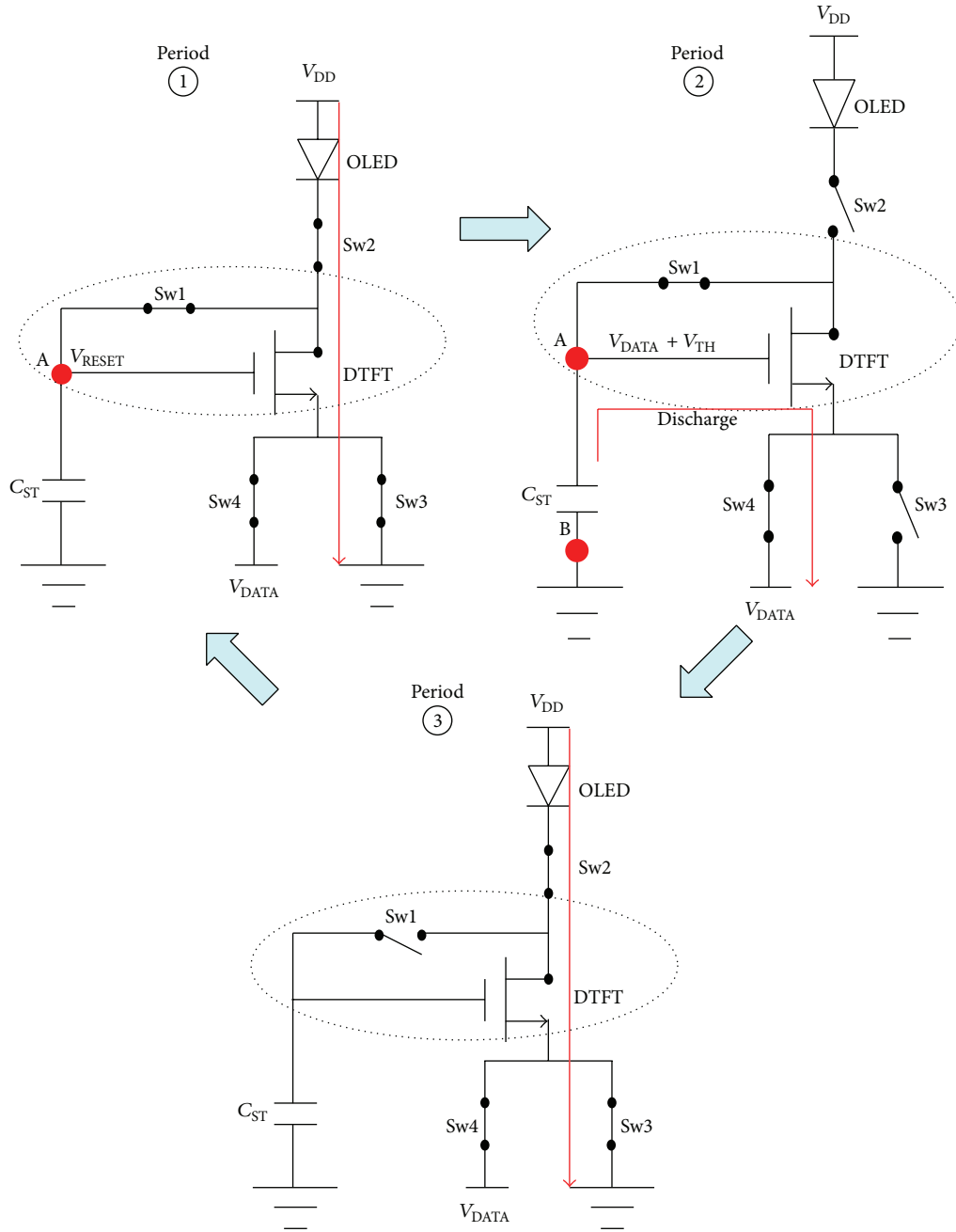


FIGURE 3: Equivalent circuits at each operation stage.

TABLE 1: Simulation parameters of the proposed pixel circuit.

Devices			
W/L (Sw1~Sw4) (μm)	8/2	V_{TH} (DTFT) (V)	1
W/L (DTFT) (μm)	12/2	$V_{TH,OLED}$ (OLED) (V)	1
C_{ST} (pF)	0.35	C_{OLED} (pF)	1
μ_{FET} (cm^2/Vs)			51.48
Signal line			
V_{SCAN1} (V)	-3 to 15	V_{DATA} (V)	1 to 4.5
V_{SCAN2} (V)	-3 to 15	V_{DD} (V)	12

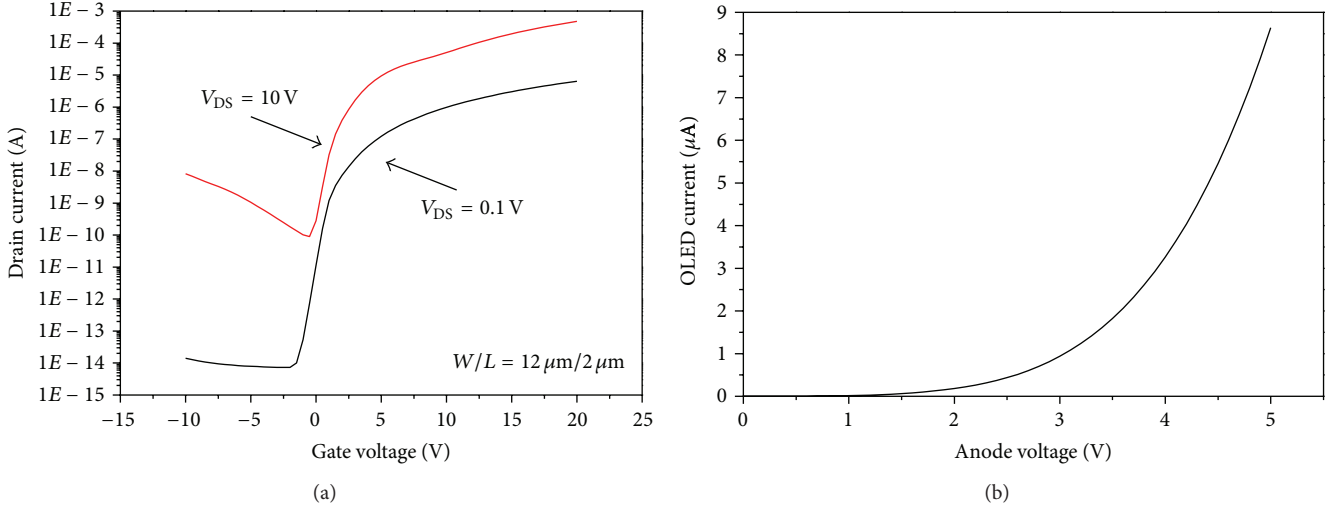


FIGURE 4: (a) The simulated I_{DS} - V_{GS} curves of the poly-Si TFT (DTFT) and (b) the I - V curve of the OLED.

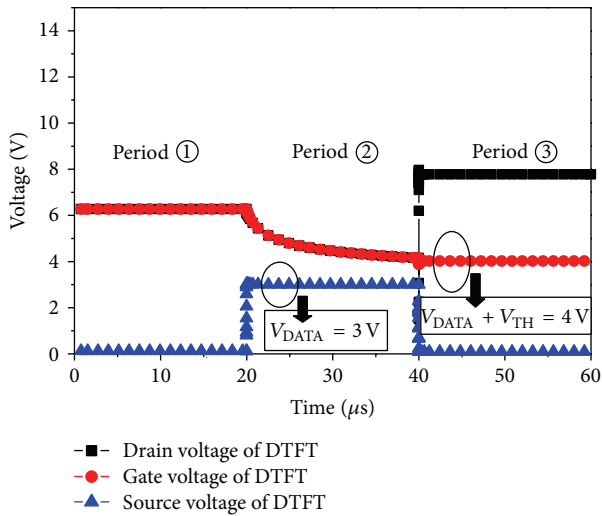


FIGURE 5: Gate, source, and drain voltages of DTFTs during different operation stages.

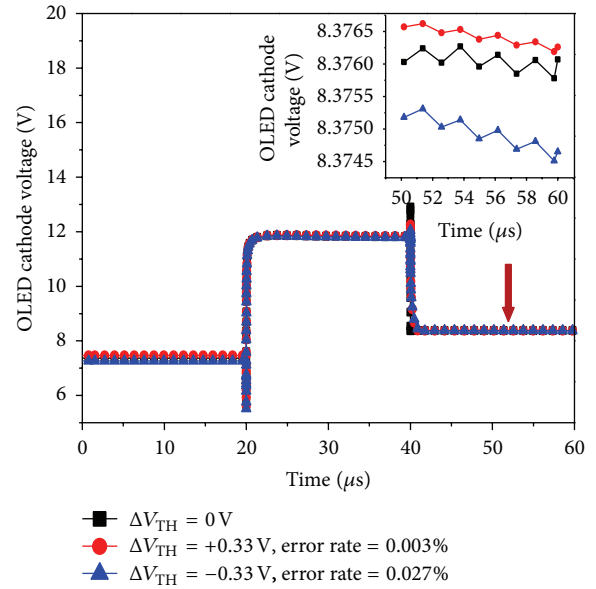


FIGURE 6: Cathode voltages of OLEDs at various DTFT threshold voltage shifts ($\Delta V_{TH} = -0.33, 0,$ and $+0.33$ V). The inset indicates that the variation is less than 0.005 V during the emission period.

and OLEDs. Figure 6 shows the simulated transient results obtained by varying the DTFT threshold voltage ($\Delta V_{TH} = -0.33, 0,$ and $+0.33$ V). The OLED cathode voltage was insensitive to the DTFT threshold voltage deviation. The error rates of the OLED cathode voltage when $\Delta V_{TH} = 0$ and ± 0.33 V were all below 0.03%. Therefore, the current flowing through the OLED was uniform. Thus, the proposed pixel circuit reduced the effect of DTFT and OLED threshold voltage deviations.

The OLED driving current affects the OLED luminance and represents the display brightness. The simulation results indicated that the DTFT threshold voltage deviation caused

the OLED current variation. The error rate of the OLED current (I_{OLED}) is defined as the difference between the shifted OLED driving current ($\Delta V_{TH} = \pm 0.33$ V) and the normal OLED current ($\Delta V_{TH} = 0$ V), as shown in the following equation:

Error rate

$$= \frac{I_{OLED}(\Delta V_{TH} = \pm 0.33 \text{ V}) - I_{OLED}(\Delta V_{TH} = 0 \text{ V})}{I_{OLED}(\Delta V_{TH} = 0 \text{ V})} \quad (3)$$

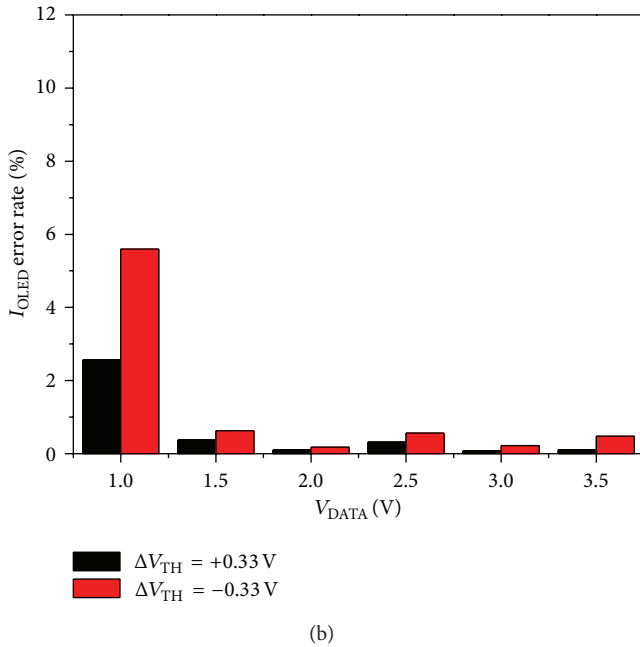
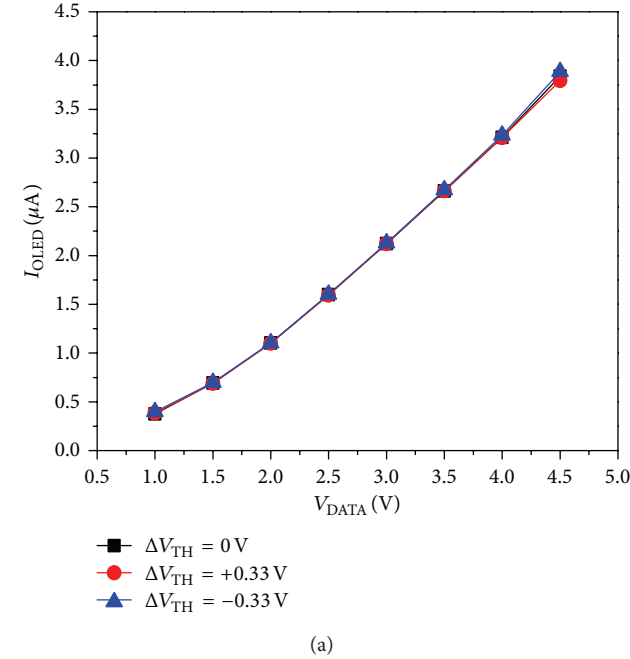


FIGURE 7: (a) OLED current (I_{OLED}) and (b) I_{OLED} error rate when $\Delta V_{\text{TH}} = \pm 0.33$ V at various data voltage.

Figures 7(a) and 7(b) present the OLED currents (I_{OLED}) and their error rates when $\Delta V_{\text{TH}} = \pm 0.33$ V at various data voltage, respectively. The figures clearly indicate that the average I_{OLED} error rate is below 0.8% for the proposed circuit. The average error rates of conventional 2T1C and other published pixel circuits are approximately 30% and 5%, respectively [10–12]. Therefore, the display image quality of panels that use the proposed pixel circuit will be more uniform than conventional 2T1C and reported pixel circuits.

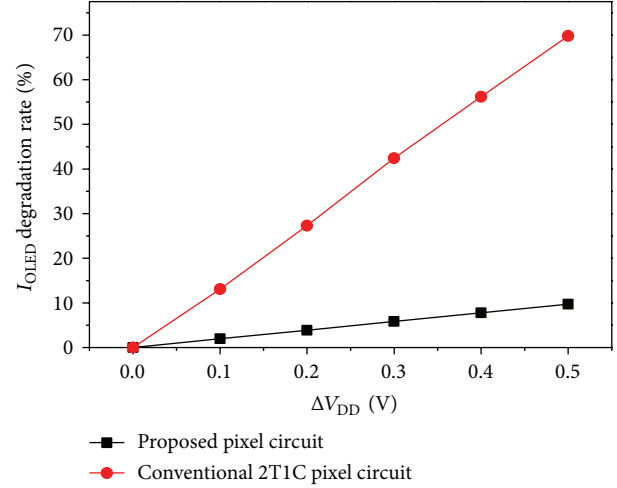


FIGURE 8: Proposed pixel circuit I_{OLED} degradation rate, compared with the degradation rate of conventional 2T1C pixel circuit, when the range of the $I \times R$ drop voltage of a power line (ΔV_{DD}) is 0.5 V.

Figure 8 presents the simulation results of the I_{OLED} degradation rates of the proposed circuit and the conventional 2T1C pixel circuit when the range of the $I \times R$ drop voltage of a power line (ΔV_{DD}) is 0.5 V. The initial V_{DD} value was set to 12 V and the $I \times R$ drop voltage (ΔV_{DD}) was set to 0.5 V; that is, the V_{DD} decayed from 12 V to 11.5 V. In conventional 2T1C pixel circuit, the I_{OLED} degradation rate is approximately 70% to 80%. The proposed pixel circuit can improve the I_{OLED} degradation rate caused by the $I \times R$ drop voltage of a power line. In addition, the I_{OLED} degradation rate when ΔV_{DD} was 0.3 V improved to approximately 5.8%. This demonstrates that the proposed pixel circuit can effectively solve the issue of $I \times R$ drop voltage.

Figures 9(a) and 9(b) present the I_{OLED} value and its error rate when the degradation of the OLED threshold voltage ($\Delta V_{\text{TH, OLED}}$) is +0.33 V at a range of data voltages between 1 V and 4.5 V, respectively. After long-term operation, the OLED threshold voltage ($V_{\text{TH, OLED}}$) increases, causing the brightness and quality of the display to deteriorate. As shown in Figure 9(b), the proposed pixel circuit can compensate for OLED degradation and the average I_{OLED} error rate was 4.7%. Therefore, the display image uniformity improved as a result of the decreased I_{OLED} error rate.

4. Conclusions

This study proposed a voltage programming pixel circuit for AM-OLED displays and verified the circuit using the AIM-SPICE simulator. The proposed circuit was composed of five TFTs and one capacitor and it simultaneously compensated for the threshold voltage variations of DTFTs and OLEDs and the $I \times R$ drop voltage of a power line. The simulation results demonstrated that the average error rates of the OLED current when $\Delta V_{\text{TH}} = \pm 0.33$ V for DTFTs and $\Delta V_{\text{TH, OLED}} = +0.33$ V for the OLEDs were less than 1% and 5%, respectively. The average error rate was also less sensitive to the $I \times R$ drop voltage of a power line. Therefore, the proposed circuit

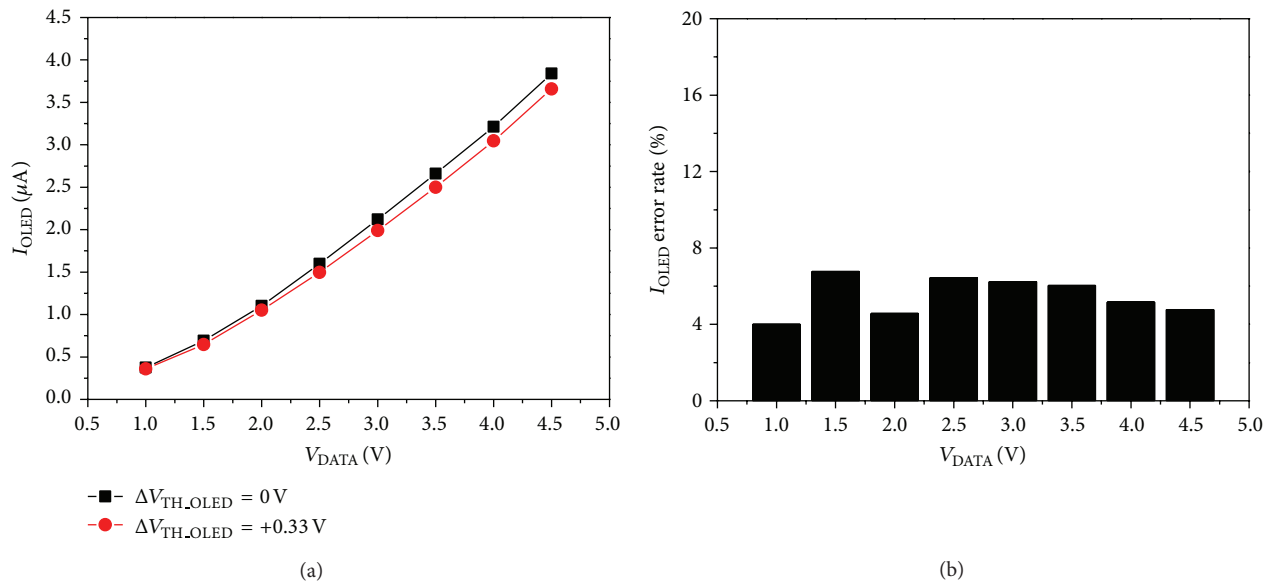


FIGURE 9: (a) I_{OLED} and (b) I_{OLED} error rate when the degradation of the OLED threshold voltage ($\Delta V_{\text{TH,OLED}}$) is +0.33 V, with a voltage range between 1 V and 4.5 V.

exhibited high immunity to the threshold voltage deviation of both DTFTs and OLEDs and improved the brightness uniformity of AM-OLED displays.

Conflict of Interests

The authors declare that there is no conflict of interests regarding the publication of this paper.

Acknowledgments

The authors would like to acknowledge the financial support of the National Science Council of Taiwan under Contract nos. NSC 101-2221-E-011-070 and NSC 102-2221-E-011-112-MY2 and of the Taiwan Building Technology Center (TBTC) of National Taiwan University of Science and Technology (NTUST).

References

- [1] M. Stewart, R. S. Howell, L. Pires, M. K. Hatalis, W. Howard, and O. Prache, "Polysilicon VGA active matrix OLED displays—technology and performance," in *Proceedings of IEEE International Electron Device Meeting (IEDM '98)*, pp. 871–874, December 1998.
- [2] T. Funamoto, Y. Matsueda, O. Yokoyama, A. Tsuda, H. Takeshita, and S. Miyashita, "A 130-ppi, full-color polymer OLED display fabricated using an ink-jet process," in *Proceedings of the SID Symposium Digest of Technical Papers*, pp. 899–901, 2002.
- [3] H. Lee, B. H. You, W. J. Nam, H. J. Lee, and M. K. Han, "A new a-Si:H TFT pixel design compensating threshold voltage degradation of TFT and OLED," in *Proceedings of the SID Symposium Digest of Technical Papers*, pp. 264–267, 2004.
- [4] C. L. Fan, Y. Y. Lin, B. S. Lin, J. Y. Chang, C. L. Fan, and H. C. Chang, "New pixel circuit compensating poly-si TFT threshold-voltage shift for a driving AMOLED," *Journal of the Korean Physical Society*, vol. 56, no. 4, pp. 1185–1189, 2010.
- [5] H. Aziz, "Degradation mechanism of small molecule-based organic light-emitting devices," *Science*, vol. 283, no. 5409, pp. 1900–1902, 1999.
- [6] J. Zhou, M. Wang, and M. Wong, "Two-stage degradation of p-channel poly-Si thin-film transistors under dynamic negative bias temperature stress," *IEEE Transactions on Electron Devices*, vol. 58, no. 9, pp. 3034–3041, 2011.
- [7] S.-H. Jung, W.-J. Nam, and M.-K. Han, "A new voltage-modulated AMOLED pixel design compensating for threshold voltage variation in Poly-Si TFTs," *IEEE Electron Device Letters*, vol. 25, no. 10, pp. 690–692, 2004.
- [8] A. Nathan, G. R. Chaji, and S. J. Ashtiani, "Driving schemes for a-Si and LTPS AMOLED displays," *IEEE/OSA Journal of Display Technology*, vol. 1, no. 2, pp. 267–277, 2005.
- [9] Yumoto, M. Asano, H. Hasegawa, and M. Sekiya, "Pixel-driving methods for large-sized poly-Si AM-OLED displays," in *Proceedings of International Display Workshops*, pp. 1395–1398, 2001.
- [10] C.-L. Fan, Y.-Y. Lin, J.-Y. Chang, B.-J. Sun, and Y.-W. Liu, "A new low temperature polycrystalline silicon thin film transistor pixel circuit for active matrix organic light emitting diode," *Japanese Journal of Applied Physics*, vol. 49, no. 6, pp. 0642011–0642015, 2010.
- [11] C.-L. Lin and Y.-C. Chen, "A novel LTPS-TFT pixel circuit compensating for TFT threshold-voltage shift and OLED degradation for AMOLED," *IEEE Electron Device Letters*, vol. 28, no. 2, pp. 129–131, 2007.
- [12] H.-J. In and O.-K. Kwon, "External compensation of non-uniform electrical characteristics of thin-film transistors and degradation of OLED devices in AMOLED displays," *IEEE Electron Device Letters*, vol. 30, no. 4, pp. 377–379, 2009.

- [13] W.-J. Wu, L. Zhou, R.-H. Yao, and J.-B. Peng, "A new voltage-programmed pixel circuit for enhancing the uniformity of AMOLED displays," *IEEE Electron Device Letters*, vol. 32, no. 7, pp. 931–933, 2011.
- [14] W.-J. Wu, L. Zhou, M. Xu, L.-R. Zhang, R.-H. Yao, and J.-B. Peng, "An AC driving pixel circuit compensating for tfts threshold-voltage shift and oled degradation for amoled," *IEEE/OSA Journal of Display Technology*, vol. 9, no. 7, pp. 572–576, 2013.
- [15] M. Kimura, Y. Hara, H. Hara, T. Okuyama, S. Inoue, and T. Shimoda, "Classification of driving methods for TFT-OLEDs and novel proposal using time ratio grayscale and current uniformization," *IEICE Transactions on Electronics*, vol. E88-C, no. 11, pp. 2043–2050, 2005.
- [16] C.-L. Lin, C.-C. Hung, W.-Y. Chang, M.-H. Cheng, P.-Y. Kuo, and Y.-C. Chen, "Voltage driving scheme using three TFTs and one capacitor for active-matrix organic light-emitting diode pixel circuits," *IEEE/OSA Journal of Display Technology*, vol. 8, no. 10, pp. 602–608, 2012.

Research Article

OLED Fabrication by Using a Novel Planar Evaporation Technique

Fu-Ching Tung,^{1,2} Yi-Shan Wang,² Shih-Hsiang Lai,² Chien-Chih Chen,² Szu-Hao Chen,² Ching-Chiun Wang,² Jwo-Huei Jou,¹ and Sun-Zen Chen³

¹ Department of Materials Science and Engineering, National Tsing Hua University, Hsinchu 30013, Taiwan

² Mechanical and Systems Research Laboratories, Industrial Technology Research Institute, Hsinchu 31040, Taiwan

³ Center for Nanotechnology, Materials Science, and Microsystems, National Tsing Hua University, Hsinchu 30013, Taiwan

Correspondence should be addressed to Fu-Ching Tung; fc tung@itri.org.tw and Jwo-Huei Jou; jjou@mx.nthu.edu.tw

Received 13 March 2014; Revised 15 May 2014; Accepted 23 May 2014; Published 22 June 2014

Academic Editor: Liang-Sheng Liao

Copyright © 2014 Fu-Ching Tung et al. This is an open access article distributed under the Creative Commons Attribution License, which permits unrestricted use, distribution, and reproduction in any medium, provided the original work is properly cited.

Organic light-emitting diode fabrication is suffering from extremely high material wasting during deposition especially using a typical point or even line source. Moreover, the need of depositing a high number of emitters and host(s) with a precise composition control in a single layer makes traditional vapor codeposition systems nearly impossible, unless otherwise with a very low yield. To improve, we have developed a novel thin-film deposition system with a planar source loadable with any premeasured solvent-mixed organic compounds, plausibly with no component number limitation. We hence demonstrate experimentally, along with a Monte Carlo simulation, in the report the feasibility of using the technique to deposit on a large area-size substrate various organic materials with a relatively high material utilization rate coupling with high film uniformity. Specifically, nonuniformity of less than $\pm 5\%$ and material utilization rate of greater than 70% have been obtained for the studied films.

1. Introduction

Organic light-emitting diodes (OLEDs) emit light when electricity is applied. They are used to create beautiful digital displays and also possible for use in solid-state lighting applications in the near future [1–3]. However, they are not the mainstream technologies yet because of the high manufacturing cost. To resolve, some key technologies need to be significantly improved, if not totally replaced.

Amongst organic thin-film deposition process is one key technology in OLEDs manufacturing. Most in use are evaporation systems equipped with a point source. Although the point source provides good film nonuniformity, in case the source-to-substrate distance is sufficiently long, the material utilization rate is known to be much less than 10% [4, 5]. The high waste of those expensive organic materials is one major cause of the current high cost in OLEDs manufacturing. This in turn obstructs the market

acceptance. The problem becomes more severe as large area-size panels are demanded. To overcome, we propose a novel evaporation system equipped with a planar source, loadable with any premeasured solvent-mixed organic compounds. It is a promising technology that can markedly improve the material utilization rate and easily scale up for deposition of large area-size substrate to enable low-cost manufacturing for OLED devices. In current study, we demonstrate a successful OLED device manufacturing by using in part the newly developed system. The new system has shown a better organic film uniformity and a higher material utilization than the conventional ones.

To assist the design of the new system, a parallel direct simulation Monte Carlo (DSMC) method [6] has been adopted in order to attain high film uniformity on a large area-size substrate for various different organic materials. The DSMC [6] method can be applied in several applications, including semiconductor related fabrication processes, fluid/thermal analysis of

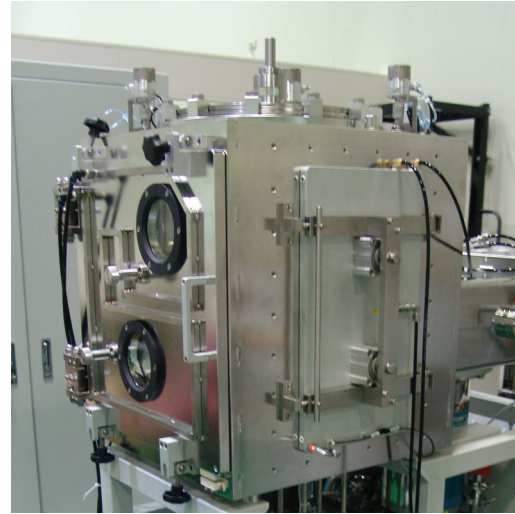
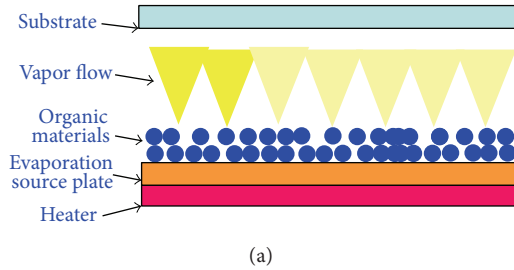


FIGURE 1: Illustration of (a) the concept and (b) photograph of the novel evaporation system.

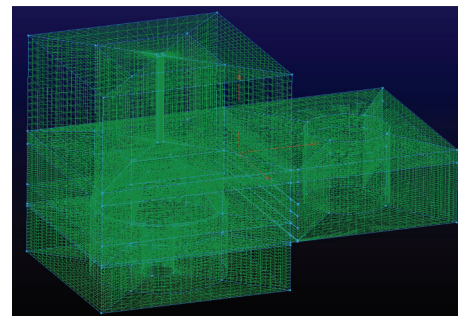
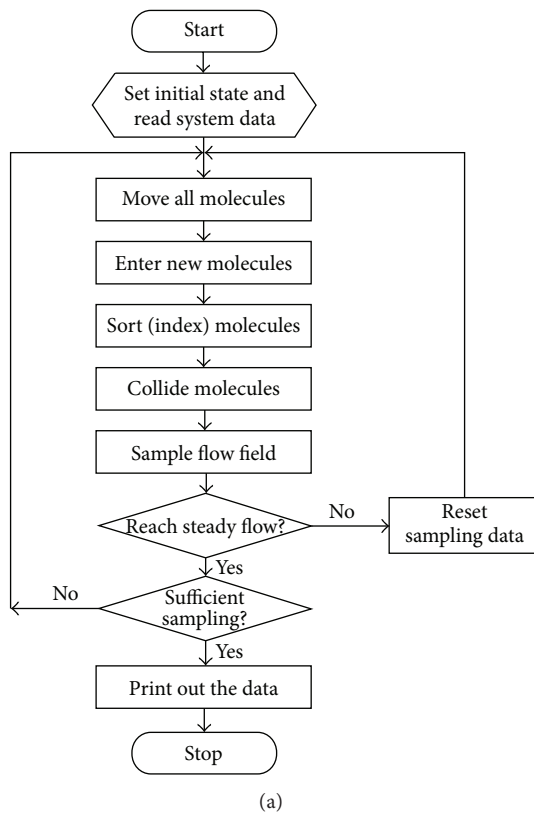


FIGURE 2: (a) Flow chart of the 3D DSMC method and (b) the 3D simulation cells.

MEMS/NEMS devices, hypersonic flow analysis, estimation of spacecraft, and scramjet engines flow. Importantly, it can also be adopted for modeling thin-film deposition process, such as, in the present case, the physical vapor evaporation of OLED, to obtain high uniformity on large area-size substrates for mixed compounds with any designated concentration [7–10].

It is learned that, via an accurate DSMC modeling, the development cost of the system can be tremendously reduced and the operational conditions of which can be rapidly optimized. It is also observed that the film uniformity is greatly improved and material utilization rate is markedly enhanced as the target-to-source (T/S) distance is decreased.

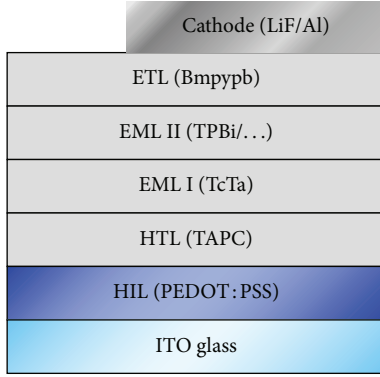


FIGURE 3: The structure of OLED device manufactured.

2. Experimental

2.1. Novel Evaporation System Equipped with a Planar Source Plate. The planar source module is illustrated in Figure 1(a) [11]. First, organic materials are deposited on the planar source plate by using a coating process. The planar source plate is then placed in a chamber. The heater under the planar source plate heats to the desired temperature, and the organic materials on the planar source plate are deposited upward onto the glass substrate. A shutter plate is set between the planar source plate and substrate to prevent the impurity from evaporating to the substrate at the initial time of the evaporation. The chamber is pumped to base pressure by using a cryopump equipped with a controlled gate valve. Figure 1(b) presents a photograph of the novel evaporation system equipped with a planar source plate.

2.2. Parallel Direct Simulation Monte Carlo Method. The direct simulation Monte Carlo (DSMC) method involves directly simulating particle collision kinetics for solving the Boltzmann equation and can automatically capture nonequilibrium phenomena without any convergence problem. This method has been widely used for simulating gas flow in rarefied gas dynamics. In addition, the parallel DSMC method can mitigate the problem of high computing power and increased computational time by simulating a large number of particles [12–15].

We applied parallel DSMC for modeling the transport phenomena and film deposition in an OLED processing chamber containing the planar source plate. Although numerous particles are generated in the flow field to represent real physical gas molecules, the DSMC algorithm can be readily parallelized using physical domain decomposition. Each processor executes the DSMC algorithm in sequence for all of the particles and cells of the computational grid, which are distributed among the processors, in its domain. Data communication occurs when particles cross the domain (processor) boundaries and are then transferred between processors.

Figure 2(a) presents a simplified flow chart of the three-dimensional (3D) DSMC method used in this study. Figure 2(b) presents the 3D simulation cells of the planar source system. Table 1 lists the properties of Organic Material

TABLE 1: The properties of Organic Material A.

Item	Value
Molecular weight	459.43
Molecular mass (kg)	$7.63E - 26$
Ref. temperature (K)	273
Surface temperature ($^{\circ}\text{C}$)	155
Surface temperature (K)	428
Flux J (mole/ $\text{m}^2\cdot\text{s}$)	$8.07E - 10$
Flux n ($\#/\text{m}^2\cdot\text{s}$)	$4.86E + 14$
Mean thermal speed (m/s)	$4.44E + 02$
Number density n ($\#/\text{m}^3$)	$1.09E + 12$
Degrees of freedom ξ	3
Viscosity coefficient	$3.29E - 05$
Viscosity index ω	1.63
Reference diameter d (m)	$1.76E - 09$
Mean free path λ	$1.50E + 02$

A [11]. According to the simulation result, we modified the planar source plate used in this study to achieve optimal performance.

2.3. Methods and Device Fabrication. The thickness of the Alq3 thin films deposited using the planar source plate was measured to assess the nonuniformity of the film thickness. We deposited organic material (5, 6, 11, 12)-tetraphenylanthracene (rubrene) onto the glass substrate at varying distances between the target substrate and planar source plate (T/S) to measure the material utilization of the planar source plate.

Figure 3 presents the structure of the fabricated OLED device. The substrate size is 5×5 cm.

First, we fabricated a hole-injection layer (HIL) on a pre-cleaned indium tin oxide (ITO) anode by spin-coating an aqueous solution of poly(3,4-ethylene-dioxythiophene)-poly(styrenesulfonate) (PEDOT:PSS) in nitrogen.

The hole-transport layer (HTL) was then deposited using the proposed system equipped with the planar source plate. We used di-[4-(N,N-ditolyl-amino)-phenyl]cyclohexane (TAPC) as the hole-transport material. The TAPC was dissolved in tetrahydrofuran, spray-coated onto the planar source plate at room temperature in air, and dried. The heater heated to 450°C , and the TAPC was deposited upward onto the glass substrate exhibiting a T/S gap of 5 cm at a pressure of 1.33 Pa.

The other organic and metal layers were prepared using a conventional system at approximately 1.33×10^{-3} Pa. A 4,4',4''-tris(carbazol-9-yl)-triphenylamine (TcTa) was used as the host with a small amount of blue dopant for the emissive layer (EML) I. A 1,3,5-tris(1-phenyl-1h-benzimidazol-2-yl) benzene (TPBi) was used as host with a small amount of red dopant, yellow dopant, and green dopant for the EML II. Subsequently, 1,3-bis[3,5-di(pyridin-3-yl)phenyl]benzene (Bmpypb) was prepared to form an electron-transport layer (ETL).

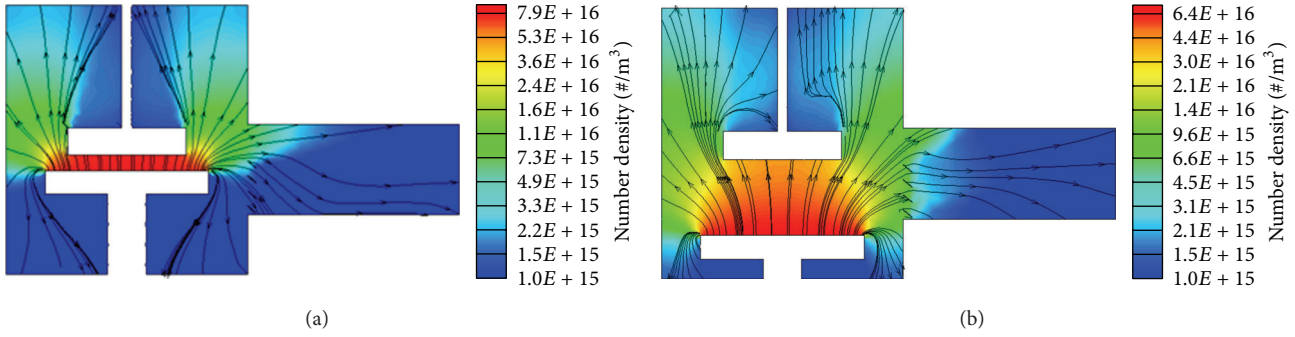


FIGURE 4: Number density distribution diagrams with (a) 30 mm and (b) 150 mm T/S distance (slice from x - y plane).

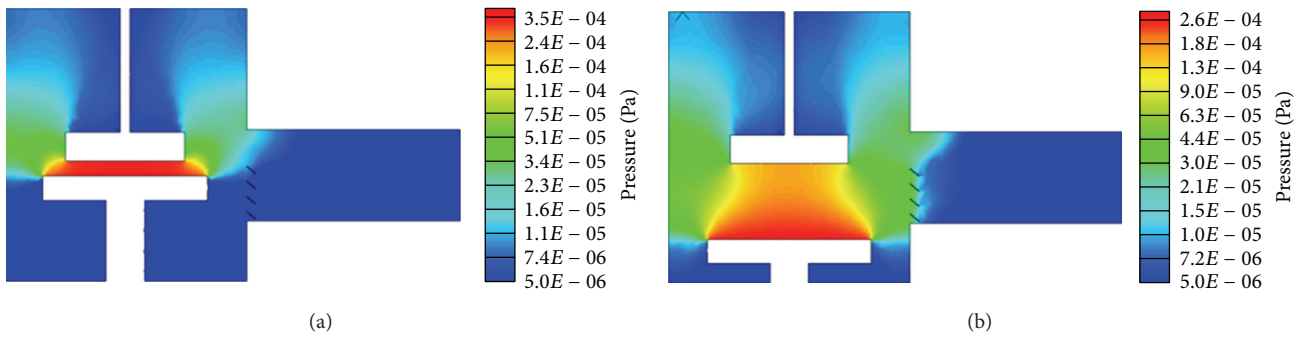


FIGURE 5: Pressure distribution diagrams with (a) 30 mm and (b) 150 mm T/S distance (slice from x - y plane).

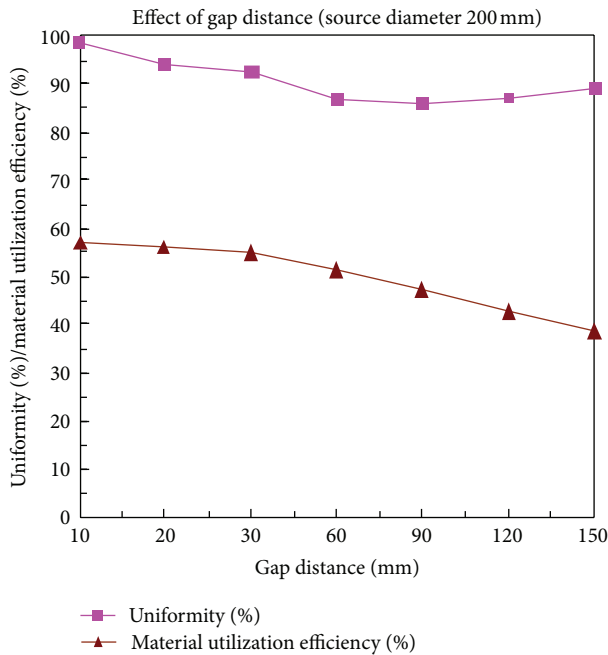


FIGURE 6: The relationship of thin-film uniformity and material utilization rate of Organic Material A at varying T/S gap distances.

Subsequently, an electron-injection layer (EIL) of lithium fluoride (LiF) and aluminum cathode was deposited using thermal evaporation at 1.33×10^{-3} Pa.

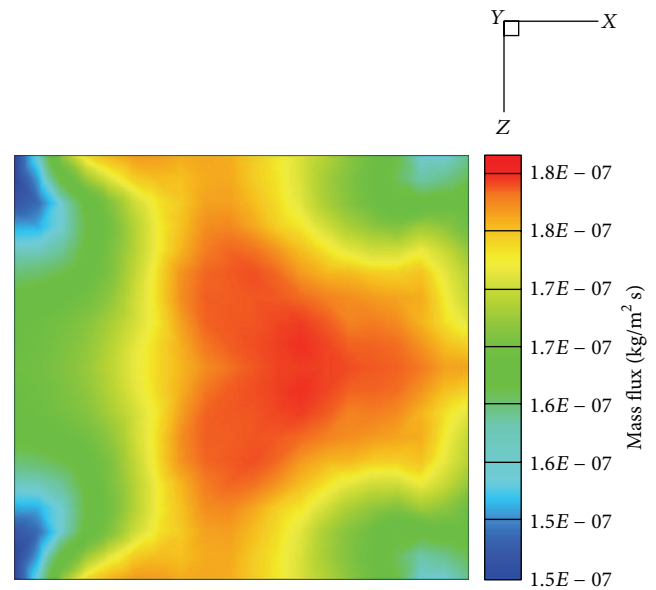


FIGURE 7: Mass flux of Organic Material A.

Luminance, chromaticity, and electroluminescence spectra of the OLEDs were recorded using a PR-650 SpectraScan Colorimeter. The current-voltage characteristics were measured using a Keithley 2400 source meter. All of the measurements were performed at room temperature in air.

TABLE 2: Thickness of the “Alq3” thin films deposited by the planar source.

Position	1	2	3	4	5	6	7	8
Thickness (nm)	151.71	149.59	150.82	153.53	161.03	154.64	152.15	158.46

TABLE 3: Material utilization rate of the planar source.

T/S (cm)	Planar source plate weight difference (mg)	Substrate weight difference (mg)	Material utilization rate (%)
14	14.2	4.7	33.1
12	13.6	5.7	41.9
10	5.4	4.2	77.8

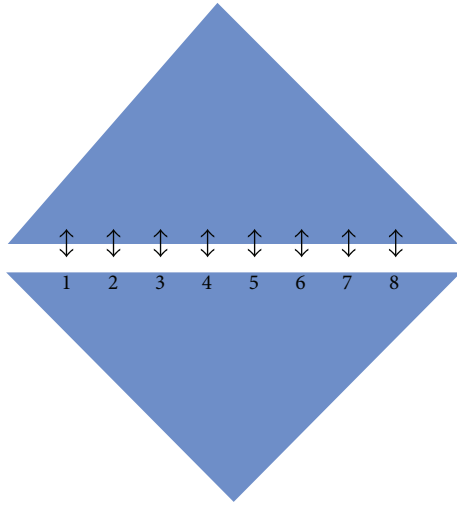


FIGURE 8: The thickness measurement positions of the substrate.

3. Results and Discussion

3.1. Parallel Direct Simulation Monte Carlo Method. Figure 4 presents the number density contour for observing the distribution from the evaporation source to the substrate. The flux of molecules from the evaporation source to the substrate is uniform when the T/S distance is equal to 30 mm. Figure 5 illustrates the pressure distribution contour for a T/S distance of (a) 30 mm and (b) 150 mm (slice from the x - y plane). The pressure distribution at a T/S distance of 30 mm is more uniform than that at a T/S distance of 150 mm [11], because tilted blade gate openings, as indicated by the “\” in Figures 4 and 5, were constructed to obstruct the flow to reduce the influence of the asymmetrical pumping system. Because the T/S gap was short and the pressure was considerably low, the influence of the asymmetrical system was reduced. Although the molecules number density and the pressure distribution were not symmetrical near the outlet region, both were symmetrical in the region of the substrate and the target. High film uniformity was thus obtained.

Figure 6 presents the relationship of thin-film uniformity and material utilization rate of Organic Material A at varying T/S gap distances. The uniformity of the thin film is more than 85% when the T/S distance ranges from 30 mm to

150 mm. The thin-film thickness uniformity and material utilization rate are high when the T/S distance is decreased, which differs from the conventional thermal evaporation system equipped with a point source.

The film uniformity can be estimated according to the mass flux of the particles passing through the substrate surface, as illustrated in Figure 7. As indicated, the mass flux is distributed from 1.5×10^{-7} to 1.8×10^{-7} kg/m²s, with most of the mass flux centered from 1.6×10^{-7} to 1.8×10^{-7} kg/m²s. Equations (1)–(3) are used to calculate the nonuniformity. Because of the high uniformity of particle distribution, the calculated film nonuniformity is only 3.5%. Consider

$$\bar{T} = \frac{1}{N} \sum_{i=1}^N t_i \quad (1)$$

$$\Delta t = \sqrt{\frac{1}{n-1} \sum_{i=1}^N (t_i - \bar{T})^2} \quad (2)$$

$$\text{UN} = \frac{\Delta t}{\bar{T}} \times 100\%, \quad (3)$$

where \bar{T} is the mass flux average, N is the total mass flux, t_i is the mass flux, Δt is the standard deviation of mass flux, and UN is the nonuniformity number.

3.2. Nonuniformity of the Film Thickness. The thin films composed of tris(8-hydroxy-quinolino) aluminum (Alq3) were deposited using the planar source plate at a distance of 5 cm between the target substrate and planar source plate (T/S).

The thickness of the Alq3 thin films was measured using the Dektak XT Surface Profiler, as indicated in Table 2 [11]. The positions measured from the 10×10 cm glass substrate are presented in Figure 8. The nonuniformity of the film thickness can be determined using (4). Consider

$$\text{Nonuniformity } (\pm\%) = \frac{(T_{\max} - T_{\min})}{2T_{\text{avg}}} \times 100\%, \quad (4)$$

where T_{\max} , T_{\min} , and T_{avg} are the maximal, minimal, and average values of the film thickness, respectively. According to (4), the nonuniformity of the Alq3 thin-film thickness was

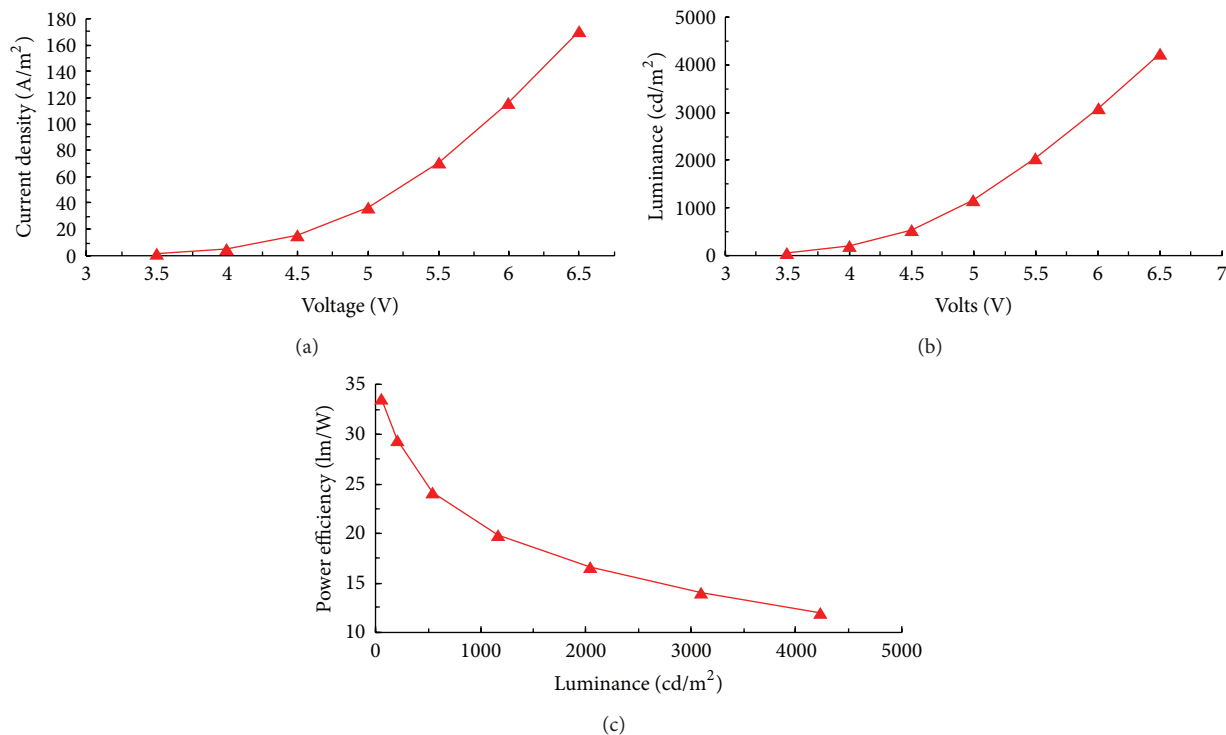


FIGURE 9: (a) The current density-voltage characteristic. (b) The brightness-voltage characteristic. (c) The power efficiency versus luminance of the OLED device.

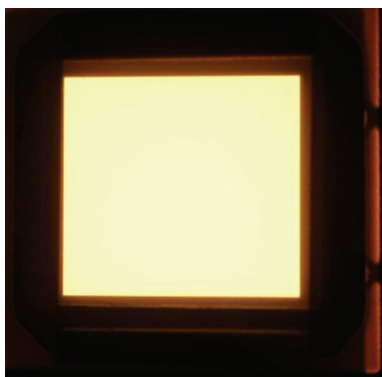


FIGURE 10: The OLED device illuminated at 3.5 V.

$\pm 3.7\%$. The uniformity can be easily attained using the planar source plate at a short T/S distance [11].

A layer using a host and a blue dye to obtain a film nonuniformity of $\pm 2.7\%$ was successfully achieved. Specifically, the film was prepared using the solvent premixing deposition method [16–19]. The film was deposited shot by shot by using the planar source. For each shot, the precise doping concentration with a favorable reproducibility was obtained by controlling the amount of solvent-mixed premeasured organic compounds. To the moment, no substantial residual materials, either single coating materials (HTL) or two materials (host and blue dye), were observed on the planar source after evaporation. This meant that most of the prepared solvent premixing materials, including the dopant

and the host, were successfully evaporated during the heating process. The conventional codeposition doping process requires an extremely low deposition rate and a highly precise deposition-time control, which is impractical and occasionally impossible. Insufficient doping or overdoping of one or more of the dyes, such as red or green dyes, frequently occurs, explaining why numerous previously reported white OLEDs have failed to yield pure white emission [16].

3.3. Material Utilization Rate. To measure the material utilization rate of the planar source plate directly, (5, 6, 11, 12)-tetraphenylanthracene (rubrene) was deposited onto the glass substrate at varying distances between the target substrate and planar source plate (T/S). We used approximately 16 mg of rubrene for each studied material in the planar source. The weight difference of the planar source plate and glass substrate was measured, as indicated in Table 3 [11]. When the T/S distance was 10 cm, the material utilization was as high as 77.8%. Based on the experimental results, the T/S distance should be as short as possible to increase the material utilization rate in the deposition processes.

A 77.8% material utilization rate was obtained using the newly developed planar source, which was much higher than the 3% to 5% rate observed when using typical point sources. Improving material utilization by a wide margin should decrease the manufacturing cost of mass production.

3.4. Characterization of the Device. We successfully fabricated OLED devices by using the HTL deposited

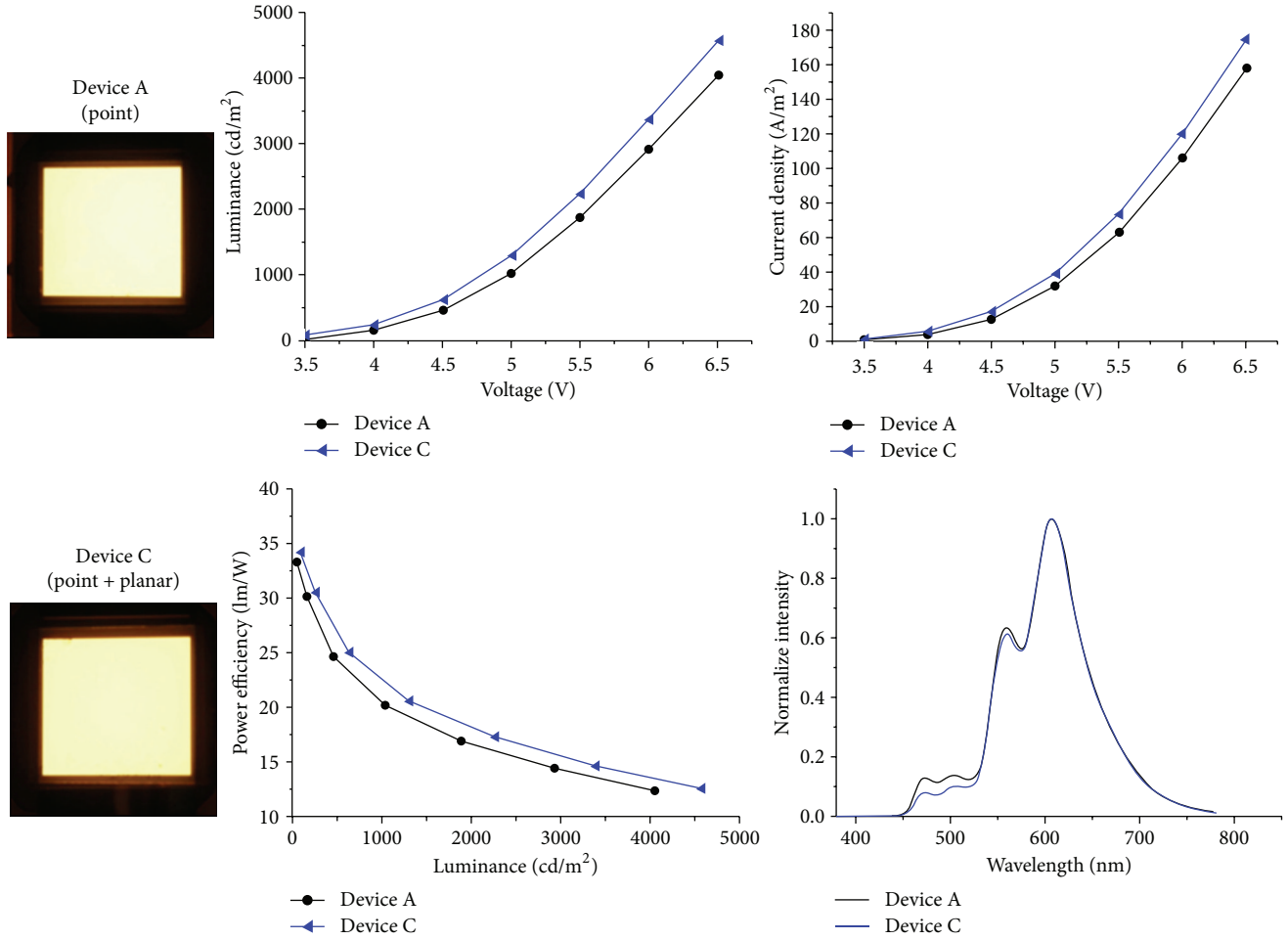


FIGURE 11: The device performance compared with that of a device prepared using a complete conventional point source.

using the proposed system equipped with a planar source plate and the other layers deposited using a conventional system.

Figure 9(a) presents the current density-voltage characteristic and Figure 9(b) presents the brightness-voltage characteristic. The current density was 31 A/m² and the brightness was 1000 cd/m² at an operation voltage of 4.85 V. Figure 9(c) presents the power efficiency versus luminance of the OLED device. The power efficiency at 1000 cd/m² is 21.1 lm/W. The device also exhibits a color rendering index (CRI) of 70 at 1000 cd/m². Figure 10 presents a photograph of the OLED device illuminated at 3.5 V.

Figure 11 presents the device performance compared with that of a device prepared by using a complete conventional point source. The characteristics of luminance, current density, and power efficiency, achieved by partially using the proposed system equipped with a planar source, were higher than those achieved using a complete conventional point source. The wavelength spectra were similar in both cases.

4. Conclusion

A new system designed with a planar source is manufactured for OLED application. A parallel DSMC method is used for modeling the process of organic material deposition of the planar source system. As the T/S distance is decreased, the film uniformity is higher, and the material utilization rate is also higher, much different from the point source based evaporation system. We can reduce the cost of the planar source development and optimize the operating conditions through accurate DSMC modeling. Using such a planar source has at least three advantages, namely, a high material utilization rate, high film uniformity, and high degree of device design freedom. To the moment, we successfully achieved a layer with a host and a blue dye with a film nonuniformity of $\pm 2.7\%$. Specifically, the film was prepared using the solvent premixing deposition method. Moreover, by using the newly developed planar source, a 77.8% material utilization rate was obtained, which is much higher than the 3% to 5% rate observed when using the typical point source. The system has enabled the organic thin films to be deposited

with a less than 5% nonuniformity and a material utilization rate of over 70%. We successfully demonstrate the fabrication of an OLED device with the hole transporting layer deposited by the new system with the planar source and the other layers deposited by the conventional system. The power efficiency of the OLED device is 21.1 lm/W with a CRI of 70 at 1,000 cd/m². The evaporation system equipped by the novel planar source can obtain large-area uniformity for thin-film evaporation and high material utilization rate of various organic materials.

Conflict of Interests

The authors declare that they have no conflict of interests regarding the publication of this paper.

Acknowledgments

The authors acknowledge Professor Jong-Shinn Wu and his laboratory team of the Department of Mechanical Engineering, National Chiao Tung University, for assisting with the DSMC method. This study was financially supported by the Taiwan Ministry of Economic Affairs through Grants nos. 102-EC-17-A-05-01-1111, D301AR3B00, and 102-EC-17-A-07-S1-181.

References

- [1] S. Reineke, F. Lindner, G. Schwartz et al., "White organic light-emitting diodes with fluorescent tube efficiency," *Nature*, vol. 459, no. 7244, pp. 234–238, 2009.
- [2] S. J. Su, E. Gonmori, H. Sasabe, and J. Kido, "Highly efficient organic blue-and white-light-emitting devices having a carrier-And exciton-confining structure for reduced efficiency roll-off," *Advanced Materials*, vol. 20, no. 21, pp. 4189–4194, 2008.
- [3] T. H. Han, Y. Lee, M. R. Choi et al., "Extremely efficient flexible organic light-emitting diodes with modified graphene anode," *Nature Photonics*, vol. 6, no. 2, pp. 105–110, 2012.
- [4] C. C. Hwang, "Plane source and in-line deposition system for OLED manufacturing," in *Proceedings of the 44th International Symposium, Seminar, and Exhibition (SID '06)*, pp. 1542–1545, June 2006, Technical Papers 37.
- [5] H. W. Kim, S. Y. Han, H. B. Shim et al., "Improvement of material utilization of organic evaporation source for manufacturing large-sized AMOLED devices," in *Proceedings of the International Symposium, Seminar, and Exhibition (SID '08)*, pp. 1450–1453, May 2008, Technical Papers 39.
- [6] G. A. Bird, *Molecular Gas Dynamics and the Direct Simulation of Gas Flows*, Clarendon Press, Oxford, UK, 1994.
- [7] D. M. Mattox, *Handbook of Physical Vapor Deposition (PVD) Processing*, Noyes, Westwood, NJ, USA, 1998.
- [8] M. Baldo, M. Deutsch, P. Burrows et al., "Organic vapor phase deposition," *Advanced Materials*, vol. 10, no. 18, pp. 1505–1514, 1998.
- [9] H. Fukumoto, Y. Muramatsu, T. Yamamoto, J. Yamaguchi, K. Itaka, and H. Koinuma, "Combinatorial physical vapor deposition of π -conjugated organic thin film libraries," *Macromolecular Rapid Communications*, vol. 25, no. 1, pp. 196–203, 2004.
- [10] H. Usui, "Formation of polymer thin films and interface control by physical vapor deposition," in *Proceedings of the SPIE*, vol. 7404, August 2009.
- [11] S.-H. Lai, C.-C. Chen, C.-C. Wang, F.-C. Tung, S.-H. Chen, and Y.-S. Wang, "OLED deposition system using plane-source evaporation techniques," in *Proceedings of the 20th International Display Workshops (IDW '13)*, 2013.
- [12] J.-S. Wu and Y.-Y. Lian, "Parallel three-dimensional direct simulation Monte Carlo method and its applications," *Computers and Fluids*, vol. 32, no. 8, pp. 1133–1160, 2003.
- [13] J. S. Wu and K. C. Tseng, "Parallel DSMC method using dynamic domain decomposition," *International Journal For Numerical Methods in Engineering*, vol. 63, no. 1, pp. 37–76, 2005.
- [14] J.-S. Wu, K.-C. Tseng, and F.-Y. Wu, "Parallel three-dimensional DSMC method using mesh refinement and variable time-step scheme," *Computer Physics Communications*, vol. 162, no. 3, pp. 166–187, 2004.
- [15] C.-C. Su, K.-C. Tseng, H. M. Cave et al., "Implementation of a transient adaptive sub-cell module for the parallel DSMC code using unstructured grids," *Computers & Fluids*, vol. 39, no. 7, pp. 1136–1145, 2010.
- [16] J. H. Jou, Y. S. Chiu, C. P. Wang, R. Y. Wang, and H.-C. Hu, "Efficient, color-stable fluorescent white organic light-emitting diodes with single emission layer by vapor deposition from solvent premixed deposition source," *Applied Physics Letters*, vol. 88, no. 19, Article ID 193501, 2006.
- [17] Y. C. Tsai and J. H. Jou, "Long-lifetime, high-efficiency white organic light-emitting diodes with mixed host composing double emission layers," *Applied Physics Letters*, vol. 89, no. 24, Article ID 243521, 2006.
- [18] J.-H. Jou, C.-Y. Hsieh, P.-W. Chen, S. Kumar, and J. H. Hong, "Candlelight style organic light-emitting diode: a plausibly human-friendly safe night light," *Journal of Photonics for Energy*, vol. 4, no. 1, Article ID 043598, 2014.
- [19] J. H. Jou, C. P. Wang, M. H. Wu et al., "Efficient fluorescent white organic light-emitting diodes with blue-green host of di(4-fluorophenyl)amino-di(styryl)biphenyl," *Organic Electronics: Physics, Materials, Applications*, vol. 8, no. 1, pp. 29–36, 2007.

Research Article

Organic Light-Emitting Diode with Color Tunable between Bluish-White Daylight and Orange-White Dusk Hue

Shih-Yun Liao, Sudhir Kumar, Hui-Huan Yu, Chih-Chia An, Ya-Chi Wang, Jhong-Wei Lin, Yung-Lee Wang, Yung-Chun Liu, Chun-Long Wu, and Jwo-Huei Jou

Department of Materials Science and Engineering, National Tsing Hua University, Hsin-Chu 30013, Taiwan

Correspondence should be addressed to Jwo-Huei Jou; jjou@mx.nthu.edu.tw

Received 14 March 2014; Accepted 19 May 2014; Published 5 June 2014

Academic Editor: Ramunas Lygaitis

Copyright © 2014 Shih-Yun Liao et al. This is an open access article distributed under the Creative Commons Attribution License, which permits unrestricted use, distribution, and reproduction in any medium, provided the original work is properly cited.

The varying color of sunlight diurnally exhibits an important effect on circadian rhythm of living organisms. The bluish-white daylight that is suitable for work shows a color temperature as high as 9,000 K, while the homey orange-white dusk hue is as low as 2,000 K. We demonstrate in this report the feasibility of using organic light-emitting diode (OLED) technology to fabricate sunlight-style illumination with a very wide color temperature range. The color temperature can be tuned from 2,300 K to 9,300 K, for example, by changing the applied voltage from 3 to 11 V for the device composing red and yellow emitters in the first emissive layer and blue emitter in the second. Unlike the prior arts, the color-temperature span can be made much wider without any additional carrier modulation layer, which should enable a more cost effective fabrication. For example, the color-temperature span is 7,000 K for the above case, while it is 1,700 K upon the incorporation of a nanoscale hole modulation layer in between the two emissive layers. The reason why the present device can effectively regulate the shifting of recombination zone is because the first emissive layer itself possesses an effective hole modulation barrier of 0.2 eV. This also explains why the incorporation of an extra hole modulation layer with a 0.7 eV barrier did not help extend the desirable color-temperature span since excessive holes may be blocked.

1. Introduction

Color temperature of light plays a crucial role on human physiology and psychology [1–9]. Bright daylight or high color temperature intensive artificial light, such as cold fluorescent tubes or the latest white LED lamps, stimulates the secretion of cortisol, a hormone that keeps people awake and active [1–3]. Numerous medical studies revealed that frequent exposure to high color temperature light also markedly suppresses the nocturnal secretion of oncostatic melatonin, increasing the risk of breast, colorectal, and prostate cancers [4–7].

Moreover, current lighting sources provide only a fixed color temperature, seriously mismatching what one truly needs from the standpoint of circadian rhythm; that is, circadian rhythm can be entrained by bright light with high color temperature and melatonin generation can be triggered at dark night. Devising a light source with color temperature tunability would hence be highly valuable. However, little

attention had been paid to this until 2009. The first sunlight-style color temperature tunable OLED was reported in 2009, which yielded a wide color-temperature span, fully covering that of the entire daylight locus [10]. However, the corresponding power efficiency was low because of the use of purely fluorescent emitters. Although the efficiency has been much improved as electroluminescence effective phosphorescent emitters were employed, the color rendering index was low [11]. To provide visual comfort, high or very-high color rendering index is required, which can be realized by employing an effective carrier modulation layer (CML) [12]. A high triplet energy CML may effectively regulate the entering carriers into the available wider recombination zones and results in a wide color-temperature span with desirable electroluminescence spectrum [13, 14]. In past decade, several researchers have reported the chromaticity tunable OLEDs using various types of carrier modulation layers. For example, in 2002, Forrest's group has reported that the CIE color coordinates of the OLED emission can be tuned over a

wide range by inserting a 5 nm exciton blocking layer, BCP, between the emissive layers [15]. Chen et al. have reported the emission color of hybrid white OLED can also be tuned by changing the bipolar CML, CBP, thickness from 2 to 8 nm [16]. Recently, our group had also demonstrated the feasibility of using OLED lighting technology to fabricate light sources with low color temperature as well as chromaticity tunable between that of dusk hue and candle-light [17, 18]. The challenge has now become how to design and fabricate a cost effective lighting device with a high color rendering index along with a color temperature tunable character, and daylight chromaticity is essential, especially considering its strong effect on human physiology and psychology [19–22].

We demonstrate, in this report, the feasibility of using OLED technology to fabricate sunlight-style illumination with a very wide color temperature range and high color rendering index (up to 84), without employing a CML. The resulting color temperature is tunable from 2,300 K to 9,300 K, covering that of entire daylight chromaticities. The CIE coordinates of device, composing orange and yellow emitters in the first emissive layer and blue emitter in the second, can simply tune from (0.51, 0.40) to (0.27, 0.31) by changing the applied voltage from 3 to 11 V. The wide color-temperature range may be attributed to the fact that the recombination zone therein can easily be shifted along the different emissive zones from the first to the second layer via voltage control is because the first emissive layer itself possesses an effective hole modulation function for having a 0.2 eV hole injection barrier between the hole transporting layer and the host.

2. Experimental

2.1. Device Fabrication. Figure 1(a) shows the device architectures of the studied sunlight-style OLED devices without any CML. We fabricated the color temperature tunable OLED devices by using three blackbody radiation complementary emitters, that is, a red light-emitting iridium complex with heterocyclic ligand (WPRD931, a proprietary material from Wan Hsiang OLED Ltd.), a yellow light-emitting dye, 5,6,11,12-tetra-phenylnaphthacene (rubrene), and a blue light-emitting dye, EB515 (a proprietary blue light-emitting material from e-Ray Optoelectronics Technology Co. Ltd.), dispersed in two different emissive layers (EMLs). As shown in Figure 1, the first EML (12 nm) for yielding an orange emission was obtained by doping 2 to 4 wt% rubrene and 0.3 to 0.5 wt% of the red dye of WPRD931 in mixed hosts of bis(2-methyl-8-quinolinolato)(4-phenylphenolato)aluminum (BALq) and *N,N'*-Di(1-naphthyl)-*N,N'*-diphenyl-(1,1'-biphenyl)-4,4'-diamine (NPB) with a ratio of 4 : 1, and the second EML (28 nm) was designated to yield a blue emission, which was obtained by doping 10 to 15 wt% EB515 in a host of aryl substituted anthracene derivative (EB43, a proprietary blue light-emitting host from e-Ray Optoelectronics Technology Co. Ltd.). The devices comprised of 5 nm 1,4,5,8,9,11-hexaazatriphenylene-hexanitride (HAT-CN) carrier generation layer (CGL), a 36 nm di-[4-(*N,N*-ditolyl-amino)-phenyl]cyclohexane (TAPC) hole transporting layer (HTL), a 32 nm BmPyPb electron transporting layer (ETL), a 1 nm

lithium fluoride (LiF) electron injection layer, and a 150 nm aluminum cathode layer. All fabricated devices, except Device II-1 and Device II-2, have an additional carrier modulating layer, 1,3,5-trisN-phenylbenzimidazol-2-ylbenzene (TPBi), in between the orange and blue EMLs.

2.2. Characterization. The current-voltage-luminance (*I-V-L*) characteristics of the resulting phosphorescent yellow OLEDs were measured using a Keithley 2400 electrometer together with a Minolta CS-100 luminance meter. Electroluminescence (EL) spectrum and CIE color coordinates were obtained by using a PR655 SpectraScan spectroradiometer. The emission area of all the resultant devices was 9 mm² and only the luminance in the forward direction was measured.

3. Result and Discussion

The OLEDs with a sunlight-style chromaticity were obtained by employing three sunlight chromaticity complementary emitters via device engineering to adjust the relative emissive intensity of the two EMLs so that the resultant emission would fall at or nearby the daylight locus. The three emitters employed had indeed enabled the generation of the desirable sunlight-style chromaticity with a color temperature ranging at least from 2,300 K to 9,300 K. In the present device system, the relative emissive intensity of the two EMLs was achieved simply by adjusting the doping concentration of the yellow emitter in the first EML and the blue emitter in the second EML.

Table 1 summarizes the effect of emitters doping concentration and CML thickness on the resultant color-temperature span. Without the use of CML (Device I-1), the device with a 2 wt% yellow dopant and a 0.3 wt% red dopant in the first EML and 10 wt% blue dopant in the second EML exhibited a color temperature ranging between 2,460 K and 9,340 K. By increasing the red dopant from 0.3 to 0.5 wt% (Device I-2), the orange red emission became dominant, relatively, with a color temperature varying between 2,170 K and 8,990 K. Whilst by increasing the yellow-dopant from 2 to 4 wt% and blue dopant from 10 to 15 wt% (Device I-3), the entire emission slightly shifted toward the bluer side, and color temperature covered the entire day-light locus. This indicates the dopant concentration has played a significant role in obtaining the broader color-temperature span. As a 3 nm CML was inserted in between the orange red and blue EMLs (Device II-1), the blue emission became dominant with a color temperature varying between 2,900 K and 4,890 K.

Notably, the corresponding color-temperature span became markedly smaller, however, as the thickness of the CML was increased to 5 nm (Device II-2). The comparatively weaker blue emission and stronger orange-red emission had resulted in a much lower color temperature along with the smaller color-temperature span of 1,700 K. Apparently, the thicker modulation layer had blocked excessive holes from entering the blue-emissive zone, leading to a blue-less emission. In contrast, more holes would hence be retained in the orange red emissive zone.

With the above-mentioned device architecture, the sunlight-style OLED, Device I-3, exhibited an emission track

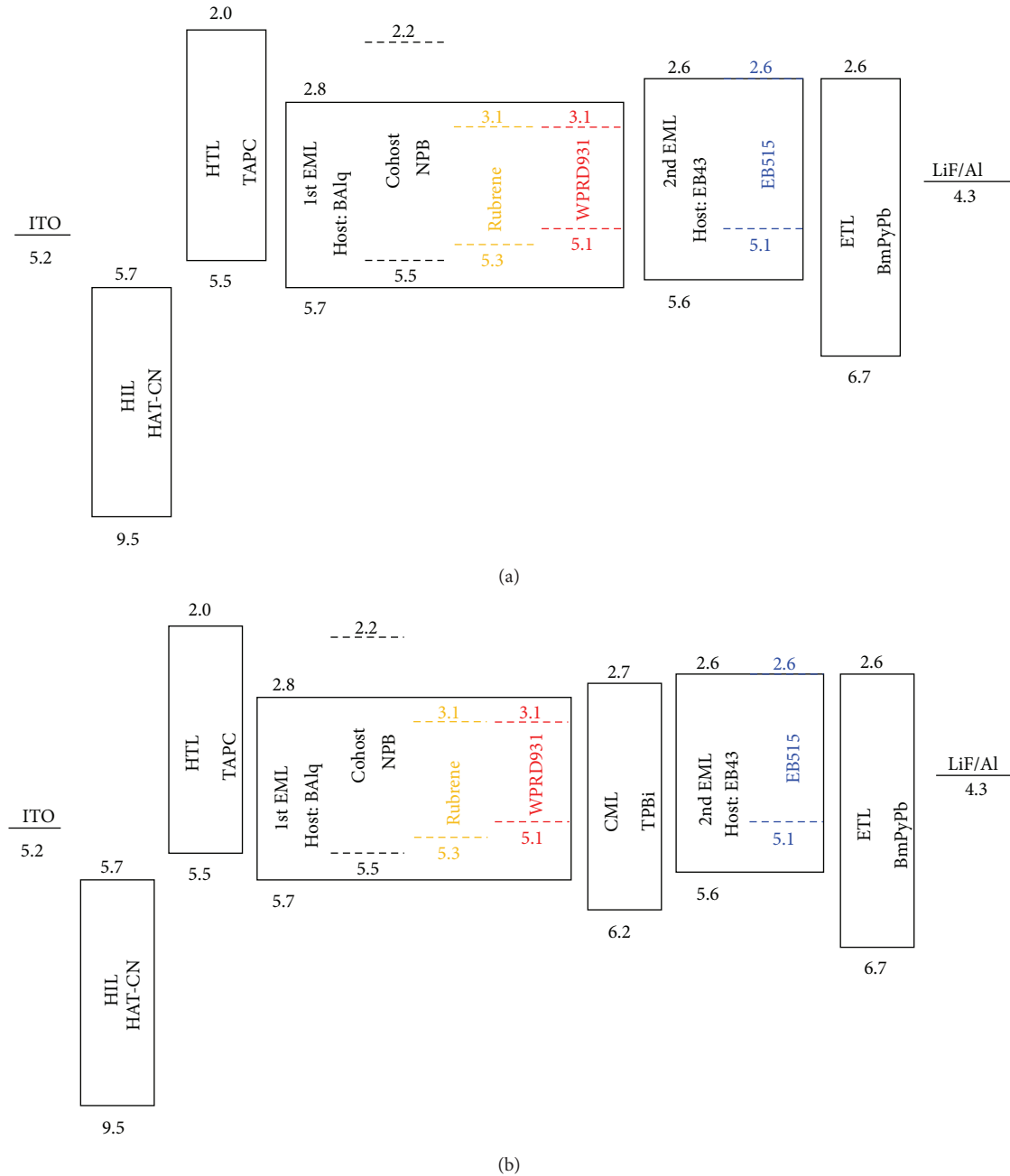


FIGURE 1: Schematic illustrations of the device structure, in terms of energy-levels, of the color temperature tunable OLED devices composing three black body radiation complementary emitters, namely, red, yellow, and blue, dispersed in two emissive layers (EMLs) (a) without any hole modulation layer, and (b) with an extra nanoscale hole modulating layer with an energy barrier of 0.7 eV at the interface between the orange and blue EMLs. Nevertheless, there still exists a 0.2 eV hole injection barrier in Device (a) between the hole transporting layer and the host of the first EML, which could hence effectively regulate the injection of hole and in turn the shifting of recombination zone.

closely matching with the day-light locus shown on the CIE chromaticity diagram in Figure 2. Besides having a wide color-temperature span ranging from 2,300 K to 9,300 K, it also emitted a significantly high color rendering index, ranging from 74 to 84.4 for voltage increasing from 3.0 to 11.5 V (Figure 3).

As shown by the electroluminescent spectra in Figure 4, the device initially showed a predominantly orange-red emission spectrum at 4.0 V with CIE coordinates of (0.45,

0.39), turning to pure white (0.33, 0.34) at 7.0 V, and bluish white (0.29, 0.32) at 9.5 V. Relative to the blue emission, the rapidly decreasing peak intensity of the green and yellow emissions with respect to the applied voltage explains why the emission is hypsochromically shifted as the operation voltage increased from 6.0 to 9.5 V. The reason why the sunlight-style OLED, Device I-3, could effectively regulate the shifting of recombination zone is because the first emissive layer itself possesses an effective hole modulation barrier of

TABLE 1: Effects of dopant concentration and carrier modulating layer thickness on the color temperature span, color temperature, and color rendering index of the sunlight-style OLED devices studied.

Device	Dopant concentration [wt%]		CML thickness (nm)	CT span (K)	CT (K)	CRI	Power efficiency (lm/W)	Current efficiency (cd/A) @100/1,000 cd/m ²	1931 CIE coordinates	Operating voltage (V)	Maximum luminance (cd/m ²)
	Ist EML Yellow	Blue									
I-1	2	0.3	—	2,460–9,340	2,980/4,530	84.3/80.8	4.0/2.7	5.7/5.4	(0.42, 0.38)/(0.35, 0.35)	4.5/6.1	10,800
I-2	2	0.5	—	2,170–8,990	2,940/4,410	85.2/82.1	4.0/2.4	5.7/4.7	(0.43, 0.38)/(0.36, 0.35)	4.5/6.2	10,270
I-3	4	0.5	—	2,290–9,280	2,980/4,540	80.7/84.4	3.9/3.1	5.7/6.0	(0.42, 0.38)/(0.35, 0.35)	4.6/6.2	10,160
II-1	2	0.3	3	2,900–4,890	3,060/3,870	83.6/84.5	4.3/2.9	5.9/6.0	(0.42, 0.38)/(0.38, 0.37)	4.3/6.4	4,990
II-2	2	0.3	5	2,570–4,270	2,860/3,380	80.1/82.0	4.5/2.7	6.3/5.7	(0.44, 0.39)/(0.41, 0.38)	4.5/6.6	4,750

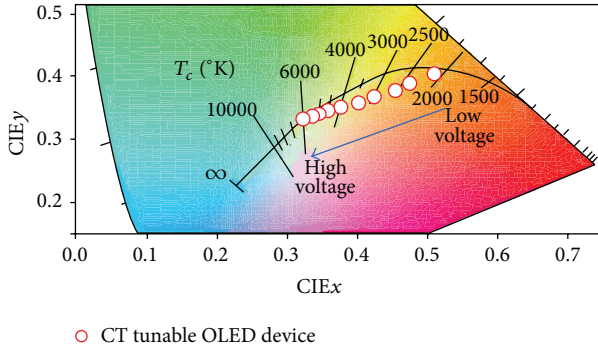


FIGURE 2: Chromaticity and color temperature characteristics of the color temperature tunable OLED, which shows a dusk hue-style emission at low applied voltage and bluish white light-style emission at high voltage. A record high color-temperature span is observed for the device without using any additional CML.

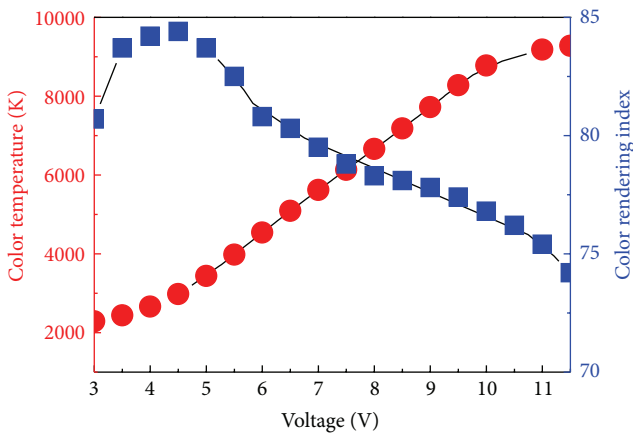


FIGURE 3: For the studied sunlight-style OLED (Device-I-3), its color temperature changes from 2,290 to 9,280 K and color rendering index from 74 to 84.4 as the applied voltage is increased from 3 to 11.5 V.

0.2 eV. As the operation voltage was increased, increasing electrons could transport to the blue emissive zone and in turn it resulted in a higher probability of recombination therein, leading to a bluer emission as observed. This also explains why the incorporation of an extra CML with a 0.7 eV barrier did not help extend the desirable color-temperature span since excessive holes would have been blocked, and the blocking effect had increased markedly as the CML thickness was increased from 3 to 5 nm.

Figure 5 shows the resultant power efficiency of the studied OLED devices. For the desirable sunlight-style OLED, Device I-3, its respective power efficiency was 3.9 and 3.1 lm/W, and current efficiency 5.7 and 6.0 cd/A, at 100 cd/m² and 1,000 cd/m², respectively.

4. Conclusion

To conclude, we demonstrate in this study a CML free, sunlight-style OLED with color tunable between bluish white

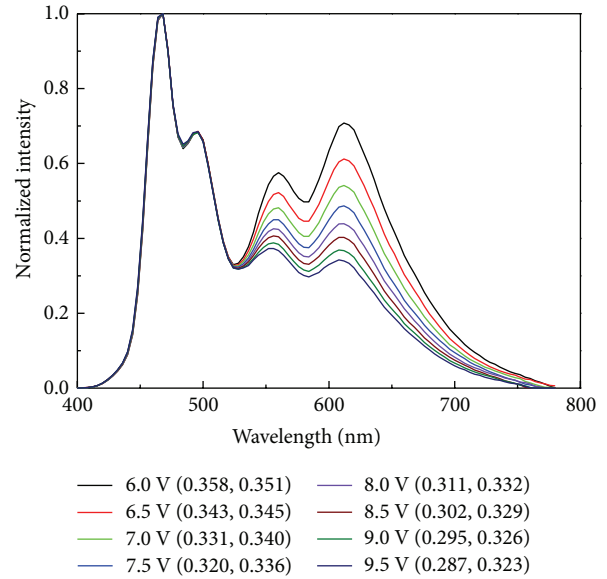


FIGURE 4: Electroluminescence spectra of the sunlight-style OLED (Device I-3) at various applied voltages.

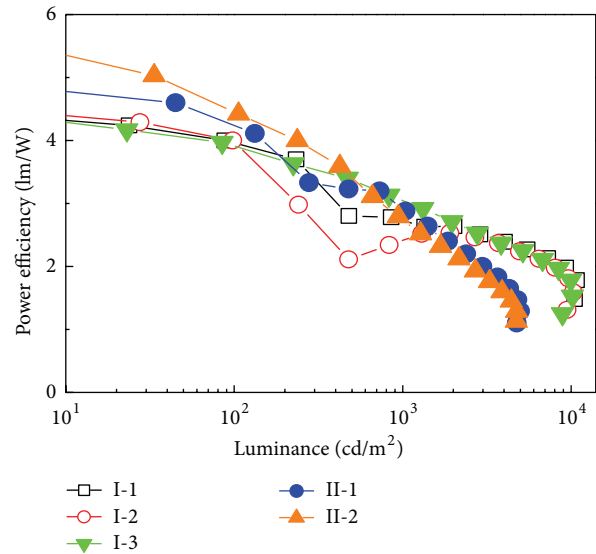


FIGURE 5: The resultant power efficiency of the sunlight-style OLED devices studied. For Device I-3 with the desirable color-temperature span and sunlight-style chromaticity, its power efficiency varied from 4.2 to 1.8 lm/W at luminance increasing from 10 to 10,160 cd/m².

daylight and warm dusk hue with a record high color-temperature span of 7,000 K, along with a color rendering index varying from 74 to 84.4. The reason why the device could effectively regulate the shifting of the recombination zone is because the first emissive layer itself possesses an effective hole modulation barrier of 0.2 eV. Unlike the prior arts, the color-temperature span can be made much wider without any additional CML, which should enable a more cost effective fabrication.

Conflict of Interests

The authors declare that there is no conflict of interests regarding the publication of this paper.

Acknowledgments

The authors are cordially thankful to National Science Council (NSC) and Ministry of Economic Affairs (MEA) for their financial support in part under the following Grants MEA102-EC-17-A-07-S1-181, NSC102-3113-E-007-001, and NSC100-2119-M-007-011-MY3.

References

- [1] P. R. Mills, S. C. Tomkins, and L. J. M. Schlangen, "The effect of high correlated colour temperature office lighting on employee wellbeing and work performance," *Journal of Circadian Rhythms*, vol. 5, article 2, 2007.
- [2] F. A. J. L. Scheer, L. J. P. van Doornen, and R. M. Buijs, "Light and diurnal cycle affect human heart rate: possible role for the circadian pacemaker," *Journal of Biological Rhythms*, vol. 14, no. 3, pp. 202–212, 1999.
- [3] W. J. M. van Bommel, "Non-visual biological effect of lighting and the practical meaning for lighting for work," *Applied Ergonomics*, vol. 37, no. 4, pp. 461–466, 2006.
- [4] G. C. Brainard, B. A. Richardson, T. S. King, and R. J. Reiter, "The influence of different light spectra on the suppression of pineal melatonin content in the syrian hamster," *Brain Research*, vol. 294, no. 2, pp. 333–339, 1984.
- [5] S. W. Lockley, G. C. Brainard, and C. A. Czeisler, "High sensitivity of the human circadian melatonin rhythm to resetting by short wavelength light," *Journal of Clinical Endocrinology and Metabolism*, vol. 88, no. 9, pp. 4502–4505, 2003.
- [6] S. M. Pauley, "Lighting for the human circadian clock: recent research indicates that lighting has become a public health issue," *Medical Hypotheses*, vol. 63, no. 4, pp. 588–596, 2004.
- [7] T. Hättönen, A. Alila-Johansson, S. Mustanoja, and M.-L. Laakso, "Suppression of melatonin by 2000-lux light in humans with closed eyelids," *Biological Psychiatry*, vol. 46, no. 6, pp. 827–831, 1999.
- [8] M. Sato, T. Sakaguchi, and T. Morita, "The effects of exposure in the morning to light of different color temperatures on the behavior of core temperature and melatonin secretion in humans," *Biological Rhythm Research*, vol. 36, no. 4, pp. 287–292, 2005.
- [9] R. Kuller and L. Wetterberg, "Melatonin, cortisol, EEG, ECG, and subjective comfort in healthy humans: impact of two fluorescent lamp types at two light intensities," *Lighting Research & Technology*, vol. 25, no. 2, pp. 71–80, 1993.
- [10] J.-H. Jou, M.-H. Wu, S.-M. Shen et al., "Sunlight-style color-temperature tunable organic light-emitting diode," *Applied Physics Letters*, vol. 95, no. 1, Article ID 013307, 2009.
- [11] J. H. Jou, S. M. Shen, M. H. Wu, S. H. Peng, and H. C. Wang, "Sunlight-style organic light-emitting diodes," *Journal of Photonics for Energy*, vol. 1, no. 1, Article ID 011021, 2011.
- [12] J.-H. Jou, Y.-C. Chou, S.-M. Shen et al., "High-efficiency, very-high color rendering white organic light-emitting diode with a high triplet interlayer," *Journal of Materials Chemistry*, vol. 21, no. 46, pp. 18523–18526, 2011.
- [13] J.-H. Jou, S.-H. Chen, S.-M. Shen et al., "High efficiency low color-temperature organic light-emitting diodes with a blend interlayer," *Journal of Materials Chemistry*, vol. 21, no. 44, pp. 17850–17854, 2011.
- [14] J.-H. Jou, H.-C. Wang, S.-M. Shen et al., "Highly efficient color-temperature tunable organic light-emitting diodes," *Journal of Materials Chemistry*, vol. 22, no. 16, pp. 8117–8120, 2012.
- [15] W. D'Andrade, M. E. Thompson, and S. R. Forrest, "Controlling exciton diffusion in multilayer white phosphorescent organic light emitting devices," *Advanced Materials*, vol. 14, no. 2, pp. 147–151, 2002.
- [16] P. Chen, W. Xie, J. Li et al., "White organic light-emitting devices with a bipolar transport layer between blue fluorescent and orange phosphorescent emitting layers," *Applied Physics Letters*, vol. 91, no. 2, Article ID 023505, 2007.
- [17] J.-H. Jou, P.-W. Chen, Y.-L. Chen et al., "OLEDs with chromaticity tunable between dusk-hue and candle-light," *Organic Electronics*, vol. 14, no. 1, pp. 47–54, 2013.
- [18] J.-H. Jou, C.-Y. Hsieh, J.-R. Tseng et al., "Candle light-style organic light-emitting diodes," *Advanced Functional Materials*, vol. 23, no. 21, pp. 2750–2757, 2013.
- [19] G. Lambert, C. Reid, D. Kaye, G. Jennings, and M. Esler, "Increased suicide rate in the middle-aged and its association with hours of sunlight," *American Journal of Psychiatry*, vol. 160, no. 4, pp. 793–795, 2003.
- [20] I. Knez, "Effects of colour of light on nonvisual psychological processes," *Journal of Environmental Psychology*, vol. 21, no. 2, pp. 201–208, 2001.
- [21] T. Dalglish, K. Rosen, and M. Marks, "Rhythm and blues: the theory and treatment of seasonal affective disorder," *British Journal of Clinical Psychology*, vol. 35, no. 2, pp. 163–182, 1996.
- [22] R. W. Lam, D. F. Kripke, and J. C. Gillin, "Phototherapy for depressive disorders: a review," *Canadian Journal of Psychiatry*, vol. 34, no. 2, pp. 140–147, 1989.

Research Article

Improvement in Device Performance and Reliability of Organic Light-Emitting Diodes through Deposition Rate Control

Shun-Wei Liu,¹ Chih-Chien Lee,² Yu-Ting Chung,² Jiun-Haw Lee,³
Chin-Ti Chen,⁴ and Juen-Kai Wang^{5,6}

¹ Department of Electronic Engineering, Ming Chi University of Technology, New Taipei City 24301, Taiwan

² Department of Electronic Engineering, National Taiwan University of Science and Technology, Taipei 106, Taiwan

³ Graduate Institute of Photonics and Optoelectronics and Department of Electrical Engineering, National Taiwan University, Taipei 106, Taiwan

⁴ Institute of Chemistry, Academia Sinica, Taipei 11529, Taiwan

⁵ Center for Condensed Matter Sciences, National Taiwan University, Taipei 106, Taiwan

⁶ Institute of Atomic and Molecular Sciences, Academia Sinica, Taipei 106, Taiwan

Correspondence should be addressed to Jiun-Haw Lee; jiunhawlee@ntu.edu.tw and Chin-Ti Chen; cchen@chem.sinica.edu.tw

Received 25 February 2014; Revised 9 April 2014; Accepted 10 April 2014; Published 27 April 2014

Academic Editor: K. R. Justin Thomas

Copyright © 2014 Shun-Wei Liu et al. This is an open access article distributed under the Creative Commons Attribution License, which permits unrestricted use, distribution, and reproduction in any medium, provided the original work is properly cited.

We demonstrated a fabrication technique to reduce the driving voltage, increase the current efficiency, and extend the operating lifetime of an organic light-emitting diode (OLED) by simply controlling the deposition rate of bis(10-hydroxybenzo[h]quinolinato) beryllium (Bebq₂) used as the emitting layer and the electron-transport layer. In our optimized device, 55 nm of Beq₂ was first deposited at a faster deposition rate of 1.3 nm/s, followed by the deposition of a thin Beq₂ (5 nm) layer at a slower rate of 0.03 nm/s. The Beq₂ layer with the faster deposition rate exhibited higher photoluminescence efficiency and was suitable for use in light emission. The thin Beq₂ layer with the slower deposition rate was used to modify the interface between the Beq₂ and cathode and hence improve the injection efficiency and lower the driving voltage. The operating lifetime of such a two-step deposition OLED was 1.92 and 4.6 times longer than that of devices with a single deposition rate, that is, 1.3 and 0.03 nm/s cases, respectively.

1. Introduction

Molecular packing plays an important role in the function of organic electronics and optoelectronic devices [1–5]. For organic thin-film transistor (OTFT) applications, appropriate packing produces higher field-effect mobility resulting in increased electrical current [1]. Molecular packing of organic materials for OTFT (such as pentacene) can be adjusted by introducing the substituent to the molecules, surface treatment (e.g., octadecyltrichlorosilane), or insertion of self-assembled monolayer [6, 7]. For polymer solar cell application, molecular packing can be controlled by fabrication techniques such as thermal annealing or solvent annealing. Better molecular packing of donor material (e.g., poly(3-hexylthiophene)) not only improved hole mobility and charge balance but also increased absorption [8, 9]. For

the small-molecular organic solar cell, molecular packing plays an important role in determining the open circuit voltage (V_{OC}). For organic materials with higher crystallinity, it resulted in higher saturation dark current, and in turn reduced the V_{OC} and hence power conversion efficiency, which can be engineered by inserting an interfacial layer or varying evaporation rate [10, 11]. For the organic light-emitting diode (OLED) application, we demonstrated in our previous study that molecular packing of a planar molecule, bis(10-hydroxybenzo[h]quinolinato) beryllium (Bebq₂), can be controlled via the deposition rate during vacuum sublimation [12–14]. Atomic force microscopy (AFM) measurements confirmed that a slower deposition rate (i.e., 0.03 nm/s) resulted in better molecular packing. When slower-deposition rate Beq₂ was used as the emitting layer (EML) and the electron-transporting layer (ETL) material

in our OLED, such an ordered molecular packing improved electron mobility and reduced driving voltage. On the other hand, the ordered BeBq₂ resulted in a photoluminescence (PL) quenching and a lower current efficiency (in terms of cd/A), so there appeared to be a tradeoff between the electrical and optical properties.

The deposition rate of organic materials was generally controlled at ~ 0.1 nm/s, with some fluctuations (e.g., 0.08–0.12 nm/s). An ultralow deposition rate (e.g., less than 0.01 nm/s) meant that device fabrication took a long time and was impractical from a manufacturing point of view. On the other hand, at ultrahigh deposition rates (e.g., higher than 10 nm/s) precise control over the thickness of the organic layer became problematic. This paper therefore looks at deposition rates between 0.03 and 1.3 nm/s due to practical considerations such as takt time and precise thickness control. During the evaporation process, temperature was carefully adjusted to achieve constant deposition rates of 0.03, 0.3, and 1.3 nm/s with fluctuations of 0.02–0.04, 0.27–0.33, and 1.1–1.4 nm/s, respectively. The separation of deposition rates was sufficient to avoid any possible overlap due to fluctuation in deposition rate.

In this report, we made use of a two-step evaporation technique for depositing BeBq₂ at high and low rates sequentially. First, 55 nm of BeBq₂ was deposited at a fast rate (1.3 nm/s) to form the EML (and ETL as well) alleviating the PL quenching at the recombination zone near the HTL/EML interface. This was followed by the deposition of a BeBq₂ thin layer (5 nm) at a slow rate (0.03 nm/s) to modify the interface between the ETL and the cathode for efficient electron injection, which was deduced from electron-only device and AFM measurement. Although BeBq₂ with slower deposition rate exhibited the lowest PL efficiency, it did not affect the device performances because it was far away from the recombination zone.

2. Experiment

To study the effects of the deposition rate on the device performance and lifetime of the electroluminescence (EL) device, five different device structures were fabricated, as summarized in Table 1. The authors selected ITO/NPB (60 nm)/BeBq₂, (55 nm)/BeBq₂, (5 nm)/LiF, and (1 nm)/Al (100 nm) as the EL samples, in which the 5 nm thick BeBq₂ layer was deposited at three different rates of 0.03 nm/s (device A), 0.3 nm/s (device B), and 1.3 nm/s (device C). OLEDs with different single deposition rates (0.3 and 0.03 nm/s) were also fabricated and designated as devices D and E, respectively. The fabrication process was similar to that outlined in our previous reports, except for the purification process of the organic materials [15]. For this experiment, the organic materials were purified three times by temperature-gradient sublimation. This change indeed resulted in significant changes to the lifetime performances compared to our previous studies [14]. Despite similar device configurations and aging conditions, the operating lifetimes observed in this project were approximately 10 times longer than those in our previous paper [14]. We

TABLE 1: (a) Five different device structures used to investigate the dependence of device performance on deposition rate of ultrathin ETL. Consider $(x, y) = (1.3, 0.03), (1.3, 0.3), (1.3, 1.3), (0.3, 0.3),$ and $(0.03, 0.03)$ for devices A, B, C, D, and E, respectively. (b) Three different device structures used to investigate the electron injection characteristics on deposition rate of ultrathin ETL. Consider $z = 0.03, 0.3,$ and 1.3 for devices F, G, and H, respectively.

(a)
LiF/Al, 1/100 nm
BeBq ₂ , 5 nm, y nm/s
BeBq ₂ , 55 nm, x nm/s
NPB, 60 nm
ITO, 80 nm
Glass
(b)
Ca, 150 nm
BeBq ₂ , 5 nm, z nm/s
BeBq ₂ , 55 nm, 1.3 nm/s
Ca, 150 nm
Glass

also measured the J - V characteristics of the single carrier (electron) device to investigate the injection characteristics of the organic/electrode interface [16]. The device structures were Ca (150 nm; 0.1 nm/s)/BeBq₂, (55 nm; 1.3 nm/s)/BeBq₂, (5 nm; 0.03, 0.3 and 1.3 nm/s)/Ca, and (150 nm; 0.1 nm/s) on glass substrate, designated as devices F, G, and H, respectively. For our fabrication, the ITO/glass substrate (sheet resistance $\sim 30 \Omega/\square$) was commercially obtained from the Merck Corporation, with the low energy method (AC2; Riken Keiki) yielding a work function of 4.8 eV for the ITO. During the film deposition of the devices, the pressure of the chamber was maintained at below 4×10^{-6} torr. The thickness of each organic layer was calibrated by a surface profiler (Dektak 150; Veeco) before device fabrication. The active area of the devices was 4 mm^2 and the devices were completed with an encapsulation in a glove box (O_2 and H_2O concentration below 0.1 ppm). A DC current/voltage source meter (2400; Keithley) was used to measure current density versus voltage characteristics, while the brightness was monitored with a spectrophotometer (PR650; Photo Research). The device lifetime was determined with a constant current density of 100 mA/cm^2 in a DC driving condition. For AFM measurement (noncontact mode; Park system XE-100), the Si wafer was sequentially sonicated in acetone, methanol, and deionized water, and etched in dilute H_2SO_4 solution. Immediately after cleaning, the substrates were transferred into an evaporation chamber for deposition of the organic thin film. The surface roughness of the cleaned Si wafer was 0.2 nm.

3. Results and Discussion

3.1. Device Performances. Figure 1 shows the J - V characteristics and EL efficiency of devices A–E. The only difference

in the OLED fabrication process among devices A, B, and C was the deposition rate of the ultrathin Bebq_2 at the LiF/Al interface, with these being 0.03, 0.3, and 1.3 nm/s, respectively, while the deposition rate of the thick Bebq_2 at the HTL interface was maintained at 1.3 nm/s. One should note that the current density decreased monotonically from 25.8 to 11 mA/cm^2 at 6 V when the deposition rate of the final Bebq_2 layer was increased from 0.03 to 1.3 nm/s. When devices C, D, and E were compared with cases where the entire Bebq_2 layer was deposited at a constant evaporation rate of 1.3, 0.3, and 0.03 nm/s, respectively, current density increased monotonically as the deposition rate decreased, because lower evaporation rates resulted in higher electron mobility [17]. By comparing the J - V characteristics of devices A, B, and C, we can see that the ultrathin Bebq_2 film (5 nm) near the LiF/Al interface helped to reduce the driving voltage; that is, this thin layer may facilitate better electron injection from the cathode into the ETL and EML. To confirm this hypothesis, three electron-only devices with the device structure shown in Table I were fabricated. A thick Bebq_2 (55 nm; 1.3 nm/s) layer followed by a thin Bebq_2 (5 nm) layer deposited at rates of 0.03, 0.3, and 1.3 nm/s, respectively, was sandwiched between two Ca electrodes. Figure 2 shows the J - V characteristics of the electron-only devices. As expected, the electron-only device with a thin Bebq_2 (5 nm) layer of the lowest deposition rate (0.03 nm/s) exhibited the highest current density due to better electron injection capability, consistent with the device performances observed in Figure 1(a). By optimizing the carrier injection and carrier transport, one can theoretically obtain an OLED with the lowest driving voltage (device E). For the cases with a single deposition rate (1.3, 0.3, and 0.03 nm/s, corresponding to devices C, D, and E, resp.), one can note that the current efficiency decreased with the deposition rate, as shown in Figure 1(b), due to the decrease in PL efficiency with better molecular packing at a lower deposition rate [14]. By changing the deposition rate of the thin (5 nm) Bebq_2 layer close to LiF/Al (devices A, B, and C), the current efficiency decreased monotonically from 7.5 to 5.4 cd/A at 100 mA/cm^2 when the deposition rate of the final Bebq_2 layer was increased from 0.03 to 1.3 nm/s. The change can be attributed to better electron injection at the cathode interface and hence better electron/hole balance [18–20]. By simply decreasing the evaporation rate at the ETL and LiF/Al interface, device performances were significantly improved with lower driving voltages and higher current efficiencies.

3.2. Accelerated Lifetime Test. To evaluate the effects of the Bebq_2 /electrode on the device lifetime, the five types of Bebq_2 based devices (A–E) were measured at a constant DC driven current density of 100 mA/cm^2 . Figures 3(a) and 3(b) show the time dependent variations of the device luminance and driving voltage. The initial luminance was 7470, 7300, 5320, 3360, and 3220 cd/m^2 for devices A, B, C, D, and E, respectively. No detectable change in the EL spectra was observed for the five OLEDs during the accelerated lifetime test. This evidence suggested that there was no change in the chemical nature of these organic layers and no drastic alteration in the emission zone location during device operation; that is,

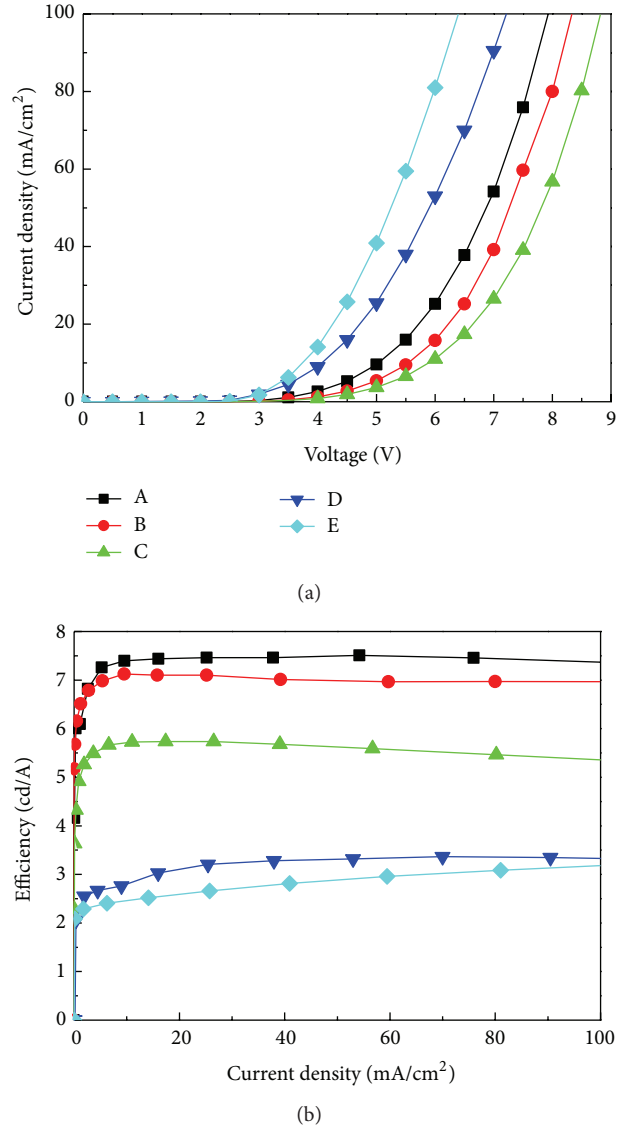


FIGURE 1: (a) Luminance versus bias voltage and (b) electroluminescence efficiency versus current density of devices A to E.

the EL efficiency degradation was most likely due to the decrease in the created exciton density and radiative efficiency. When the deposition rate for the last 5 nm Bebq_2 layer was decreased from 1.3 to 0.03 nm/s, the device exhibited a significantly longer lifetime compared to similar devices with no change in the deposition rate. The extracted half lifetimes of the OLEDs with a two-step deposition process (devices A and B) were 1200 and 833 min. at deposition rates of 0.03 and 0.3, respectively, for ultrathin Bebq_2 (5 nm) on the bulk material (55 nm). This suggested that modifying the organic/electrode interface at the electron contact of OLED can significantly improve their operational reliability. In contrast, the corresponding half lifetimes of bulk Bebq_2 devices with constant deposition rate were 410, 288, and 214 min. at deposition rates of 1.3, 0.3, and 0.03 nm/s, respectively. The extracted device lifetimes (devices C, D, and E)

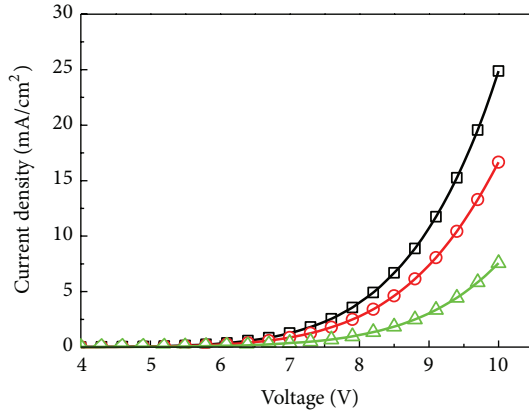


FIGURE 2: Current density versus bias voltage characteristics of electron-only devices with a BeBq_2 layer deposited at three deposition rates (solid line, 0.03 nm/s; dashed line, 0.3 nm/s; dotted line, 1.3 nm/s).

decreased as the film deposition rate decreased. The PL intensities were measured before and after the aging process, with decreases of 3.6%, 4%, 4.3%, 20%, and 35% observed for devices A, B, C, D, and E, respectively. One should note that the PL decrease was the most pronounced for device E. On the contrary, as shown in Figure 3(b), the voltage increase was highest for the OLED with the highest deposition rate (device C). By using a low deposition rate BeBq_2 at the LiF/Al interface, the voltage increase was significantly alleviated in devices A and B. The voltage increase in an aged OLED is due to the trap density formation [21–23]. By comparing devices C, D, and E, one may conclude that the lower deposition rates helped to reduce the trap formation. Device A exhibited the lowest voltage increase rate (even lower than device E), however, indicating that the trap distribution upon electrical aging was different under different deposition rates. For device C, with the highest deposition rate BeBq_2 , traps were formed near the interface in direct contact with the cathode. On the other hand, for device E, the traps were mainly located away from the cathode side. With the two-step evaporation process, the trap formation rate for the entire BeBq_2 layer was decreased, extending the operating lifetime. This explained the differences in the EL lifetimes among devices A, B, and C, despite similar PL decay rates.

3.3. Surface Morphology. To further investigate the possible physical mechanisms in play, we examined the correlation of the morphology of the BeBq_2 layer with other devices prepared on Si wafer [4]. Although the situation of BeBq_2 deposited on Si substrate may be different from that on ITO glass, unfortunately, the surface of ITO is quite rough making it unsuitable for studying the surface condition of BeBq_2 thin film. Figure 4 shows the AFM surface morphology measurement of the bulk BeBq_2 films from the two-step deposition process. Such layers were fabricated with a constant deposition rate of 1.3 nm/s (55 nm) for the bulk material, followed by deposition of the last 5 nm ultrathin layer at the three different deposition rates of 0.3, 0.03, and

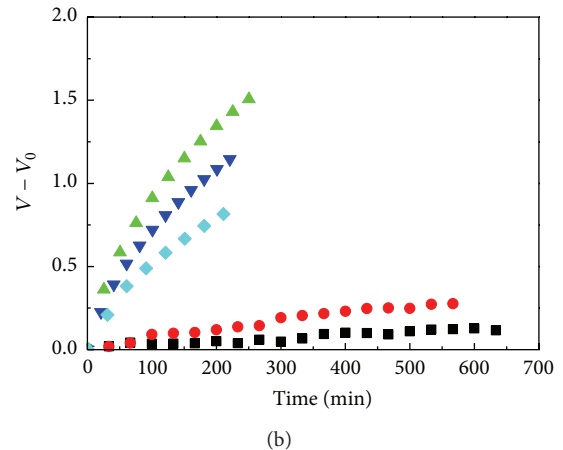
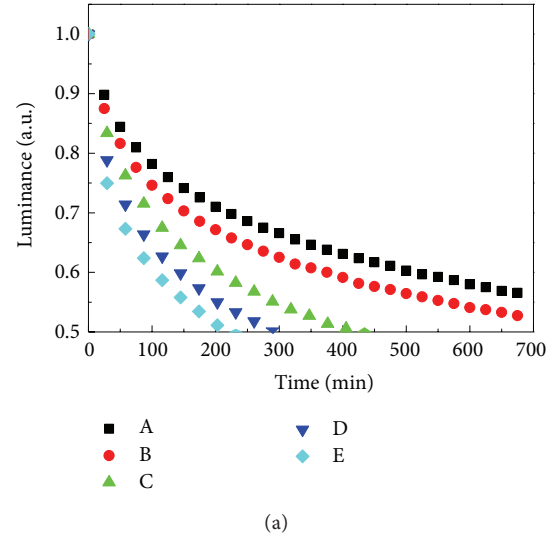


FIGURE 3: (a) Normalized luminance (L^*) and (b) voltage variation ($V - V_0$) versus operating time of five types of OLED structure. The last 5 nm BeBq_2 layer prepared with a two-step process (device A, 0.03 nm/s and device B, 0.3 nm/s) on bulk BeBq_2 (55 nm and 1.3 nm/s). The reference devices were used at the constant deposition rates of 1.3 (device C), 0.3 (device D), and 0.03 (device E) nm/s in bulk BeBq_2 EML/ETL (60 nm). All devices were driven with constant current density of 100 mA/cm².

1.3 nm/s upon the bulk BeBq_2 . The scanning area of these images was $2 \times 2 \mu\text{m}$ and the morphology of all films revealed a similar island-like surface texture. The average root-mean-square (RMS) roughness of the ultrathin BeBq_2 films with deposition rates of 0.03, 0.3, and 1.3 nm/s on bulk BeBq_2 surface was about 0.26, 0.30, and 0.38 nm, respectively (see Figures 4(a), 4(b), and 4(c)). We also extracted the variation values (the extracted values correspond to the highest and lowest heights) of these devices: 0.95, 1.35, and 1.55 nm for the ultrathin layer deposited at 0.03, 0.3, and 1.3 nm/s, respectively (see Figures 4(d), 4(e), and 4(f)). Note that in Figure 4(c) the deposition rate was kept at 1.3 nm/s for the whole 60 nm. The surface is rough and there are numerous “white spots” with a diameter ~ 200 nm. When decreasing the deposition rate for the final 5 nm at 0.3 and 0.03 nm/s,

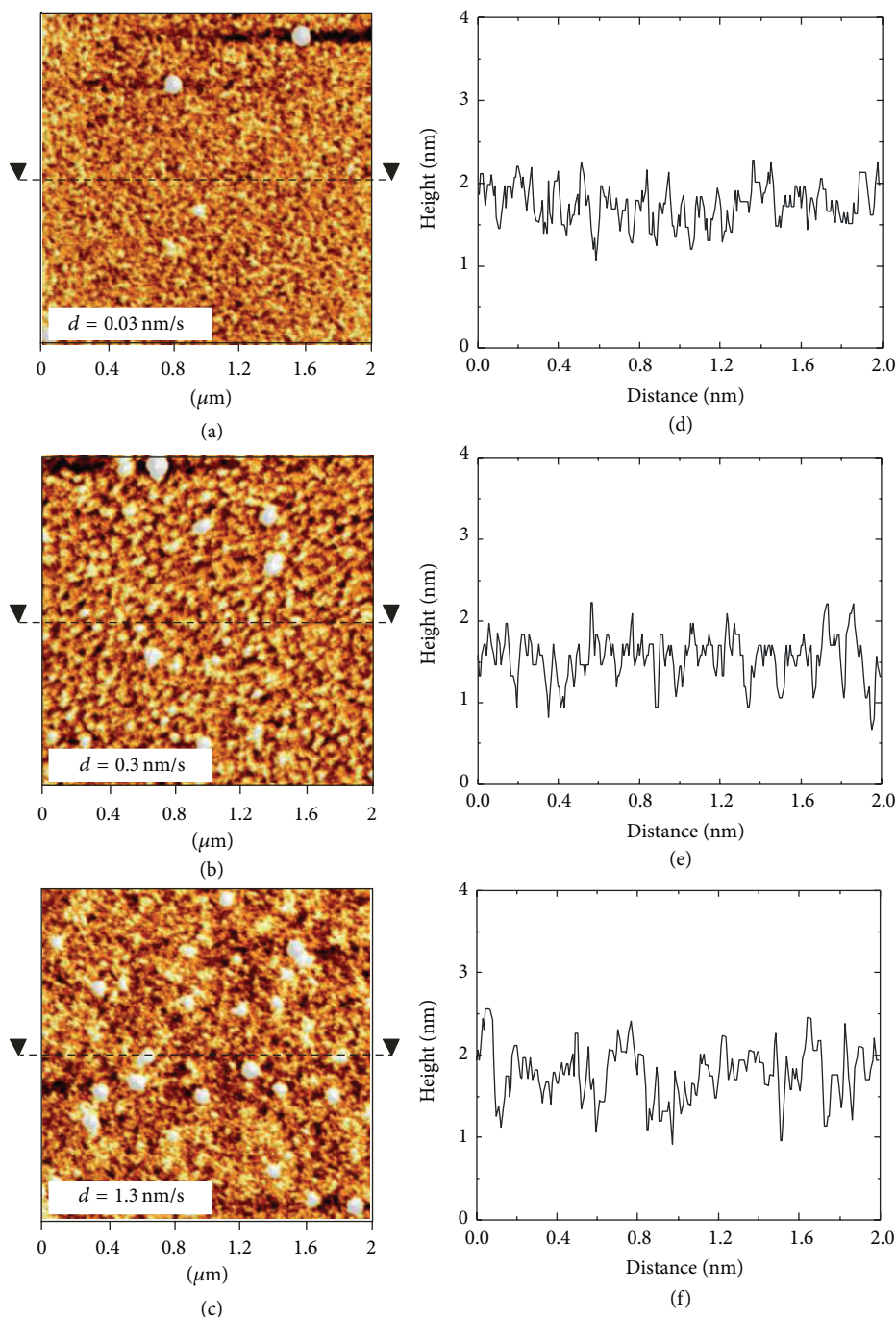


FIGURE 4: The atomic force microscope micrographs of Bebq_2 (5 nm) films prepared with different deposition rates of (a) 0.03, (b) 0.3, and (c) 1.3 nm/s on the bulk material of Bebq_2 (55 nm; 1.3 nm/s) substrate. The depth profiles of ultrathin Bebq_2 with three deposition rates of 0.03 (d), 0.3 (e), and 1.3 (f) nm/s were extracted from the centerline of corresponding images.

it can be seen that the surface became smooth and the number of “white spots” decreased. The dependence of the morphology results on the deposition rate can be explained by the fact that a lower deposition rate in the ultrathin layer enabled the planar Bebq_2 molecules to settle into their lowest energy-packing configuration and produce a smooth surface (see Figure 4(d)). The optimization of the two-step process resulted in a significant decrease to the RMS roughness of the

Bebq_2 surface and the formation of a “good contact” interface between Bebq_2 /electrode. Consequently, we expect that such smooth contact would eliminate the obstruction buildup at the interface between organic/electrode. Conversely, the rough surface morphology of Bebq_2 film (see Figures 4(e) and 4(f)) may result in weak adhesion of the subsequently deposited electrode layer and decrease the electron injection efficiency. The present results suggest that these factors are

strongly affected by the interface qualities of Beq₂/electrode under different deposition rates. With the modification of the contact layer, the 5 nm Beq₂ with lower deposition rate produced a uniform buffer layer that reduced the driving voltage and gave a higher efficiency due to better charge balance. At a low deposition rate, the smooth Beq₂/electrode interface also facilitated stable contact for the subsequently deposited LiF/Al electrode. This explained why the trap distribution upon electrical aging was predominantly concentrated on the cathode side with high deposition rate Beq₂ (device C). On the other hand, for device E with low deposition rate Beq₂, the efficiency was low (as shown in Figure 1(b)), resulting in more serious joule heating near the recombination zone (HTL/Beq₂ interface) that assisted the crystallization process [24, 25] and decreased the PL efficiency.

4. Conclusion

We investigated the influence of the deposition rate of the Beq₂ film on the performance of OLEDs with a Beq₂ film and reached two conclusions. First, the current densities versus driving voltage and luminance versus current densities characteristics of the devices were found to be consistent with the extracted dependence of the carrier injection properties on the film deposition rate. In particular, when ultrathin films were fabricated at low deposition rates, the formation of a smooth Beq₂ surface may strongly enhance charge injection. This conclusion was supported by the electron-only measurements. Second, when the deposition rate for the last 5 nm Beq₂ layer was decreased from 1.3 to 0.03 nm/s, the devices exhibited significantly longer lifetimes compared to similar devices with no changes in the deposition rate. This indicated that the two-step deposition process was responsible for a significant increase in the surface smoothness of the Beq₂/electrode interface, possibly due to the strong and stable adhesion of Beq₂ and subsequently deposited Al electrode.

Conflict of Interests

The authors declare that they have no conflict of interests regarding the publication of this paper.

Acknowledgments

The authors thank the financial support by the National Science Council, ROC, under Grant nos. NSC 101-2221-E-002-156-MY3, 102-2221-E-002-182-MY3, NSC 102-2221-E-131-026-MY2, NSC 102-2221-E-131-030-MY2, NSC 102-2511-S-131-002, NSC 103-ET-E-011-004-ET, NSC 102-2627-E-002-002, and NSC 102-2622-E-011-018-CC3 and Academia Sinica of Taiwan.

References

[1] H. Klauk, "Organic thin-film transistors," *Chemical Society Reviews*, vol. 39, pp. 2643–2666, 2010.

[2] G. Li, R. Zhu, and Y. Yang, "Polymer solar cells," *Nature Photonics*, vol. 6, no. 3, pp. 153–161, 2012.

[3] B. J. Chen, W. Y. Lai, Z. Q. Gao, C. S. Lee, S. T. Lee, and W. A. Gamblig, "Electron drift mobility and electroluminescent efficiency of tris(8-hydroxyquinolinolato) aluminum," *Applied Physics Letters*, vol. 75, p. 4010, 1999.

[4] C. B. Lee, A. Uddin, X. Hu, and T. G. Andersson, "Study of Alq₃ thermal evaporation rate effects on the OLED," *Materials Science and Engineering: B*, vol. 112, pp. 14–18, 2004.

[5] T. Matsushima, K. Shiomura, S. Naka, and H. Murata, "Optical, morphological, structural, electrical, molecular orientation, and electroluminescence characteristics of organic semiconductor films prepared at various deposition rates," *Thin Solid Films*, vol. 520, no. 6, pp. 2283–2288, 2012.

[6] H. W. Zan, Y. H. Hsu, H. F. Meng, C. H. Huang, Y. T. Tao, and W. W. Tsai, "High output current in vertical polymer space-charge-limited transistor induced by self-assembled monolayer," *Applied Physics Letters*, vol. 101, no. 9, Article ID 093307, 2012.

[7] S. Pola, C. H. Kuo, W. T. Peng, M. M. Islam, I. Chao, and Y. T. Tao, "Contorted tetrabenzocoronene derivatives for single crystal field effect transistors: correlation between packing and mobility," *Chemistry of Materials*, vol. 24, pp. 2566–2571, 2012.

[8] F. Padinger, R. S. Rittberger, and N. S. Sariciftci, "Effects of postproduction treatment on plastic solar cells," *Advanced Functional Materials*, vol. 13, no. 1, pp. 85–88, 2003.

[9] G. Li, V. Shrotriya, J. Huang et al., "High-efficiency solution processable polymer photovoltaic cells by self-organization of polymer blends," *Nature Materials*, vol. 4, no. 11, pp. 864–868, 2005.

[10] H. C. Han, C. A. Tseng, C. Y. Du et al., "Enhancing efficiency with fluorinated interlayers in small molecule organic solar cells," *Journal of Materials Chemistry*, vol. 22, pp. 22899–22905, 2012.

[11] C.-F. Lin, S.-W. Liu, C.-C. Lee et al., "Open-circuit voltage and efficiency improvement of subphthalocyanine-based organic photovoltaic device through deposition rate control," *Solar Energy Materials and Solar Cells*, vol. 103, pp. 69–75, 2012.

[12] C. C. Lee, S. W. Liu, and Y. T. Chung, "Effect of deposition rate on device performance and lifetime of planar molecule-based organic light-emitting diodes," *Journal of Physics D: Applied Physics*, vol. 43, no. 7, Article ID 075102, 2010.

[13] J.-H. Lee, C.-I. Wu, S.-W. Liu, C.-A. Huang, and Y. Chang, "Mixed host organic light-emitting devices with low driving voltage and long lifetime," *Applied Physics Letters*, vol. 86, Article ID 103506, 2005.

[14] S.-W. Liu, C.-C. Lee, C.-H. Wang, J.-H. Lee, C.-T. Chen, and J.-K. Wang, "Enhancing performance of planar molecule-based organic light-emitting diodes through deposition-rate optimization: role of molecular packing," *Chemical Physics Letters*, vol. 474, pp. 207–211, 2009.

[15] S.-H. Liao, J.-R. Shiu, S.-W. Liu et al., "Hydroxynaphthyridine-derived group III metal chelates: wide band gap and deep blue analogues of green Alq₃ (tris(8-hydroxyquinolate)aluminum) and their versatile applications for organic light-emitting diodes," *Journal of the American Chemical Society*, vol. 131, pp. 763–777, 2009.

[16] W. Brütting, S. Berleb, and A. G. Mückl, "Device physics of organic light-emitting diodes based on molecular materials," *Organic Electronics*, vol. 2, pp. 1–36, 2001.

- [17] S. T. Lee, Z. Q. Gao, and L. S. Hung, "Metal diffusion from electrodes in organic light-emitting diodes," *Applied Physics Letters*, vol. 75, p. 1404, 1999.
- [18] J.-H. Lee, Y.-H. Ho, T.-C. Lin, and C.-F. Wu, "High-efficiency fluorescent blue organic light-emitting device with balanced carrier transport," *Journal of the Electrochemical Society*, vol. 154, pp. 226–228, 2007.
- [19] H. Aziz, Z. D. Popovic, and N.-X. Hu, "Organic light emitting devices with enhanced operational stability at elevated temperatures," *Applied Physics Letters*, vol. 81, p. 370, 2002.
- [20] C.-C. Lee, M.-Y. Chang, P.-T. Huang, Y.-C. Chen, and S.-W. Liu, "Electrical and optical simulation of organic light-emitting devices with fluorescent dopant in the emitting layer," *Journal of Applied Physics*, vol. 101, p. 114501, 2007.
- [21] S. A. Van Slyke, C. H. Chen, and C. W. Tang, "Organic electroluminescent devices with improved stability," *Applied Physics Letters*, vol. 69, no. 15, pp. 2160–2162, 1996.
- [22] D. Y. Kondakov, J. R. Sandifer, C. W. Tang, and R. H. Young, "Nonradiative recombination centers and electrical aging of organic light-emitting diodes: direct connection between accumulation of trapped charge and luminance loss," *Journal of Applied Physics*, vol. 93, no. 2, pp. 1108–1119, 2003.
- [23] J.-H. Lee, J.-J. Huang, C.-C. Liao, P.-J. Hu, and Y. Chang, "Operation lifetimes of organic light-emitting devices with different layer structures," *Chemical Physics Letters*, vol. 402, pp. 335–339, 2005.
- [24] J. R. Gong, L. J. Wan, S. B. Lei, C. L. Bai, X. H. Zhang, and S. T. Lee, "Direct evidence of molecular aggregation and degradation mechanism of organic light-emitting diodes under joule heating: an STM and Photoluminescence study," *The Journal of Physical Chemistry B*, vol. 109, pp. 1675–1682, 2005.
- [25] H. Aziz and Z. D. Popovic, "Degradation phenomena in small-molecule organic light-emitting devices," *Chemistry of Materials*, vol. 16, pp. 4522–4532, 2004.

Research Article

Investigation Performance and Mechanisms of Inverted Polymer Solar Cells by Pentacene Doped P3HT : PCBM

Hsin-Ying Lee and Hung-Lin Huang

Department of Photonics, Research Center Energy Technology and Strategy, Advanced Optoelectronic Technology Center, National Cheng Kung University, Tainan 701, Taiwan

Correspondence should be addressed to Hsin-Ying Lee; hylee@ee.ncku.edu.tw

Received 24 February 2014; Accepted 13 March 2014; Published 8 April 2014

Academic Editor: Ramunas Lygaitis

Copyright © 2014 H.-Y. Lee and H.-L. Huang. This is an open access article distributed under the Creative Commons Attribution License, which permits unrestricted use, distribution, and reproduction in any medium, provided the original work is properly cited.

The inverted polymer solar cells (PSCs) with pentacene-doped P3HT : PCBM absorption layers were fabricated. It was demonstrated that the pentacene doping modulated the electron mobility and the hole mobility in the resulting absorption layer. Furthermore, by varying the doping content, the optimal carrier mobility balance could be obtained. In addition, the pentacene doping led to an improvement in the crystallinity of the resulting films and made an enhancement in the light absorption, which was partly responsible for the performance improvement of the solar cells. Using the space-charge-limited current (SCLC) method, it was determined that the balanced carrier mobility ($\mu_h/\mu_e = 1.000$) was nearly achieved when a pentacene doping ratio of 0.065 by weight was doped into the P3HT : PCBM : pentacene absorption layer. Compared with the inverted PSCs without the pentacene doping, the short circuit current density and the power conversion efficiency of the inverted PSCs with the pentacene doping ratio of 0.065 were increased from 9.73 mA/cm² to 11.26 mA/cm² and from 3.39% to 4.31%, respectively.

1. Introduction

Over the past decades, much effort has been devoted to improving energy utilization efficiency, to developing renewable energy, and to decreasing overall greenhouse gas emissions [1]. Recently, polymer solar cells (PSCs) have attracted much attention and are thought of as a potential candidate of the next generation solar cells, because they have many advantages, including low cost, flexibility, light weight, and easy fabrication [2, 3]. However, compared with the inorganic solar cells [4–6], the PSCs suffer from two major drawbacks of a lower power conversion efficiency (PCE) and a worse stability [7]. Conventionally, the PSCs were constructed with an Al back cathode electrode, a poly(3,4-ethylene-dioxythiophene) : poly(styrene sulfonate) (PEDOT : PSS) hole transport layer inserted between the polymer absorption layer and the indium tin oxide (ITO) front anode electrode. Unfortunately, the oxygen could diffuse into the absorption layer through the pinholes and grain boundaries within the Al electrode. Consequently, the quality of the absorption layer of PSCs was degraded [8].

Furthermore, the ITO electrode was easily etched by the PEDOT : PSS [9]. These problems were responsible for the instability of the PSCs, which limited the application and commercialization of the devices. To improve the stability of the PSCs, an inverted cell structure for PSCs was previously proposed, where a high-work-function metal (Au or Ag) layer was used as the back contact anode electrode and the PEDOT : PSS hole transport layer was removed [10]. However, the conventional inverted PSCs still suffer from low PCE. To enhance the efficiency, many efforts have been carried out previously. For example, organic or inorganic materials were doped into the P3HT : PCBM absorption layers of the PSCs to enhance the light absorption or the carrier mobility. Various promising doping materials were previously reported, including cadmium selenide (CdSe) [11], zinc oxide (ZnO) [12], nanodiamonds [13], single wall carbon nanotubes (SWCNTs) [14], ferric oxide (Fe₃O₄) [15], graphene [16], 3-hydroxyflavone (3-HF) [17], and perylene [18]. In these previous reports, the performances of PSCs were improved owing to an increase of light absorption. Consequently, the amount of the photoinduced charge carriers in the absorption

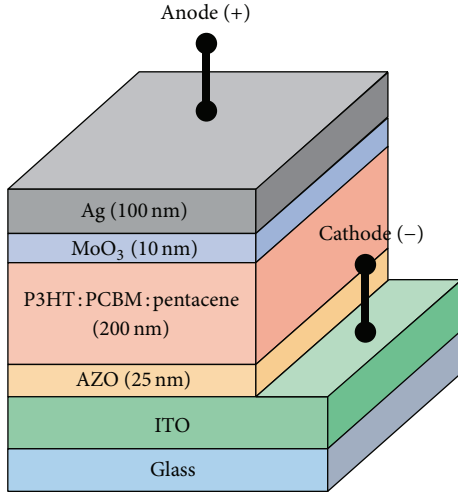


FIGURE 1: Schematic configuration of the inverted PSCs structure.

layer was increased. However, the PCE of these PSCs with the absorption layer doped with various materials was still not satisfactory, only 1.5%~3.6%. It has been pointed out that the carrier mobility mismatching in the absorption layer was one of the main reasons for the low PCE [19]. The balanced carrier mobility could decrease the carrier recombination in the absorption layer and hence increase the photocurrent of the resulting solar cells [20].

Recently, many efforts have been devoted to balancing the carrier mobility in the absorption layer. It was reported that the carrier mobility could be modulated by doping pentacene into the absorption layer of the conventional PSCs and the performances of the resulting devices were improved [21]. In order to further improve the performance of the PSCs, in this work, the inverted PSCs with pentacene-doped absorption layer were fabricated and investigated. To clearly identify the electron mobility and the hole mobility in the absorption layers, the electron-only devices and the hole-only devices with the corresponding absorption layers were analyzed, respectively, using the space-charge-limited current (SCLC) method. By varying pentacene doping content in the absorption layer, the optimal mobility balance condition was obtained. It is clarified that the PCE of the inverted PSCs was enhanced by properly balancing the carrier mobility in the absorption layer.

2. Experiments

Figure 1 shows the schematic configuration of the inverted polymer solar cells (PSCs). The 25 nm thick Al-doped ZnO (AZO) film was deposited on the ITO-coated glass substrate using a magnetron radio-frequency (RF) sputtering system. The AZO film worked as the electron transportation and hole blocking layer. The mixed solution of poly(3-hexylthiophene) (P3HT), (6,6)-phenyl-C₆₁-butyric acid methyl ester (PCBM), and pentacene with given mixing ratio in the 1,2-dichlorobenzene (DCB) was then spread on the AZO film using a spin-coating technique to form a

P3HT:PCBM:pentacene absorption layer of the inverted PSCs. The thickness of the absorption layer was 200 nm. Subsequently, the deposited absorption layer was annealed in a nitrogen glove box at 110°C for 20 minutes. Finally, the 10 nm thick MoO₃ layer and the 100 nm thick Ag layer were subsequently deposited on the absorption layer as the anode electrode of the inverted PSCs using a thermal evaporator. The absorption area of the inverted PSCs was about 4 mm². Thus fabricated inverted PSCs with various pentacene doping ratios (0, 0.05, 0.06, 0.065, and 0.07 by weight) in the P3HT:PCBM (1:0.8) absorption layers were, respectively, named solar cells A, B, C, D, and E, hereafter. For estimating the hole mobility and the electron mobility in the absorption layer, the hole-only devices of Au/P3HT:PCBM:pentacene/MoO₃/Ag (100/200/10/100 nm) and the electron-only devices of ITO/AZO/P3HT:PCBM:pentacene/Al (300/25/200/100 nm) were fabricated. In this work, ten batches, each batch had six devices, of the electron-only devices, the hole-only devices, and the inverted PSCs were fabricated and measured.

The space-charge-limited current (SCLC) method was used to estimate the hole mobility and the electron mobility in the absorption layer for the hole-only devices and the electron-only devices, respectively. The crystallinity and surface morphology of the absorption layers with various pentacene doping contents were measured using X-ray diffraction (XRD) and atomic force microscopy (AFM), respectively. The current density versus voltage (*J-V*) characteristics of the inverted PSCs were measured at room temperature using a *J-V* curve tracer (Keithley 2400) with an AM 1.5 G solar simulator (100 mW/cm²). The external quantum efficiency (EQE) was measured using a chopped calibrated light beam from a xenon lamp combined with a lock-in amplifier. The absorption and the diffuse reflection spectra of the absorption layer with various pentacene doping contents and the resulting cells were measured using an UV-Vis spectrometer (Hitachi, U4100).

3. Experimental Results and Discussion

The SCLC method was used to estimate the electron mobility (μ_e) and the hole mobility (μ_h) in various absorption layers by using the corresponding electron-only and hole-only devices, respectively. The dark current density-voltage characteristics of the electron-only devices and the hole-only devices with the absorption layers of various pentacene doping contents were shown in Figure 2. The electron mobility of the electron-only devices and the hole mobility of the hole-only devices were estimated by Mott-Gurney law equation shown as follows [22]:

$$J = \frac{9}{8} \epsilon_0 \epsilon_r \mu \frac{V^2}{d^3}, \quad (1)$$

where *J* is the dark current density, $\epsilon_0 \epsilon_r$ is the permittivity of the P3HT:PCBM:pentacene absorption layer, which was estimated to be (average value \pm standard deviation) $(4.50 \pm 0.02) \times 10^{-11}$ F/m from the capacitance-voltage measurement results, μ is the carrier mobility, *V* is the applied voltage, and

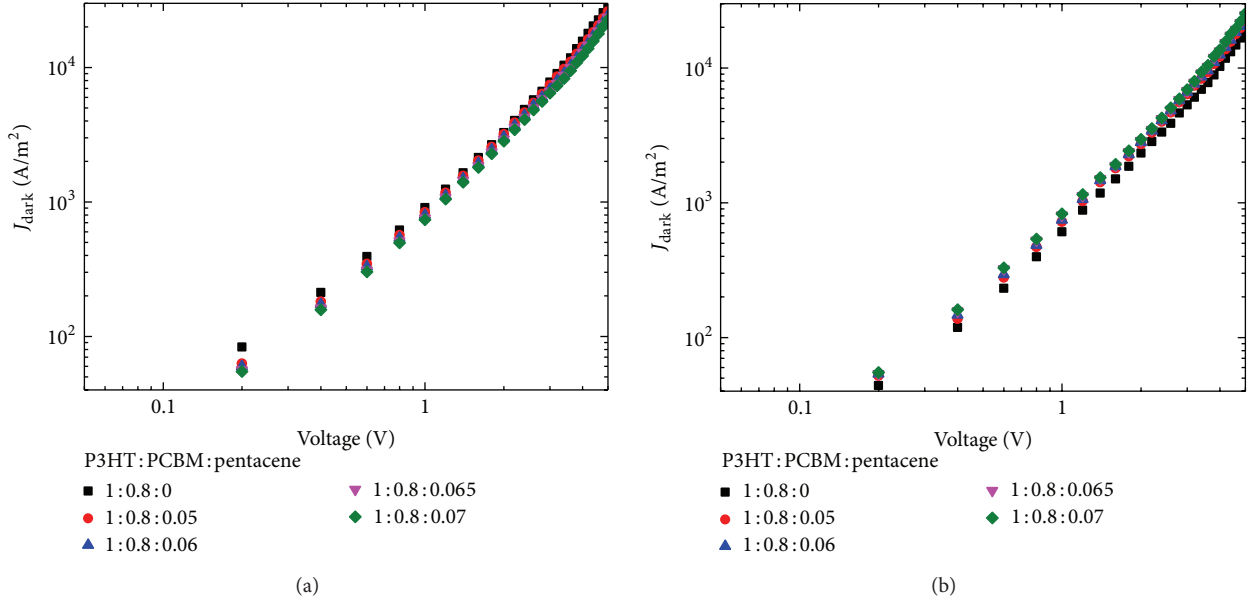


FIGURE 2: The dark current densities for (a) electron-only devices and (b) hole-only devices with the absorption layer of various pentacene doping contents.

TABLE 1: The hole mobility and electron mobility of the hole-only devices and the electron-only devices with various pentacene doping contents.

P3HT : PCBM : pentacene	Hole mobility μ_h (10^{-3} cm ² /Vs)	Electron mobility μ_e (10^{-3} cm ² /Vs)	μ_h/μ_e
1 : 0.8 : 0	0.94 ± 0.01	1.37 ± 0.01	0.686 ± 0.002
1 : 0.8 : 0.05	1.09 ± 0.02	1.29 ± 0.02	0.845 ± 0.002
1 : 0.8 : 0.06	1.13 ± 0.01	1.21 ± 0.01	0.934 ± 0.001
1 : 0.8 : 0.065	1.16 ± 0.01	1.16 ± 0.01	1.000 ± 0.001
1 : 0.8 : 0.07	1.18 ± 0.02	1.13 ± 0.02	1.044 ± 0.001

d is the thickness of the absorption layer of the devices. This equation could be also rewritten and shown as follows:

$$\log(J) = \log\left(\frac{9\varepsilon_0\varepsilon_r\mu}{8d^3}\right) + 2\log(V). \quad (2)$$

To conform the Mott-Gurney law, the slope of $\log(J)$ - $\log(V)$ curve for the electron-only devices and the hole-only devices should be 2. In this work, the applied voltage of 1.7 V matched in Mott-Gurney law was chosen to estimate the hole mobility of the hole-only devices and the electron mobility of the electron-only devices. Thus, the electric field (E) of all devices estimated by the formula of $E = V/d$, where V of 1.7 V is the applied voltage and d of 200 nm is the thickness of the absorption layer, was 8.5×10^4 V/cm. The resulting hole mobility and the electron mobility in the absorption layers with various pentacene doping contents are listed in Table 1. It can be seen that the hole mobility of the absorption layer increased and the electron mobility of the absorption layer decreased with increasing the pentacene doping content. In particular, for the P3HT:PCBM absorption layer with pentacene doping ratio of 0.065, the hole mobility, compared

with the P3HT:PCBM absorption layer, was increased from $(0.94 \pm 0.01) \times 10^{-3}$ cm²/Vs to $(1.16 \pm 0.01) \times 10^{-3}$ cm²/Vs. Contrarily, the electron mobility in the absorption layer was decreased from $(1.37 \pm 0.01) \times 10^{-3}$ cm²/Vs to $(1.16 \pm 0.01) \times 10^{-3}$ cm²/Vs. The opposite variation of the electron mobility and the hole mobility with pentacene doping content indicated that the ratio of the hole mobility and the electron mobility was accordingly modulated. As seen from the results listed in Table 1, the carrier mobility ratio varied with the pentacene content and, in particular, balanced carrier mobility of 1.000 ± 0.001 was obtained in the absorption layer with a pentacene doping ratio of 0.065 by weight.

The variation of the carrier mobility upon pentacene doping can be understood based on the photovoltaic process in the polymer solar cells (PSCs) described below. Figure 3 shows the carrier transport process as well as the energy level diagram of the component materials in the inverted PSCs with P3HT:PCBM: pentacene absorption layer. In the process, the generation and transport of the carriers in the absorption layer played the most important role and were illustrated in detail in Figure 4. As seen from Figure 4,

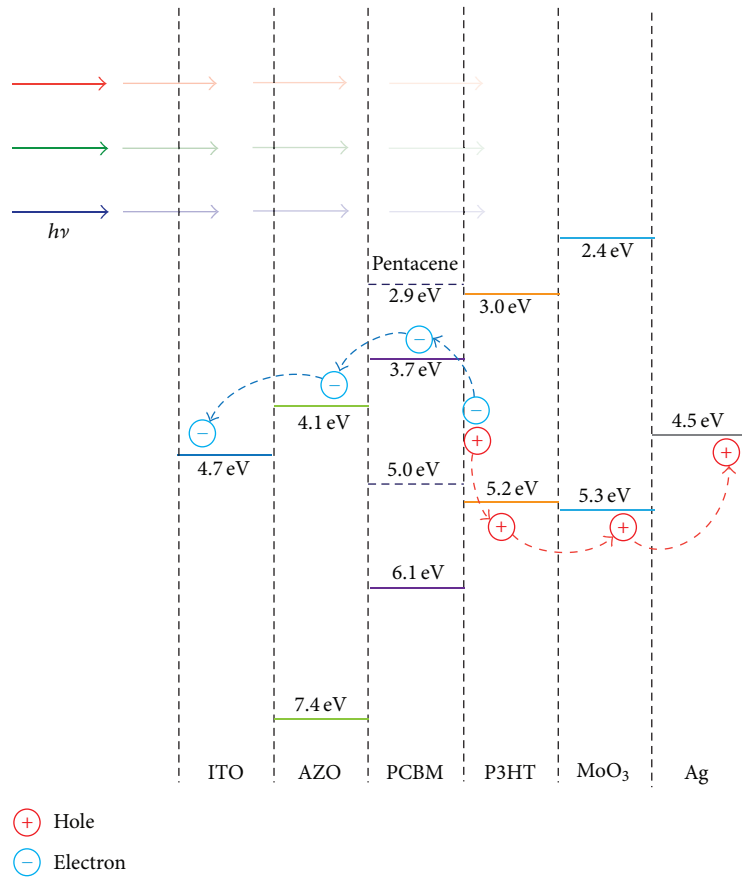


FIGURE 3: Schematic diagram of energy levels for inverted PSCs with pentacene-doped absorption layer.

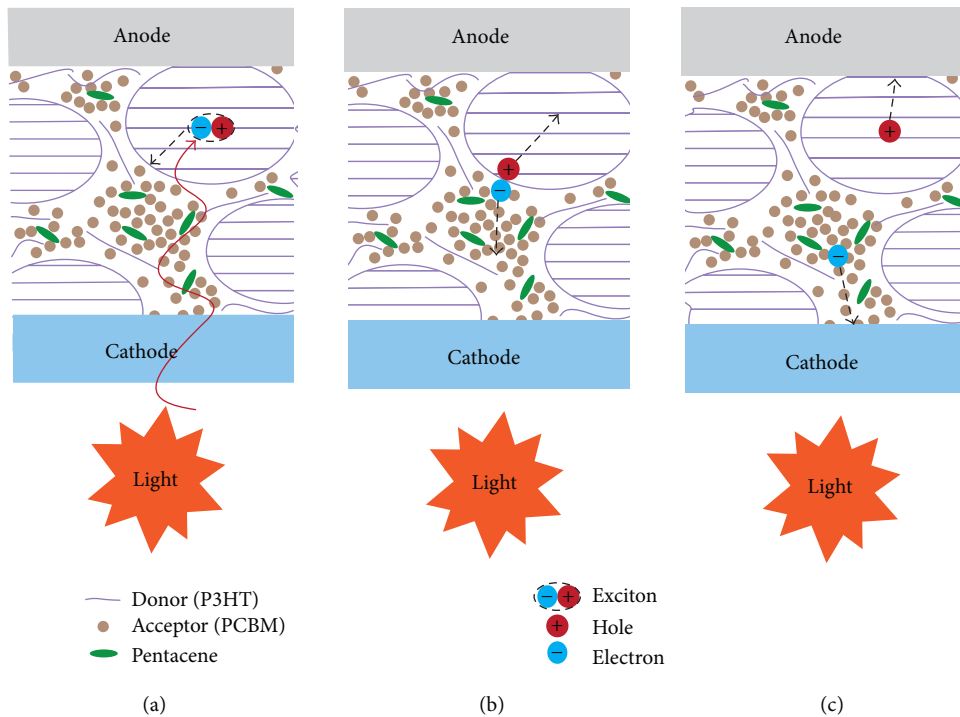


FIGURE 4: Schematics of photocurrent generation in P3HT : PCBM : pentacene system.

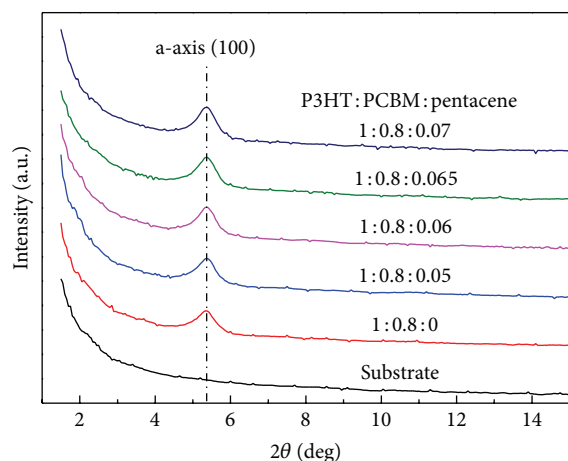


FIGURE 5: XRD spectra of the absorption layers with various pentacene doping contents.

the domains of the donor material were separated in the acceptor materials. When the incident light was absorbed by the donor material, electron-hole excitons were generated in P3HT, as shown in Figure 4(a). The excitons diffused to the interface between the donor and acceptor materials, as shown in both Figures 3 and 4(b). At the interface, the excitons were dissociated and the resulting electrons are transited into the electronegative acceptor materials, whereas the resulting holes remained in the P3HT, as shown in Figure 4(c). Afterwards, the resultant electrons and holes are transported towards the corresponding electrodes [23] as shown in Figure 3. However, due to the energy difference between LUMO of pentacene (electron affinity, 2.9 eV) [24] and the LUMO of PCBM (electron affinity, 3.7 eV) [25], as shown in Figure 3, the addition of pentacene doped into the absorption layer obstructed the electron transportation and decreased the electron mobility in the absorption layer. Consequently, the electron mobility in the absorption layer decreased with an increase of the pentacene doping content. On the other hand, the hole mobility enhancement could be attributed to the improvement in the crystallinity of the P3HT, as reported previously [26]. To demonstrate this phenomenon, the crystallinity analyses of the absorption layers with various pentacene doping contents were carried out using XRD and the results are shown in Figure 5. As shown in Figure 5, the XRD spectra of all the deposited absorption layers exhibited a (100) diffraction peak of the a-axis orientation of P3HT [27]. Moreover, the intensity of the diffraction peak increased with an increase of the pentacene doping content. These results indicated that the crystallinity of the P3HT in the absorption layer was improved by doping the pentacene. This phenomenon indicated that the hole mobility enhancement could be attributed to the enhancement in the crystallinity, induced by pentacene doping, of the P3HT in the absorption layer.

Except the mobility balance in the absorption layer, changes in the other properties of the absorption layer upon pentacene doping might affect the performances of the resulting solar cells. Figure 6 shows the absorption spectra, in

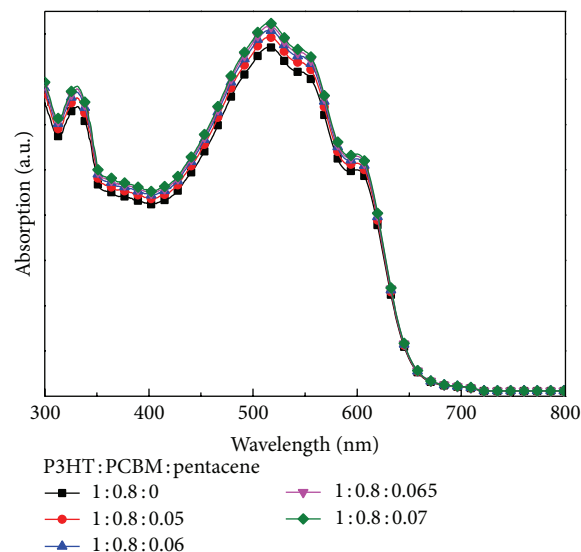


FIGURE 6: The UV-Vis absorption spectra of the absorption layers with various pentacene doping contents.

which the wavelength ranged from 300 nm to 800 nm, of the absorption layers with various pentacene doping contents. As shown in Figure 6, the absorption of the absorption layers increased with an increase of the pentacene doping weight ratio. The absorption enhancement is obviously favorable to the solar cell performance. In general, the absorptivity of the polymer is larger as the electric field of the incident light is aligned parallel to the orientation of the polymer main chains [28]. In other words, the improvement of the P3HT crystallinity enhances its absorption for the light incident perpendicularly to the main chains of the crystalline P3HT. In our case, as observed above by XRD analysis, the intensity of the (100) diffraction peak for the P3HT, which corresponded to an alignment of P3HT main chain parallelly to the substrate [27], increased with an increase of the pentacene doping content. It implied an improvement of P3HT crystallization with its main chain parallel to the substrate. Therefore, according to the previous observation [28], the absorptivity enhancement of the absorption layer was attributed to the crystallinity improvement of the P3HT in the pentacene-doped absorption layer. Furthermore, Figure 7 shows the surface morphologies of the absorption layers with various pentacene doping contents. The root mean square (rms) surface roughness of the P3HT:PCBM:pentacene (1:0.8:0, 1:0.8:0.05, 1:0.8:0.06, 1:0.8:0.065, and 1:0.8:0.07) absorption layer was 1.94 nm, 2.93 nm, 3.23 nm, 3.69 nm, and 3.93 nm, respectively. It could be found that the surface of the P3HT:PCBM:pentacene absorption layer was more roughened with an increase of the pentacene doping content. It was reported previously that the larger roughened surface of the P3HT:PCBM films indicated that the P3HT had better crystallinity [13, 29]. Based on this observation, it could also be deduced that the crystallinity of the P3HT:PCBM:pentacene absorption layer was improved with an increase of the pentacene content, which was consistent with the above-mentioned XRD measurement results.

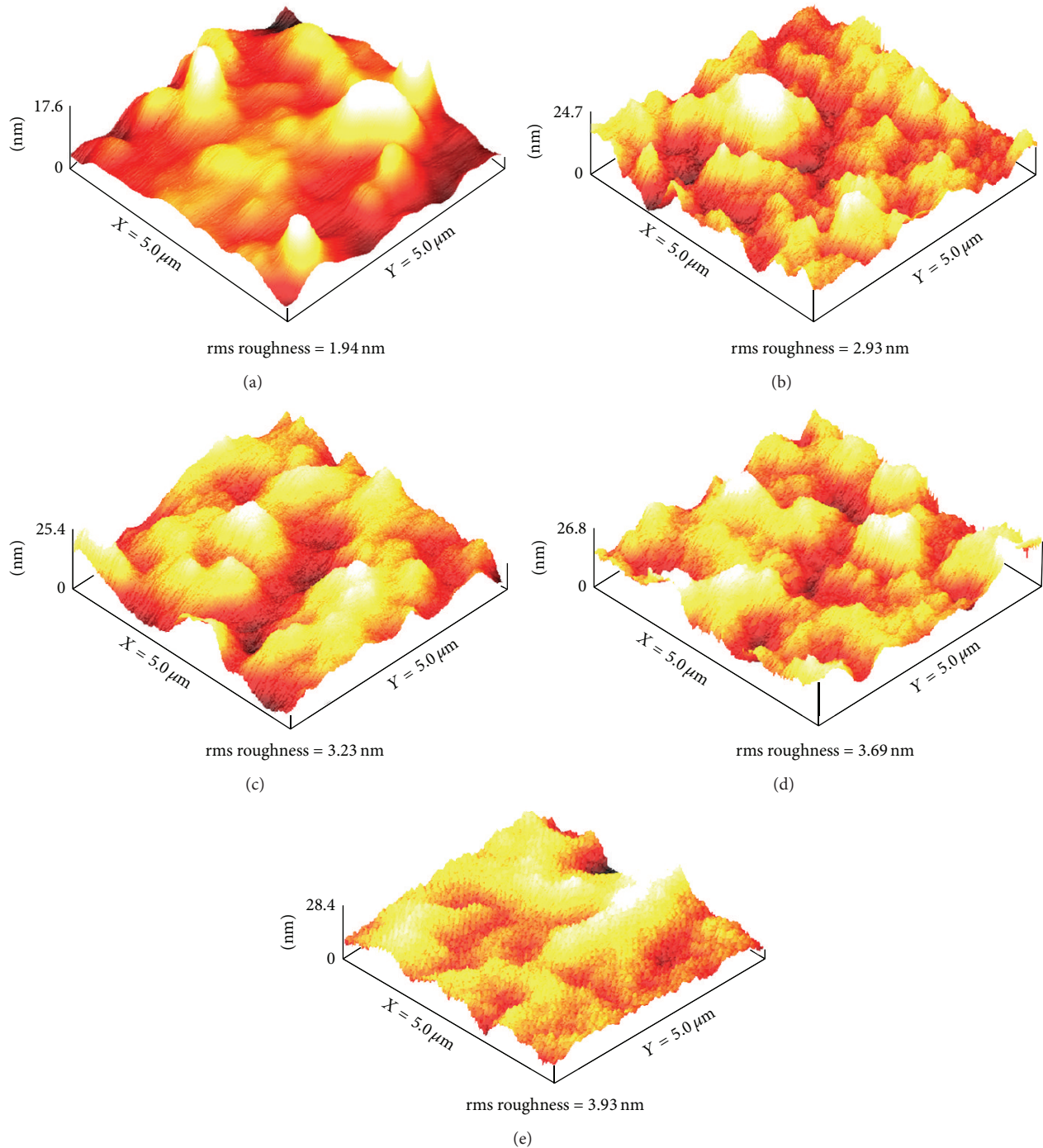


FIGURE 7: AFM images and rms surface roughness of the absorption layers with the pentacene doping ratio of (a) 0, (b) 0.05, (c) 0.06, (d) 0.065, and (e) 0.07 by weight.

Moreover, the increased surface roughness could enhance the light utilization via internal reflection and scattering at the roughened surface, which was also beneficial to the exciton production. To clearly demonstrate this feature, the reflectivity spectra of the P3HT:PCBM: pentacene inverted PSCs with various pentacene doped absorption layers were measured and the results are shown in Figure 8. As shown in Figure 8, the reflectivity of the inverted PSCs was slightly

decreased with an increase of the pentacene doping content, which implied that the diffused reflection light from the roughened surface was more effectively absorbed by absorption layer. Besides, the roughened surface increased the contact area between the polymer film and the metal anode. Therefore, the photocurrent of the PSCs could be increased [30]. As demonstrated in the above discussion, pentacene doping improved the crystallinity of the P3HT in

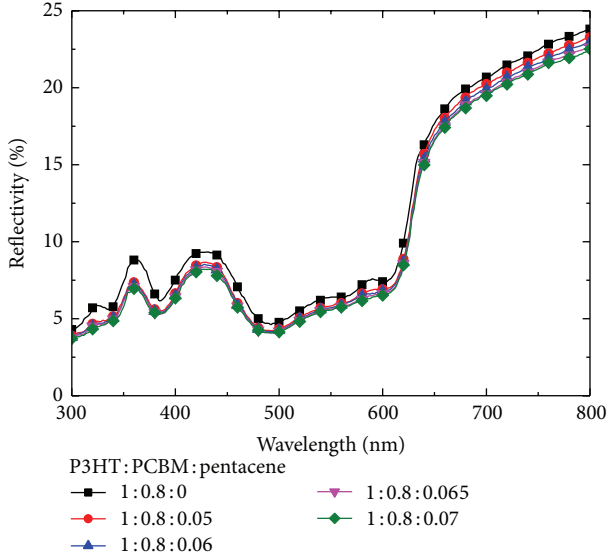


FIGURE 8: The reflectivity of the inverted PSCs with various pentacene-doped absorption layers.

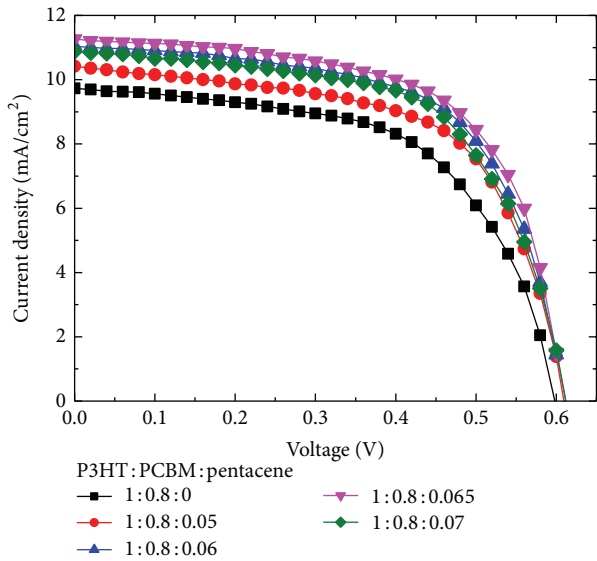


FIGURE 9: The current density-voltage characteristics of the inverted PSCs (solar cells A, B, C, D, and E).

the absorption layer, which in turn caused changes in the carrier mobility, absorption, and surface roughness of the absorption layer. All of these changes affected the performances of the resulting devices.

Figure 9 shows the J - V characteristics of the inverted PSCs with absorption layer of various pentacene doping contents. The photovoltaic characteristics of solar cells A, B, C, D, and E, including short circuit current density (J_{sc}), open circuit voltage (V_{oc}), fill factor (FF), and power conversion efficiency (PCE), were derived from the measured J - V characteristics and the results are listed in Table 2. It was found that only the open circuit voltage V_{oc} was kept nearly the same for all the fabricated devices. This fact could

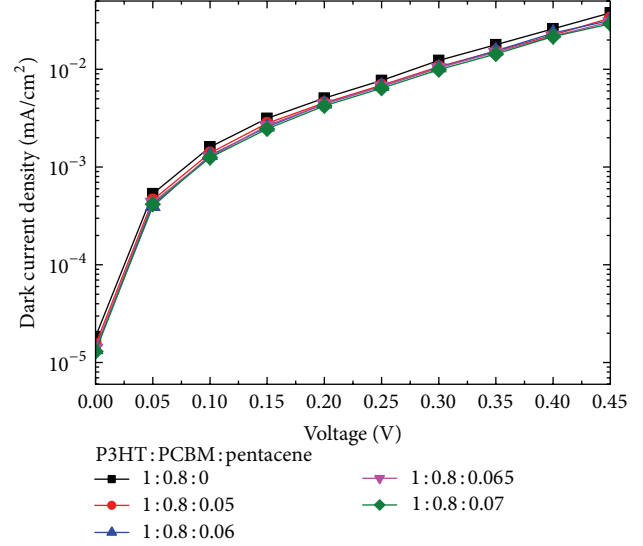


FIGURE 10: Dark current density-voltage characteristics of the inverted PSCs with various pentacene-doped absorption layers.

be evidenced from the relationship of V_{oc} with the reverse saturation current density J_0 [31]:

$$V_{oc} = \frac{nKT}{q} \ln \left[\left(\frac{J_{ph}}{J_0} \right) + 1 \right], \quad (3)$$

where n is the ideality factor, q is the electron charge, K is Boltzmann's constant, T is the absolute temperature, J_{ph} is the photocurrent density, and J_0 is deduced by extrapolating the linear regions of the dark current density-voltage curve (Figure 10) to $V = 0$. These devices with various pentacene doping contents exhibited similar dark current density and correspondingly had the similar V_{oc} . It could be seen that the performances, other than V_{oc} , of the inverted PSCs were improved by doping pentacene of a low ratio into the absorption layer and were optimized when the weight ratio of pentacene was 0.065 (solar cell D). For this optimized cell, the J_{sc} and PCE were $11.26 \pm 0.04 \text{ mA/cm}^2$ and $4.31 \pm 0.03\%$, respectively, which were obviously better than those of $9.73 \pm 0.03 \text{ mA/cm}^2$ and $3.39 \pm 0.02\%$ for solar cell A. To further investigate the variation of the above-mentioned solar cell performances, the external quantum efficiency (EQE) of the inverted PSCs with various pentacene doping contents was measured in the wavelength ranged from 300 nm to 800 nm. The results, as shown in Figure 11, exhibited a similar variation as the pentacene content varied. For example, at the wavelength of 515 nm, the EQE of solar cells A, B, C, D, and E was $51.4 \pm 0.1\%$, $55.0 \pm 0.1\%$, $57.4 \pm 0.1\%$, $59.5 \pm 0.1\%$, and $58.3 \pm 0.1\%$, respectively, in which solar cell D was the best one.

The results discussed above indicated that the solar cell efficiency (EQE or PCE) was increased with an increase of the pentacene doping content in the absorption layer when the doping ratio was low and reached the maximum at the doping ratio of 0.065. When the pentacene doping ratio was further increased to 0.07 (solar cell E), the EQE was

TABLE 2: The parameters of the inverted polymer solar cells with various pentacene doping contents.

Solar cell	P3HT:PCBM:pentacene	J_{sc} (mA/cm ²)	V_{oc} (V)	FF (%)	PCE (%)
A	1:0.8:0	9.73 ± 0.03	0.598 ± 0.001	58.3 ± 0.1	3.39 ± 0.02
B	1:0.8:0.05	10.41 ± 0.03	0.609 ± 0.001	60.1 ± 0.2	3.87 ± 0.03
C	1:0.8:0.06	11.04 ± 0.03	0.610 ± 0.001	62.2 ± 0.2	4.19 ± 0.03
D	1:0.8:0.065	11.26 ± 0.04	0.611 ± 0.001	62.6 ± 0.1	4.31 ± 0.03
E	1:0.8:0.07	10.87 ± 0.04	0.611 ± 0.001	61.3 ± 0.1	4.07 ± 0.03

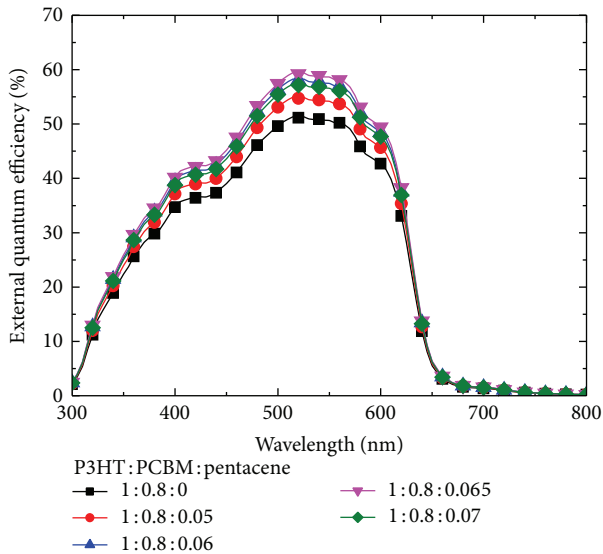


FIGURE 11: External quantum efficiency spectra of the inverted PSCs (solar cells A, B, C, D, and E).

degraded. The efficiency improvement at lower pentacene doping ratio could be attributed to both the enhancement in the absorptivity of the absorption layer and the improvement in the carrier mobility balance. Obviously, the efficiency degradation at higher doping ratio could not be ascribed to the change in the absorptivity of the absorption layer. As mentioned above, the absorptivity increased monotonically with the pentacene doping ratio, which tended to enhance the solar cell efficiency. However, it was noticed that the efficiency of the solar cell varied in a similar way as the carrier mobility ratio did (see Table 1). The optimal efficiency was achieved at the same pentacene doping ratio when the mobility in the absorption layer was properly balanced. At a higher doping ratio, say 0.07, the EQE degraded, while the carrier mobility ratio was increased to 1.044 ± 0.001 , departing obviously from the balance. This unbalanced mobility resulted in an accumulation of low mobility carriers, causing an increase in carrier recombination and a decrease in PCE and EQE. This kind of correlation between EQE and the mobility balance implied that the carrier mobility balance played an important role in the efficiency variation.

4. Conclusion

In summary, the inverted PSCs with various pentacene-doped absorption layers were fabricated. Using the SCLC

method to measure and estimate the hole mobility and the electron mobility in the resulting absorption layer with various pentacene doping contents, it was revealed that the carrier mobility in the absorption layer could be modulated by doping various pentacene contents. In particular, the required carrier mobility balance ($\mu_h/\mu_e = 1.000$) was obtained in the P3HT:PCBM absorption layer with the pentacene doping ratio of 0.065. Using the absorption layer with the balanced carrier mobility could reduce the carrier recombination in the absorption layers and hence enhance the photocurrent of the resulting inverted PSCs. Moreover, more electron-hole excitons were generated in the pentacene-doped absorption layer due to larger absorptivity and larger surface roughness, which provided additional contribution to the performance improvement. The maximum PCE of $4.31 \pm 0.03\%$ was obtained for the inverted PSCs with the pentacene doping ratio of 0.065 in the absorption layer.

Conflict of Interests

The authors declare that there is no conflict of interests regarding the publication of this paper.

Acknowledgment

The authors gratefully acknowledge the support from the Advanced Optoelectronic Technology Center and Research Center Energy Technology and Strategy of the National Cheng Kung University, the Bureau of Energy, Ministry of Economic Affairs of the Republic of China under Contract no. TDPA 101-EC-17-A-08-S1-204 and the National Science Council of Taiwan under Contract no. NSC 102-3113-P-492-002 and NSC 101-2628-E-006-017-MY3.

References

- [1] G. Najafi, B. Ghobadian, T. Tavakoli, D. R. Buttsworth, T. F. Yusaf, and M. Faizollahnejad, "Performance and exhaust emissions of a gasoline engine with ethanol blended gasoline fuels using artificial neural network," *Applied Energy*, vol. 86, no. 5, pp. 630–639, 2009.
- [2] L. Li, D. L. Jacobs, Y. Che et al., "Poly(3-hexylthiophene) nanofiber networks for enhancing the morphology stability of polymer solar cells," *Organic Electronics*, vol. 14, no. 5, pp. 1383–1390, 2013.
- [3] L. Qiao, D. Wang, L. Zuo et al., "Localized surface plasmon resonance enhanced organic solar cell with gold nanospheres," *Applied Energy*, vol. 88, no. 3, pp. 848–852, 2011.

- [4] S. W. Liang, C. H. Hsu, and C. C. Tsai, "Effect of TCO/ $\mu\text{c-Si:H}$ interface modification on hydrogenated microcrystalline silicon thin-film solar cells," *International Journal of Photoenergy*, vol. 2013, Article ID 756084, 6 pages, 2013.
- [5] D. M. Chen, Z. C. Liang, L. Zhuang, Y. H. Lin, and H. Shen, "A novel method to achieve selective emitter for silicon solar cell using low cost pattern-able a-Si thin films as the semi-transparent phosphorus diffusion barrier," *Applied Energy*, vol. 92, pp. 315–321, 2012.
- [6] C. Y. Tseng and C. T. Lee, "Mechanisms of $(\text{NH}_4)_2\text{S}_x$ -treated III-V compound triple-junction solar cells incorporating with hybrid electrode," *Applied Physics Letters*, vol. 101, no. 3, Article ID 033902, 4 pages, 2012.
- [7] Y. Sun, J. H. Seo, C. J. Takacs, J. Seifert, and A. J. Heeger, "Inverted polymer solar cells integrated with a low-temperature-annealed sol-gel-derived ZnO film as an electron transport layer," *Advanced Materials*, vol. 23, no. 14, pp. 1679–1683, 2011.
- [8] J. Li, X. Huang, J. Yuan, K. Lu, W. Yue, and W. Ma, "A new alcohol-soluble electron-transporting molecule for efficient inverted polymer solar cells," *Organic Electronics*, vol. 14, no. 9, pp. 2167–2171, 2013.
- [9] Y. M. Chang and C. Y. Leu, "Solvent extraction induced nanoporous zinc oxide as an electron transport layer for inverted polymer solar cells," *Organic Electronics*, vol. 13, no. 12, pp. 2991–2996, 2012.
- [10] H. Y. Lee, H. L. Huang, and C. T. Lee, "Performance enhancement of inverted polymer solar cells using roughened Al-doped ZnO nanorod array," *Applied Physics Express*, vol. 5, no. 12, Article ID 122302, 3 pages, 2012.
- [11] E. K. Park, H. Fu, M. Choi, W. Luan, and Y. S. Kim, "Effects ligand-exchanged cadmium selenide nanoparticles on the performance of P3HT:PCBM: CdSe ternary system solar cells," *Bulletin of the Korean Chemical Society*, vol. 34, no. 8, pp. 2321–2324, 2013.
- [12] V. Kruefu, E. Peterson, C. Khantha, C. Siritwong, S. Phanichphant, and D. L. Carroll, "Flame-made niobium doped zinc oxide nanoparticles in bulk heterojunction solar cells," *Applied Physics Letters*, vol. 97, no. 5, Article ID 053302, 3 pages, 2010.
- [13] Y. J. Hsiao, T. H. Fang, L. W. Ji, Y. C. Lee, and B. T. Dai, "Nanodiamonds embedded in P3HT:PCBM for enhancing efficiency and reliability of hybrid photovoltaics," *Electrochemical and Solid-State Letters*, vol. 15, no. 4, pp. K27–K30, 2012.
- [14] E. Kymakis, N. Kornilios, and E. Koudoumas, "Carbon nanotube doping of P3HT:PCBM photovoltaic devices," *Journal of Physics D: Applied Physics*, vol. 41, no. 16, Article ID 165110, 5 pages, 2008.
- [15] W. Zhang, Y. Xu, H. Wang, C. Xu, and S. Yang, " Fe_3O_4 nanoparticles induced magnetic field effect on efficiency enhancement of P3HT:PCBM bulk heterojunction polymer solar cells," *Solar Energy Materials and Solar Cells*, vol. 95, no. 10, pp. 2880–2885, 2011.
- [16] Z. Liu, D. He, Y. Wang, H. Wu, and J. Wang, "Graphene doping of P3HT:PCBM photovoltaic devices," *Synthetic Metals*, vol. 160, no. 9–10, pp. 1036–1039, 2010.
- [17] Y. M. Sung, F. C. Hsu, C. T. Chen, W. F. Su, and Y. F. Chen, "Enhanced photocurrent and stability of inverted polymer/ZnO-nanorod solar cells by 3-hydroxyflavone additive," *Solar Energy Materials and Solar Cells*, vol. 98, pp. 103–109, 2012.
- [18] Y. Lou, Z. Wang, S. Naka, and H. Okada, "Enhanced short-circuit current density in poly(3-hexylthiophene) and 1-(3-methoxycarbonyl)-propyl-1-phenyl-(6,6)C₆₁ based organic solar cells by doping small molecular perylene," *Applied Physics Letters*, vol. 99, no. 3, Article ID 033305, 3 pages, 2011.
- [19] M. Jørgensen, K. Norrman, and F. C. Krebs, "Stability/degradation of polymer solar cells," *Solar Energy Materials and Solar Cells*, vol. 92, no. 7, pp. 686–714, 2008.
- [20] G. Li, V. Shrotriya, J. Huang et al., "High-efficiency solution processable polymer photovoltaic cells by self-organization of polymer blends," *Nature Materials*, vol. 4, no. 11, pp. 864–868, 2005.
- [21] C. T. Lee and C. H. Lee, "Conversion efficiency improvement mechanisms of polymer solar cells by balance electron-hole mobility using blended P3HT:PCBM: pentacene active layer," *Organic Electronics*, vol. 14, no. 8, pp. 2046–2050, 2013.
- [22] P. N. Murgatroyd, "Theory of space-charge-limited current enhanced by Frenkel effect," *Journal of Physics D: Applied Physics*, vol. 3, no. 2, article 308, pp. 151–156, 1970.
- [23] C. Deibel and V. Dyakonov, "Polymer-fullerene bulk heterojunction solar cells," *Reports on Progress in Physics*, vol. 73, no. 9, Article ID 096401, 39 pages, 2010.
- [24] Y. Terada, N. Takeuchi, S. Yoshida, A. Taninaka, O. Takeuchi, and H. Shigekawa, "Effect of defects buried in pentacene/alkanethiol self-assembled monolayer/Au film on its electronic properties visualized by scanning tunneling microscopy/spectroscopy," *Japanese Journal of Applied Physics*, vol. 49, no. 8, Article ID 08LB08, 4 pages, 2010.
- [25] C. W. Chu, V. Shrotriya, G. Li, and Y. Yang, "Tuning acceptor energy level for efficient charge collection in copper-phthalocyanine-based organic solar cells," *Applied Physics Letters*, vol. 88, no. 15, Article ID 153504, 3 pages, 2006.
- [26] P. Vanlaeke, A. Swinnen, I. Haeldermans et al., "P3HT/PCBM bulk heterojunction solar cells: relation between morphology and electro-optical characteristics," *Solar Energy Materials and Solar Cells*, vol. 90, no. 14, pp. 2150–2158, 2006.
- [27] J. H. Park, J. S. Kim, J. H. Lee, W. H. Lee, and K. Cho, "Effect of annealing solvent solubility on the performance of poly(3-hexylthiophene)/methanofullerene solar cells," *Journal of Physical Chemistry C*, vol. 113, no. 40, pp. 17579–17584, 2009.
- [28] S. Y. Chuang, H. L. Chen, W. H. Lee et al., "Regioregularity effects in the chain orientation and optical anisotropy of composite polymer/fullerene films for high-efficiency, large-area organic solar cells," *Journal of Materials Chemistry*, vol. 19, no. 31, pp. 5554–5560, 2009.
- [29] M. Reyes-Reyes, K. Kim, and D. L. Carroll, "High-efficiency photovoltaic devices based on annealed poly(3-hexylthiophene) and 1-(3-methoxycarbonyl)-propyl-1-phenyl-(6,6) C₆₁ blends," *Applied Physics Letters*, vol. 87, no. 8, Article ID 083506, 3 pages, 2005.
- [30] G. Li, V. Shrotriya, Y. Yao, and Y. Yang, "Investigation of annealing effects and film thickness dependence of polymer solar cells based on poly(3-hexylthiophene)," *Journal of Applied Physics*, vol. 98, no. 4, Article ID 043704, 5 pages, 2005.
- [31] L. Stamenic, E. Smiley, and K. Karim, "Low light conditions modelling for building integrated photovoltaic (BIPV) systems," *Solar Energy*, vol. 77, no. 1, pp. 37–45, 2004.

Research Article

Au-Loaded Titanium Dioxide Nanoparticles Synthesized by Modified Sol-Gel/Impregnation Methods and Their Application to Dye-Sensitized Solar Cells

**Hathaithip Ninsonti,^{1,2} Weerasak Chomkitichai,^{2,3} Akira Baba,²
Natda Wetchakun,⁴ Wiyong Kangwansupamonkon,⁵ Sukon Phanichphant,⁶
Kazunari Shinbo,² Keizo Kato,² and Futao Kaneko²**

¹ Department of Chemistry, Faculty of Science, Chiang Mai University, Chiang Mai 50200, Thailand

² Center for Transdisciplinary Research, Niigata University, Niigata 910-2181, Japan

³ Department of Science, Faculty of Science and Technology, Uttaradit Rajabhat University, Uttaradit 53000, Thailand

⁴ Department of Physics and Materials Science, Faculty of Science, Chiang Mai University, Chiang Mai 50200, Thailand

⁵ National Nanotechnology Center, National Science and Technology Development Agency, Pathumthani 12120, Thailand

⁶ Materials Science Research Center, Faculty of Science, Chiang Mai University, Chiang Mai 50200, Thailand

Correspondence should be addressed to Sukon Phanichphant; sphanichphant@yahoo.com

Received 3 December 2013; Accepted 10 March 2014; Published 7 April 2014

Academic Editor: K. R. Justin Thomas

Copyright © 2014 Hathaithip Ninsonti et al. This is an open access article distributed under the Creative Commons Attribution License, which permits unrestricted use, distribution, and reproduction in any medium, provided the original work is properly cited.

Au-loaded TiO₂ nanoparticles were synthesized by the modified sol-gel method together with the impregnation method. Anatase phase of TiO₂ was obtained in all samples with an average particle size of 20 nm. For the enhancement of DSSCs, the dye-sensitized solar cells composed of the ITO/Au-loaded TiO₂/N-719/electrolyte/Pt were fabricated. Au-loaded TiO₂ films were deposited by using squeegee method. Finally, the fabricated cells were studied upon an irradiation of solar light to study the performance. The fabricated cell with up to 1.0 mol% Au-loaded TiO₂ could enhance the performance by localized surface plasmon effect and scattering property.

1. Introduction

Recently, an increase in energy demand has led to significant progress in environmental remediation and renewable energy technologies such as photocatalytic oxidation, adsorption/separation processing, solar cells, fuel cells, and biofuels. One of the various renewable energy options, solar cell, stands out as the most ultimately sustainable choice in terms of its availability and huge potential. The solar cell for renewable energy options is applied through catalyst materials. Titanium dioxide (TiO₂) is one of the most efficient materials for dye-sensitized solar cells (DSSCs) due to its chemical stability, nontoxicity, good electrical properties, and inexpensiveness [1–4]. The phase structure of TiO₂ exists in three polymorphs: anatase, rutile, and brookite. The anatase

TiO₂ is used as dye-sensitized solar cells material because it has band gap energy of 3.2 eV of which the absorption thresholds correspond to 380 nm, suggesting that it is easy for photon-electron transfer under solar light irradiation [3]. At the present time many studies on dye-sensitized solar cells (DSSCs) have been reported due to their high efficiency property and low cost of materials [1–4].

In the active layer of DSSCs, a monolayer of organic dye molecules covered with covalent bond on anatase TiO₂ film is generally used [5]. When the metal nanoparticles are incorporated in TiO₂ film of DSSCs, localized surface plasmon or light scattering can enhance the electric field on the active dye layer which can increase the light absorption [6–8]. Moreover, metal nanoparticles can perform as an electron acceptor from the photo-excited semiconductors.

Therefore, the electron transfer rate could be improved and the increase of photocurrent was obtained [6, 9]. Au has several advantages such as high conductivity and chemical and thermal stability [10]. For these reasons, Au nanoparticles were chosen to induce light scattering and localized surface plasmon excitation for the improvement of DSSCs performance.

There are many ways to synthesize TiO_2 such as precipitation method [11–13], solvothermal method [14–17], sol-gel method [18–22], spray pyrolysis [23–26], and microwave method [27–29]. Sol-gel process consists of 2 main reactions, hydrolysis and condensation [18–22, 30–33]. In our previous work, we reported the preparation of TiO_2 by the modified sol-gel method using cellophane membrane to decrease the diffusion rates of reactants in hydrolysis and condensation steps. This synthesis method had many advantages such as good reproducibility, good ability to obtain TiO_2 in nanosized scale, and good production for high purity products [30, 31].

In this research, TiO_2 and Au-loaded TiO_2 nanoparticles were synthesized by the modified sol-gel method and coupling the modified sol-gel with impregnation methods, respectively. The as-prepared samples were characterized by X-ray diffractometry, scanning electron microscopy, transmission electron microscopy, energy dispersive X-ray spectrophotometry, and Brunauer-Emmett-Teller techniques. The obtained particles were used to enhance DSSCs performance.

2. Experimental

2.1. Preparation of TiO_2 Nanoparticles. Titanium dioxide (TiO_2) nanoparticles were synthesized by the modified sol-gel method [30, 31]. Titanium tetraisopropoxide ($\text{Ti}[\text{OCH}(\text{CH}_3)_2]_4$ (TTIP), Aldrich, England), absolute ethanol ($\text{C}_2\text{H}_5\text{OH}$, Merck, Germany), and ammonia (NH_3 , Merck, Germany) were used as the starting materials for synthesizing TiO_2 nanoparticles. Titanium tetraisopropoxide (20 mL) was dissolved in 250 mL absolute ethanol and mixed until a homogeneous solution was obtained. The mixture of TTIP and absolute ethanol was loaded into a cellophane membrane and suspended for 1 h in a clear solution containing 1:1 ratio of ethanol (95%) and deionized water and 7 mL of ammonia solution (25%) as shown in Figure 1. After the completion of the dialysis process, the suspension was centrifuged at 7500 rpm for 10 min, washed with deionized water, and then dried in an oven at 60°C for 24 h. The white powders were then calcined in a furnace at a temperature of 400°C for 3 h.

2.2. Preparation of Au-Loaded TiO_2 Nanoparticles. The nominal 0.50–3.0 mol% Au-loaded TiO_2 powders were prepared by the impregnation method. The appropriate amounts of gold (III) chloride hydrate ($(\text{H}(\text{AuCl}_4)\cdot\text{H}_2\text{O})$, Electron Microscopy Science) solution were added in TiO_2 nanoparticles as described previously in Section 2.1. Then, the as-prepared samples were mixed until being homogeneous. Finally, the obtained powders were dried at 60°C for 24 h and calcined at 400°C for 3 h.

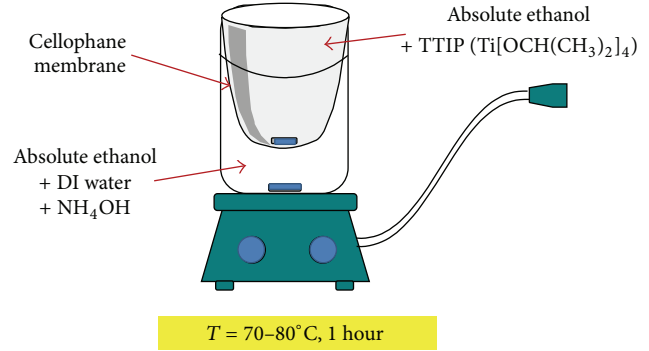


FIGURE 1: Scheme of the modified sol-gel method.

2.3. Characterization of TiO_2 and Au-Loaded TiO_2 Nanoparticles. The crystal structure and crystallinity of TiO_2 and Au-loaded TiO_2 nanoparticles were examined by X-ray diffractometry (JDX-3530, JEOL, Japan) using the Ni-filtered monochromatic with CuK_α radiation. The detection range was $15\text{--}75^\circ$ with the step size of 0.10° ($2\theta^\circ/\text{s}$). Morphologies and particle sizes of TiO_2 and Au-loaded TiO_2 nanoparticles were investigated by scanning electron microscopy (SEM, JSM5410-LV, JEOL, Japan) and transmission electron microscopy (TEM, JEM-2010, JEOL, Japan). The chemical composition of TiO_2 and Au-loaded TiO_2 nanoparticles was examined by energy dispersive X-ray spectrophotometry (EDXS, ISIS300, Oxford, England). Specific surface area (SSA_{BET}) of the samples was investigated by the Brunauer-Emmett-Teller (BET, Micromeritics Tristar 3000). An average particle diameter (d_{BET}) of TiO_2 and Au-loaded TiO_2 nanoparticles was calculated using the following formula: $d_{\text{BET}} = 6 / [(\rho_{\text{TiO}_2} \times \text{SSA}_{\text{BET}} \times \text{wt.\%TiO}_2) + (\rho_{\text{Au}} \times \text{SSA}_{\text{BET}} \times \text{wt.\%Au})]$, where ρ_{TiO_2} and ρ_{Au} are the weight densities of TiO_2 (3.84 g cm^{-3}) and Au (19.30 g cm^{-3}), respectively.

2.4. Fabrication of DSSCs. DSSCs were fabricated by TiO_2 and Au-loaded TiO_2 nanoparticles for comparison of the efficiency performance. ITO glass substrate with a sheet resistance of $10 \Omega/\text{sq}$ was used as an anode. Dish washing liquid solution, water, distilled water, and DI water were used for cleaning of ITO substrate. After cleaning process, squeegee technique was used to deposit TiO_2 or Au-loaded TiO_2 layers as follows: TiO_2 or Au-loaded TiO_2 nanoparticles were dispersed in ethanol with the concentration of 2, 3, 4, or 5 M in order to optimize the appropriate thickness. Then, TiO_2 or Au-loaded TiO_2 pastes were coated on ITO substrates by squeegee technique. TiO_2 or Au-loaded TiO_2 films were then calcined at 450°C for 90 min. To prevent the corrosion of Au particles by iodine electrolyte, Au-loaded TiO_2 films were immersed in 0.001 M 1-octadecanethiol ($\text{CH}_3(\text{CH}_2)_{17}\text{SH}$, Aldrich, England) for 15 h after calcination step. N-719 (di-tetrabutylammonium cis-bis (isothiocyanato) bis(2,2'-bipyridyl-4,4'-dicarboxylato) ruthenium (II), Sigma-Aldrich) was used as a photosensitized dye. TiO_2 or Au-loaded TiO_2 films were immersed in 0.5 mM N-719 dye for 12 h. DSSCs were fabricated as shown in Figure 2.

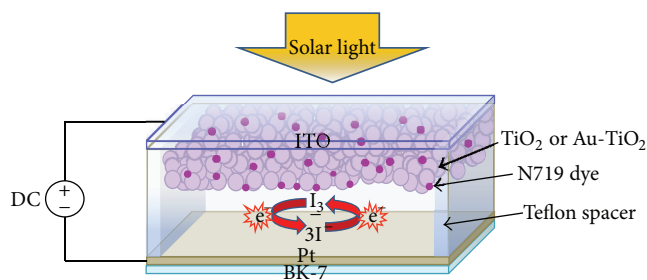


FIGURE 2: Scheme of fabricated dye-sensitized solar cells (DSSCs).

0.1 M LiI, 0.05 M I_2 , 0.6 M tBP, and 0.5 M tetrabutylammonium iodide in acetonitrile were used as electrolyte (for the optimization of the appropriate thickness, only 0.1 M LiI and 0.05 M I_2 in acetonitrile were used as electrolyte). Pt film prepared by vacuum evaporation technique was used as the cathode.

2.5. Characterization of the Fabricated DSSCs. The absorption of TiO_2 and Au-loaded TiO_2 films was observed by UV-vis spectroscopy technique (UV-vis spectrometer, V-650, JASCO). Photovoltaic properties were studied by irradiating a solar simulator (HAL-C100, 100 W compact xenon light source, ASAHI SPECTRA) to the fabricated DSSCs.

3. Results and Discussion

3.1. Synthesis and Characterization of Au-Loaded TiO_2 Nanoparticles. In this research, the TiO_2 and Au-loaded TiO_2 nanoparticles were prepared by the modified sol-gel method and the modified sol-gel method together with the impregnation method, respectively. The preparation of the TiO_2 was followed from our previously reported research [30, 31]. The sol-gel method consists of hydrolysis and condensation of titanium alkoxides, $Ti(OR)_n$, to form oxopolymers, which are converted to an oxide complex as equation mentioned in our previous report [30].

The rates of hydrolysis and condensation are important factors that might affect characteristic of Au-loaded TiO_2 . Smaller particle sizes were obtained from hydrolysis and condensation rates which are controlled by basic solution [34–37]. Consequently, cellophane membrane was used to control the hydrolysis and condensation rates in the reaction to acquire the nanosized particles [30, 31]. Moreover, TiO_2 loading with Au was produced by the impregnation method which is a very simple technique and does not require expensive equipment. The homogeneous powders of TiO_2 show white color, while increase of Au ions changed the color to grayish purple.

The structure confirmation of TiO_2 and Au-loaded TiO_2 nanoparticles was obtained by comparison with the Joint Committee on Powder Diffraction Standards (JCPDS) Card Files numbers 21-1272 and 04-0784. Figure 3 shows the XRD patterns of the TiO_2 and 1.0 mol% Au-loaded TiO_2 nanoparticles. The results of the TiO_2 and 1.0 mol% Au-loaded TiO_2 nanoparticles confirmed anatase structures according

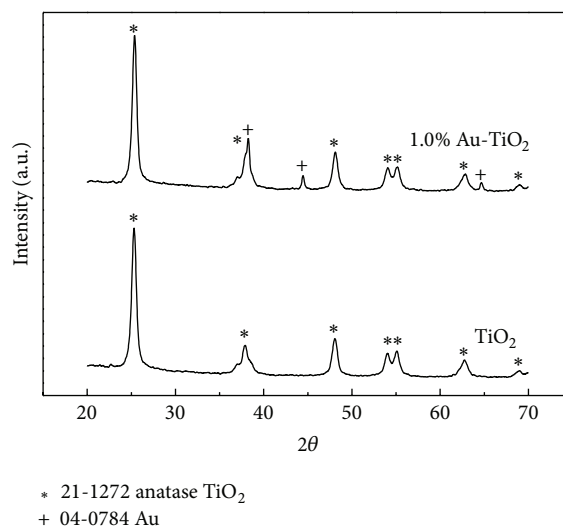


FIGURE 3: XRD patterns of the TiO_2 and 1.0 mol% Au-loaded TiO_2 nanoparticles.

to JCPDS file number 21-1272 [30, 31]. The Au-loading might not affect the phase of TiO_2 nanoparticles. The diffraction peaks of Au were found on Au-loaded TiO_2 nanoparticles at 2θ value of 38.2° and 44.4° according to JCPDS file number 04-0784. The high intensity value of the XRD peaks shows that all of the samples have well crystalline structure and the broad peaks at 2θ value of 25.2° show that the particles have a small average crystallite size.

The specific surface area (SSA_{BET}) of the TiO_2 and Au-loaded TiO_2 nanoparticles was found to be in the range of $69\text{--}109\text{ m}^2\text{ g}^{-1}$ with the particle diameter in the range of 14–21 nm, corresponding well with the XRD results. It was reported that high surface area of TiO_2 active layer has many advantages such as large amount of dye adsorption, high light-harvesting efficiency, rapid electron transport, and low electron recombination [38–40]. Therefore, high photoefficiency could be expected.

Morphologies, particle sizes, and element chemical compositions were investigated by scanning electron microscopy (SEM) as shown in Figure 4(a). The SEM result shows the rough morphology and the presence of agglomerated nanoparticles with an average diameter of 50–100 nm. From the EDS spectra as shown in Figure 4(e), the chemical compositions of 1.0 mol% Au-loaded TiO_2 showed the characteristic X-ray energy level of titanium, oxygen. The characteristic peaks of Au were observed to confirm the presence of Au corresponding to the XRD results. Furthermore, element composition of Au-loaded TiO_2 was investigated by EDS mapping mode. Figures 4(b), 4(c), and 4(d) show element composition of Ti, O, and Au in 1.0 mol% Au-loaded TiO_2 nanoparticles. The presence of Au in the sample was confirmed. Further analysis for the accurate sizes and morphology of the nanoparticles was carried out by TEM observation. The average particle diameter of TiO_2 and Au-loaded TiO_2 nanoparticles was in the range of 15–20 nm as shown in Figure 5.

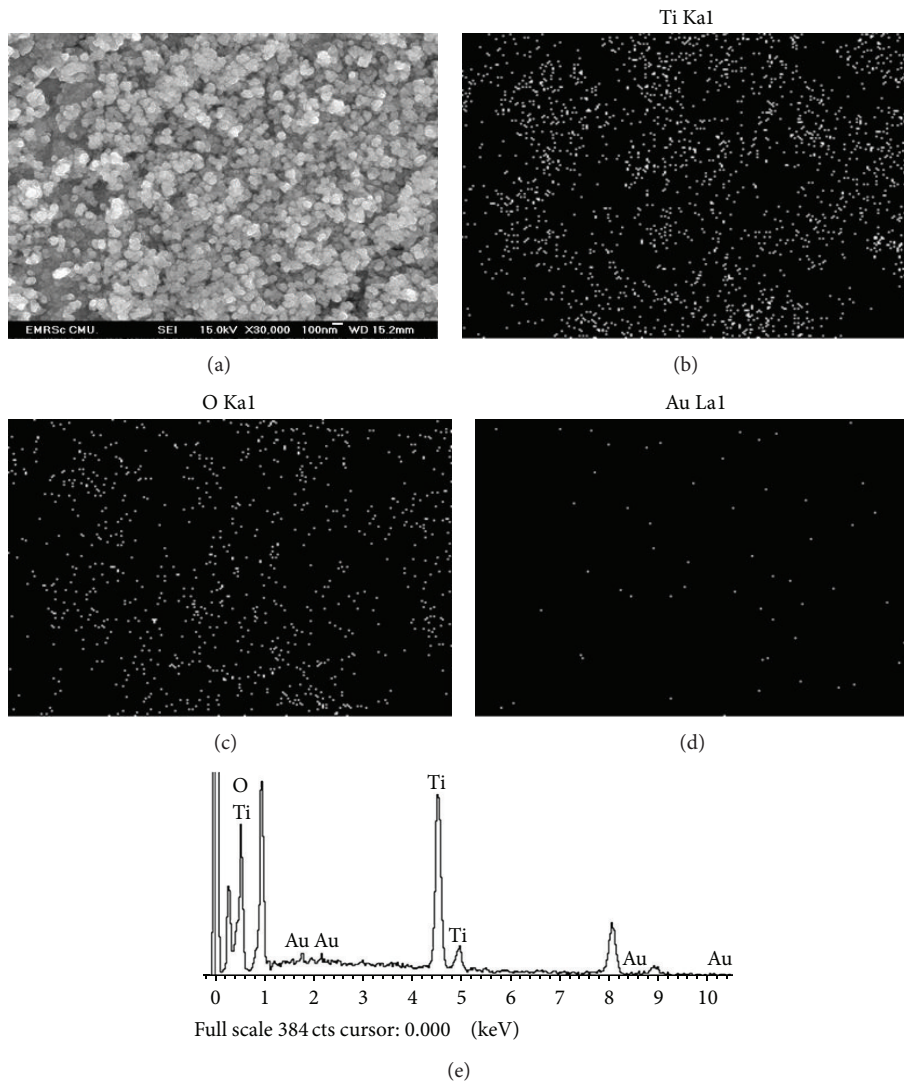


FIGURE 4: (a) SEM micrographs and EDS mapping mode of (b) Ti, (c) O, (d) Au, and (e) EDS spectra of 1.0 mol% Au-loaded TiO_2 nanoparticles.

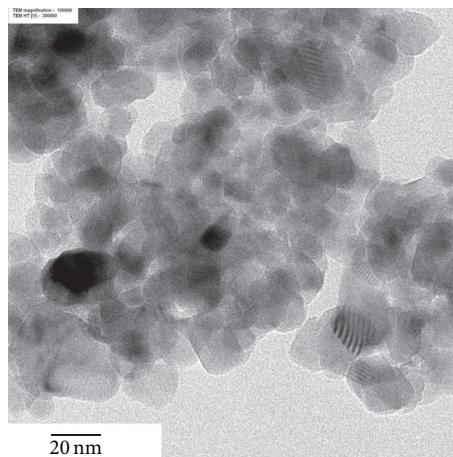


FIGURE 5: TEM micrograph of 1.0 mol% Au-loaded TiO_2 nanoparticles.

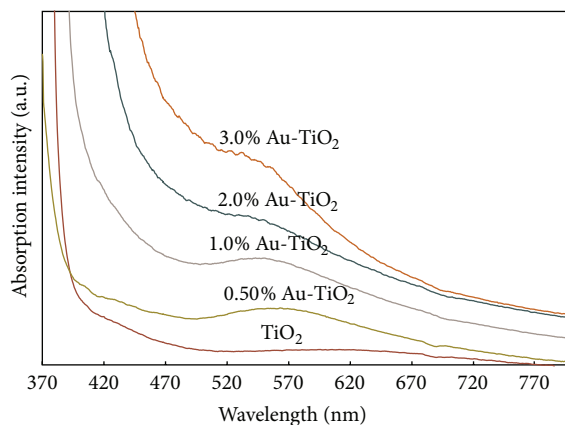
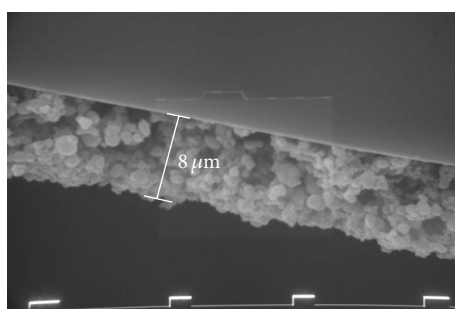
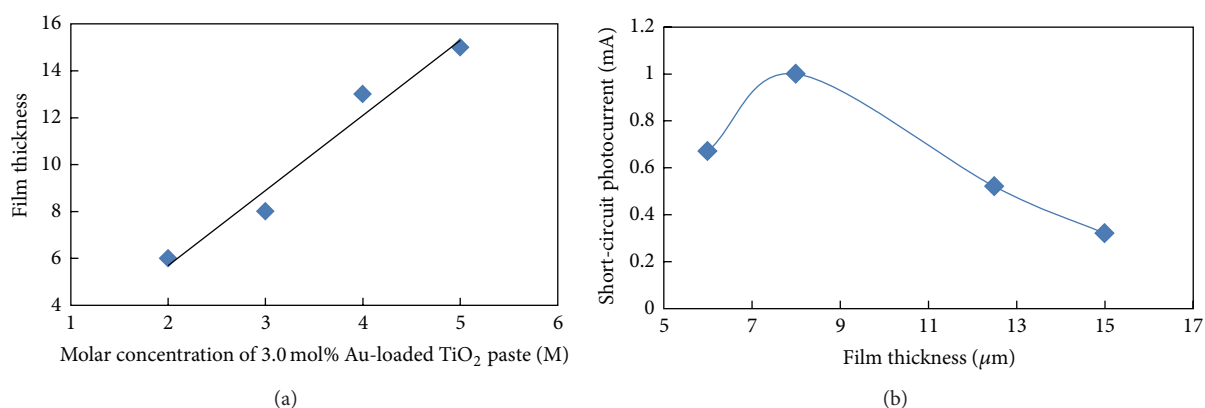


FIGURE 6: UV-vis absorption spectra of TiO_2 and 0.50–3.0 mol% Au-loaded TiO_2 films deposited on ITO substrate.



(c)

FIGURE 7: (a) Molar concentration of TiO_2 paste versus film thickness of 3.0 mol% Au- TiO_2 film. (b) Film thickness versus short-circuit photocurrent of 3.0 mol% Au- TiO_2 film. (c) SEM image of 3.0 mol% Au- TiO_2 film prepared by squeegee method with using 3 M TiO_2 paste.

3.2. Characterization and Optimization of Au-Loaded TiO_2 Films. Figure 6 shows the UV-vis absorption spectra of TiO_2 and 0.50–3.0 mol% Au-loaded TiO_2 films deposited on ITO substrate. A broad peak of Au appeared in the wavelength of 530–580 nm and increased intensity with increasing the Au loading amount on the TiO_2 nanoparticles. This result indicated that the localized surface plasmon resonance could be excited on Au-loaded TiO_2 nanoparticles [41]. As mentioned in the previously reported research by many groups,

the film thickness is one of the most important factor effects on the performance of DSSCs [42, 43]. The film thickness was optimized by varying the concentration of 3.0 mol% Au-loaded TiO_2 paste in the squeegee process. The thickness of 3.0% Au-loaded TiO_2 films was increased with increasing the concentration of Au-loaded TiO_2 paste, as shown in Figure 7(a). Figure 7(b) shows the effect of 3.0% Au-loaded TiO_2 film thickness on short-circuit photocurrent properties of DSSCs. It was found that the short-circuit

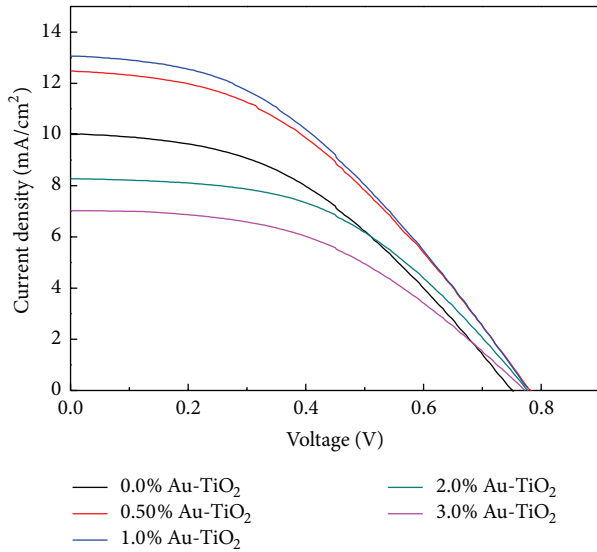


FIGURE 8: Current density versus voltage (J - V) curves of fabricated DSSCs using TiO_2 and 0.50–3.0 mol% Au-loaded TiO_2 nanoparticles.

TABLE 1: Photovoltaic performances of fabricated DSSCs using TiO_2 and 0.50–3.0 mol% Au-loaded TiO_2 nanoparticles.

	V_{oc} (V)	J_{sc} (mA/cm ²)	η (%)	FF
TiO_2	0.75	10.04	4.34	0.43
0.50 mol% Au- TiO_2	0.78	12.48	5.40	0.42
1.0 mol% Au- TiO_2	0.78	13.06	5.52	0.44
2.0 mol% Au- TiO_2	0.77	8.27	4.13	0.56
3.0 mol% Au- TiO_2	0.77	7.02	3.33	0.39

photocurrent increased with increasing film thickness up to $8 \mu\text{m}$ (Figure 7(c)). However, the photocurrent decreased with the film thickness more than $8 \mu\text{m}$.

3.3. Photovoltaic Properties of the Fabricated DSSCs Using TiO_2 and Au-Loaded TiO_2 Nanoparticles. Photovoltaic properties of the fabricated DSSCs using TiO_2 and different nominal 0.50–3.0 mol% of Au-loaded TiO_2 nanoparticles were studied to compare the enhancement of photovoltaic performance of DSSCs. Figure 8 shows current density versus voltage (J - V) curves of fabricated DSSCs using TiO_2 and 0.50–3.0 mol% Au-loaded TiO_2 nanoparticles. Photovoltaic performances were calculated from these J - V curves as shown in Table 1. The open circuit voltage (V_{oc}) is almost constant value with Au-loading amount. This indicates that the Au-loading to TiO_2 does not affect the Fermi level because the V_{oc} is originated from the energy difference between Fermi level of TiO_2 layer and the oxidation/reduction potential of the electrolyte [44]. The results show that the short-circuit current densities (J_{sc}) of the fabricated DSSCs with TiO_2 , 0.50, 1.0, 2.0, and 3.0 mol% Au-loaded TiO_2 nanoparticles were 10.04, 12.48, 13.06, 8.27, and 7.02 mA/cm², corresponding to the efficiency (η) of 4.34, 5.40, 5.52, 4.13, and 3.33%, respectively. These results confirmed that Au-loading could

enhance the performances of DSSCs with the loading amount up to 1.0 mol%. However, the short-circuit current density and the efficiency of the fabricated DSSCs were decreased upon the increasing amount of 2.0 mol% Au loading. These effects might be possibly due to the fact that the active site was shielded by the large amount of Au loading or rougher morphology of the Au-loaded TiO_2 layers.

4. Conclusion

In this research, the Au-loaded TiO_2 nanoparticles were successfully synthesized by the modified sol-gel method together with the impregnation method. Anatase phase of TiO_2 was obtained in all samples with an average particle size of 20 nm. The DSSC was improved by an effect of the Au-loaded titanium dioxide (Au-loaded TiO_2). For the enhancement of DSSCs, the fabricated cell with up to 1.0 mol% Au-loaded TiO_2 could enhance the performance by localized surface plasmon effect and scattering property.

Conflict of Interests

The authors declare that there is no conflict of interests regarding the publication of this paper.

Acknowledgments

This research was supported by a Grant-in-Aid for Young Scientists (B) (23760010) and Grant-in-Aid for Scientific Research (C) (25390051) from the Japan Society for the Promotion of Science (JSPS), the Thailand Research Fund, The Royal Golden Jubilee Ph.D. Program (PHD/0358/2551), the National Science and Technology Department Agency (NSTDA), Thailand Graduate Institute of Science and Technology (TGIST: TG-55-10-52-051 M), the National Nanotechnology Center (NANOTEC), NSTDA, Ministry of Science and Technology, through its program of Center of Excellence Network, Thailand, and the Department of Chemistry, Faculty of Science, Chiang Mai University, Chiang Mai, Thailand. Sukon Phanichphant wishes to thank the National Research University Project under Thailand's Office of the Higher Education Commission for financial support.

References

- [1] A. Fujishima, T. N. Rao, and D. A. Tryk, "Titanium dioxide photocatalysis," *Journal of Photochemistry and Photobiology C*, vol. 1, no. 1, pp. 1–21, 2000.
- [2] K. Pirkanniemi and M. Sillanpää, "Heterogeneous water phase catalysis as an environmental application: a review," *Chemosphere*, vol. 48, no. 10, pp. 1047–1060, 2002.
- [3] Y. Hu, H.-L. Tsai, and C.-L. Huang, "Effect of brookite phase on the anatase-rutile transition in titania nanoparticles," *Journal of the European Ceramic Society*, vol. 23, no. 5, pp. 691–696, 2003.
- [4] V. Samuel, R. Pasricha, and V. Ravi, "Synthesis of nanocrystalline rutile," *Ceramics International*, vol. 31, no. 4, pp. 555–557, 2005.

- [5] O. Carp, C. L. Huisman, and A. Keller, "Photoinduced reactivity of titanium dioxide," *Progress in Solid State Chemistry*, vol. 32, no. 1-2, pp. 33-177, 2004.
- [6] K. G. Deepa, P. Lekha, and S. Sindhu, "Efficiency enhancement in DSSC using metal nanoparticles: A Size Dependent Study," *Solar Energy*, vol. 86, no. 1, pp. 326-330, 2012.
- [7] H. A. Atwater and A. Polman, "Plasmonics for improved photovoltaic devices," *Nature Materials*, vol. 9, no. 3, pp. 205-213, 2010.
- [8] V. E. Ferry, J. N. Munday, and H. A. Atwater, "Design considerations for plasmonic photovoltaics," *Advanced Materials*, vol. 22, no. 43, pp. 4794-4808, 2010.
- [9] S. Muduli, O. Game, V. Dhas et al., "TiO₂-Au plasmonic nanocomposite for enhanced dye-sensitized solar cell (DSSC) performance," *Solar Energy*, vol. 86, no. 5, pp. 1428-1434, 2012.
- [10] G. Sahu, S. W. Gordon, and M. A. Tarr, "Synthesis and application of core-shell Au-TiO₂ nanowire photoanode materials for dye sensitized solar cells," *RSC Advances*, vol. 2, no. 2, pp. 573-582, 2012.
- [11] J. H. Lee and Y. S. Yang, "Effect of HCl concentration and reaction time on the change in the crystalline state of TiO₂ prepared from aqueous TiCl₄ solution by precipitation," *Journal of the European Ceramic Society*, vol. 25, no. 16, pp. 3573-3578, 2005.
- [12] A. Sandoval, A. Aguilar, C. Louis, A. Traverse, and R. Zanella, "Bimetallic Au-Ag/TiO₂ catalyst prepared by deposition-precipitation: high activity and stability in CO oxidation," *Journal of Catalysis*, vol. 281, no. 1, pp. 40-49, 2011.
- [13] H. Wang, P. Liu, X. Cheng, A. Shui, and L. Zeng, "Effect of surfactants on synthesis of TiO₂ nano-particles by homogeneous precipitation method," *Powder Technology*, vol. 188, no. 1, pp. 52-54, 2008.
- [14] S. S. Kalanur, S. H. Lee, Y. J. Hwang, and O. S. Joo, "Enhanced photoanode properties of CdS nanoparticle sensitized TiO₂ nanotube arrays by solvothermal synthesis," *Journal of Photochemistry and Photobiology A: Chemistry*, vol. 259, pp. 1-9, 2013.
- [15] M. Kang, S.-Y. Lee, C.-H. Chung et al., "Characterization of a TiO₂ photocatalyst synthesized by the solvothermal method and its catalytic performance for CHCl₃ decomposition," *Journal of Photochemistry and Photobiology A: Chemistry*, vol. 144, no. 2-3, pp. 185-191, 2001.
- [16] Y. Lee, J. Chae, and M. Kang, "Comparison of the photovoltaic efficiency on DSSC for nanometer sized TiO₂ using a conventional sol-gel and solvothermal methods," *Journal of Industrial and Engineering Chemistry*, vol. 16, no. 4, pp. 609-614, 2010.
- [17] Y. Zhang, H. Zheng, G. Liu, and V. Battaglia, "Synthesis and electrochemical studies of a layered spheric TiO₂ through low temperature solvothermal method," *Electrochimica Acta*, vol. 54, no. 16, pp. 4079-4083, 2009.
- [18] D. Crişan, N. Drăgan, M. Răileanu et al., "Structural study of sol-gel Au/TiO₂ films from nanopowders," *Applied Surface Science*, vol. 257, no. 9, pp. 4227-4231, 2011.
- [19] J. N. Hart, D. Menzies, Y.-B. Cheng, G. P. Simon, and L. Spiccia, "TiO₂ sol-gel blocking layers for dye-sensitized solar cells," *Comptes Rendus Chimie*, vol. 9, no. 5-6, pp. 622-626, 2006.
- [20] M. Hočevar, U. O. Krašovec, M. Bokalič et al., "Sol-gel based TiO₂ paste applied in screen-printed dye-sensitized solar cells and modules," *Journal of Industrial and Engineering Chemistry*, vol. 19, no. 5, pp. 1464-1469, 2013.
- [21] C. M. Malengreaux, A. Timmermans, S. L. Pirard et al., "Optimized deposition of TiO₂ thin films produced by a non-aqueous sol-gel method and quantification of their photocatalytic activity," *Chemical Engineering Journal*, vol. 195-196, pp. 347-358, 2012.
- [22] S. Šegota, L. Ćurković, D. Ljubas, V. Svetličić, I. F. Houra, and N. Tomašić, "Synthesis, characterization and photocatalytic properties of sol-gel TiO₂ films," *Ceramics International*, vol. 37, no. 4, pp. 1153-1160, 2011.
- [23] H. M. N. Bandara, R. M. G. Rajapakse, K. Murakami, G. R. R. A. Kumara, and G. Anuradha Sepalage, "Dye-sensitized solar cell based on optically transparent TiO₂ nanocrystalline electrode prepared by atomized spray pyrolysis technique," *Electrochimica Acta*, vol. 56, no. 25, pp. 9159-9161, 2011.
- [24] C. Jiang, W. L. Koh, M. Y. Leung, W. Hong, Y. Li, and J. Zhang, "Influences of alcoholic solvents on spray pyrolysis deposition of TiO₂ blocking layer films for solid-state dye-sensitized solar cells," *Journal of Solid State Chemistry*, vol. 198, pp. 197-202, 2013.
- [25] C. Jiang, M. Y. Leung, W. L. Koh, and Y. Li, "Influences of deposition and post-annealing temperatures on properties of TiO₂ blocking layer prepared by spray pyrolysis for solid-state dye-sensitized solar cells," *Thin Solid Films*, vol. 519, no. 22, pp. 7850-7854, 2011.
- [26] M. Okuya, K. Nakade, and S. Kaneko, "Porous TiO₂ thin films synthesized by a spray pyrolysis deposition (SPD) technique and their application to dye-sensitized solar cells," *Solar Energy Materials and Solar Cells*, vol. 70, no. 4, pp. 425-435, 2002.
- [27] J. N. Hart, R. Cervini, Y.-B. Cheng, G. P. Simon, and L. Spiccia, "Formation of anatase TiO₂ by microwave processing," *Solar Energy Materials and Solar Cells*, vol. 84, no. 1-4, pp. 135-143, 2004.
- [28] J. N. Hart, D. Menzies, Y.-B. Cheng, G. P. Simon, and L. Spiccia, "A comparison of microwave and conventional heat treatments of nanocrystalline TiO₂," *Solar Energy Materials and Solar Cells*, vol. 91, no. 1, pp. 6-16, 2007.
- [29] S. Uchida, M. Tomiha, N. Masaki, A. Miyazawa, and H. Takizawa, "Preparation of TiO₂ nanocrystalline electrode for dye-sensitized solar cells by 28 GHz microwave irradiation," *Solar Energy Materials and Solar Cells*, vol. 81, no. 1, pp. 135-139, 2004.
- [30] N. Wetchakun, B. Incessungvorn, K. Wetchakun, and S. Phanichphant, "Influence of calcination temperature on anatase to rutile phase transformation in TiO₂ nanoparticles synthesized by the modified sol-gel method," *Materials Letters*, vol. 82, pp. 195-198, 2012.
- [31] N. Wetchakun and S. Phanichphant, "Effect of temperature on the degree of anatase-rutile transformation in titanium dioxide nanoparticles synthesized by the modified sol-gel method," *Current Applied Physics*, vol. 8, no. 3-4, pp. 343-346, 2008.
- [32] C. Suresh, V. Biju, P. Mukundan, and K. G. K. Warriar, "Anatase to rutile transformation in sol-gel titania by modification of precursor," *Polyhedron*, vol. 17, no. 18, pp. 3131-3135, 1998.
- [33] Q. Zhang, L. Gao, and J. Guo, "Effect of hydrolysis conditions on morphology and crystallization of nanosized TiO₂ powder," *Journal of the European Ceramic Society*, vol. 20, no. 12, pp. 2153-2158, 2000.
- [34] T. Sugimoto and X. Zhou, "Synthesis of uniform anatase TiO₂ nanoparticles by the gel-sol method. 2. Adsorption of OH⁻ ions to Ti(OH)₄ gel and TiO₂ particles," *Journal of Colloid and Interface Science*, vol. 252, no. 2, pp. 347-353, 2002.

- [35] D. Bahnemann, "Photocatalytic water treatment: solar energy applications," *Solar Energy*, vol. 77, no. 5, pp. 445–459, 2004.
- [36] M. Harada, T. Sasaki, Y. Ebina, and M. Watanabe, "Preparation and characterizations of Fe- or Ni-substituted titania nanosheets as photocatalysts," *Journal of Photochemistry and Photobiology A: Chemistry*, vol. 148, no. 1–3, pp. 273–276, 2002.
- [37] M. Romero, J. Blanco, B. Sánchez et al., "Solar photocatalytic degradation of water and air pollutants: challenges and perspectives," *Solar Energy*, vol. 66, no. 2, pp. 169–182, 1999.
- [38] M. Pan, N. Huang, X. Zhao, J. Fu, and X. Zhong, "Enhanced efficiency of dye-sensitized solar cell by high surface area anatase-TiO₂-modified P25 paste," *Journal of Nanomaterials*, vol. 2013, pp. 1–6, 2013.
- [39] G. Dai, L. Zhao, S. Wang et al., "Double-layer composite film based on sponge-like TiO₂ and P25 as photoelectrode for enhanced efficiency in dye-sensitized solar cells," *Journal of Alloys and Compounds*, vol. 539, pp. 264–270, 2012.
- [40] V. Dhas, S. Muduli, S. Agarkar et al., "Enhanced DSSC performance with high surface area thin anatase TiO₂ nanoleaves," *Solar Energy*, vol. 85, no. 6, pp. 1213–1219, 2011.
- [41] I.-K. Ding, J. Zhu, W. Cai et al., "Plasmonic Dye-sensitized solar cells," *Advanced Energy Materials*, vol. 1, no. 1, pp. 52–57, 2011.
- [42] C.-Y. Huang, Y.-C. Hsu, J.-G. Chen, V. Suryanarayanan, K.-M. Lee, and K.-C. Ho, "The effects of hydrothermal temperature and thickness of TiO₂ film on the performance of a dye-sensitized solar cell," *Solar Energy Materials and Solar Cells*, vol. 90, no. 15, pp. 2391–2397, 2006.
- [43] M. C. Kao, H. Z. Chen, S. L. Young, C. Y. Kung, and C. C. Lin, "The effects of the thickness of TiO₂ films on the performance of dye-sensitized solar cells," *Thin Solid Films*, vol. 517, no. 17, pp. 5096–5099, 2009.
- [44] M. Ghaffari, M. B. Cosar, H. I. Yavuz, M. Ozenbas, and A. K. Okyay, "Effect of Au nano-particles on TiO₂ nanorod electrode in dye-sensitized solar cells," *Electrochimica Acta*, vol. 76, pp. 446–452, 2012.

Research Article

A Reuse Evaluation for Solar-Cell Silicon Wafers via Shift Revolution and Tool Rotation Using Magnetic Assistance in Ultrasonic Electrochemical Micromachining

P. S. Pa

Department of Digital Content Design, Graduate School of Toy and Game Design, National Taipei University of Education, No. 134, Sector 2, Heping E. Road, Taipei City 106, Taiwan

Correspondence should be addressed to P. S. Pa; myhow@tea.ntue.edu.tw

Received 19 September 2013; Revised 23 November 2013; Accepted 27 November 2013

Academic Editor: Liang-Sheng Liao

Copyright © 2013 P. S. Pa. This is an open access article distributed under the Creative Commons Attribution License, which permits unrestricted use, distribution, and reproduction in any medium, provided the original work is properly cited.

A new reuse fabrication using a tool module with rotation and revolution through a process of magnetic assistance in ultrasonic electrochemical micromachining (UEMM) for removal of the surface layers from silicon wafers of solar cells is demonstrated. The target of the proposed reuse fabrication method is to replace the current approach, which uses strong acid and grinding and may damage the physical structure of silicon wafers and pollute to the environment. A precisely engineered clean production approach to removal of surface microstructure layers from silicon wafers is to develop a mass production system for recycling defective or discarded silicon wafers of solar cells that can reduce pollution and cost. The high revolution speed of the shift with the high rotation speed of the designed tool increases the discharge mobility and improves the removal effect associated with the high feed rate of the workpiece. High frequency and high power of ultrasonic with large electrolyte flow rate and high magnetic strengths with a small distance between the two magnets provide a large discharge effect and good removal; only a short period of time is required to remove the epoxy film and Si_3N_4 layer easily and cleanly.

1. Introduction

The success of solar-cell technology that allows the conversion of solar energy directly into electric powers represents an important milestone for the energy industry worldwide [1, 2]. In view of energy shortages, the need for environmental protection, and a predicted future lack of silicon material, the research and application of solar optoelectronics have become globally significant. In addition to its great potential for development, solar energy also has the advantages of abundance, accessibility, and that of causing less pollution than the alternatives. The solar optoelectronic industry is becoming increasingly important and it is expected that solar energy will replace petroleum as the most important source of energy in the foreseeable future [3]. Production of photovoltaic modules on a commercial scale dates back to 1980s. Photovoltaics (PV) module manufacturers provide a work warranty of 20–30 years, so modules produced back

in the 1980s should be put out of commission and recycled during this decade, while modules manufactured in 2000 should be recycled by 2030. In recent years, photovoltaic power generation systems have been gaining unprecedented attention as an environmentally beneficial method to solve the energy problem. From the economic point of view, the pure silicon, which can be recapture from the used cells, is the most important material due to its cost and shortage. Ewa et al. selected methods of used or damaged module and cells recycling and experimental results are presented. Advantages and disadvantages of the techniques are described, what could be helpful during the optimization of the method. The recycling process of PV module consists of two main steps: separation of cells and its refining. During the first step, cells are separated due to the thermal or chemical methods usage. Separation of cells from damaged PV modules through chemical treatment is not economically worthwhile; a far more better solution is to use thermal treatment. Next, the

separated cells are refining. During this process, useless layers are removed. The implementation of laser techniques in unwanted layer removal stage, in comparison with chemical treatment, is also disadvantageous. An optimal solution is to use thermal treatment for cell separation and chemical treatment for removing the metallization, contacts, antireflective coating, and the n-p junction [4–6].

Electromagnetic metal forming (EMF) is an example of a high-speed formation process that is determined by the dynamics of a coupled electromagnetic-mechanical system. “Magnetic” pressure provides the necessary kinetic energy. A magnetic pulse accelerates the workpiece up to a certain velocity (such as 200–300 m/s) and the material is driven into the die, causing forming by impact [7, 8]. Other applications include embossing, blanking, and drawing. Magnetic deburring has also been used for holes drilled into tubes. The results showed that burrs inside pipes could be removed using a magnetic process and the height of the burr could be successfully decreased from 163 μm to 1 μm . This magnetic deburring can be effectively used inside long tubes [9]. The formulation of a thermomagneto mechanism is used to simulate electromagnetic sheet metal forming processes (EMF). In this process, deformation of the workpiece is achieved by the interaction of a current generated in the workpiece by a magnetic field from a coil adjacent to the workpiece. For authentic industrial applications, however, the modeling of three-dimensional formation operations becomes crucial for an effective process design. The implementation of such a 3D model still represents work in progress. Results shown in the study are restricted to the axisymmetric case [10]. Ultrasonics has played an important role in industry since 1927 [11]. Conventional ultrasonic machining (USM) uses an abrasive slurry and a vibrating tool (typically 10–15 μm in amplitude and 15–30 kHz in frequency). The abrasives are mobilized by the vibrating tool to cut the material. Ultrasonics have also been widely applied in welding, metallurgy, cleaning, measurement, and communications [12]. Ceramic and composite materials can be machined using ultrasonics [13]. Gilmore compares various nontraditional machining methods for machining ceramics, including grinding, ultrasonics, electrical discharge machining, laser beam machining, and water jet machining. Gilmore found that ultrasonic machining has distinct advantages over other machining methods [14]. Electrochemical machining (ECM) involves the use of corrosive chemical solutions to etch the surface of a workpiece. This approach is beneficial for avoiding deformation and deformed edges and is also applicable to brittle materials. The device and operational costs are low and design changes are less expensive. Related applications can be seen in industry such as chemical blanking, milling, and engraving [15].

Electrochemical machining (ECM) involves the connection of a workpiece between the anode of a DC power supply and a cathode. An electrolyte between the anode workpiece and the cathode causes part of the workpiece to be dissolved in an electrochemical (ECM) reaction [16]. The main difficulty in the implementation of ECM lies in the design of the electrode owing to the complex process of metal removal [17]. Previous studies show that the size of the gap between the electrode and the workpiece directly affects

the current conditions and the electrolyte dregs discharge [18]. The ECM process is still underutilized owing to a lack of understanding of the mechanism of metal removal and difficulties involved in tool design. Even for simple cases, it is not possible to accurately predict work profiles [19]. A wide range of different types of electrode have also been developed for electropolishing [20–24].

Silicon wafers are the key material for transistors in integrated circuits and are the main component in microprocessors, computer memory, and almost every electronic device in use today. At present the greatest challenge facing the solar-energy industry is material shortage. In view of this, it is necessary to develop a novel and more effective recycling technology for silicon wafer manufacturers to improve their competitiveness. Currently a proportion of used wafers are recycled and refurbished to reduce manufacturing costs and waste because recycled wafers cost less than half that of new ones. However, the most common recycling process involves abrasion, etching, polishing, and cleaning in which part of the surface layer of the wafer is removed. An alternative approach, that is faster and cheaper than the usual Chemical & Mechanical Planarization (CMP), is to etch the wafers with a hydrofluoric acid (HF) solution [25, 26]. This study introduces a newly designed tool that rotates on two axes in a process that combines ultrasonic electrochemical micromachining (UEMM) with magnetic assistance for the removal of the hybrid composites coatings from the surface of solar-cell silicon wafers. A clean manufacturing approach for the removal of defective surface films is offered. This is a low polluting recycling process that is suitable for the mass production of solar-cell silicon wafers from recovered or defective items. The object of this study is the demonstration of this recycling system as a replacement of the usual methods that use strong acids and abrasion that can damage the silicon wafers and are certainly harmful to the environment. The proposed system allows defective solar-cell wafers from the production line, as well as used ones, to be recycled and returned to production. This process will lower costs, raise efficiency, and reduce pollution without loss of silicon (because no abrasion is involved) and the recycled wafers can be returned to the production line.

2. Specifications for Solar Cell Silicon Wafer Recycling [25, 27]

2.1. Engineering Specifications

- (a) To successfully remove the defective surface layer from solar cell silicon wafers, the recycled silicon wafers shall retain no metal elements or residue on the surface and should be acceptable for return to production.
- (b) For in-house recycling lines, optional etching of defective films on solar cell silicon wafers enables recycled silicon wafers with no metal elements or residue on the surface to be obtained. They are then acceptable for return to production.

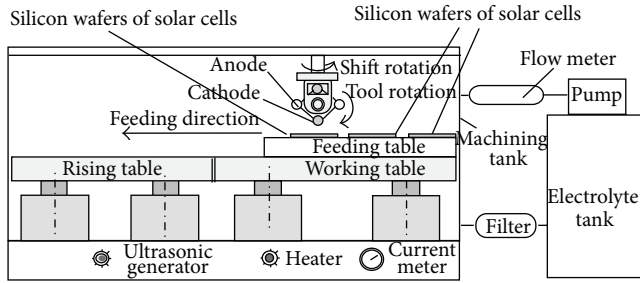


FIGURE 1: Experimental setup of recycling system for solar-cell silicon wafers.

2.2. Commercial Specifications

- Green manufacturing based on the recycling of defective items to reduce the waste of solar-cell silicon wafers is to be introduced and used by the leading wafer manufacturers in Taiwan and other countries.
- The goal of the project is to establish a mechanical module for the recycling of solar-cell silicon wafers that is applicable to the equipment, processing and manufacturing technologies to facilitate the introduction of these services to Taiwanese and foreign manufacturers and to build recycling lines that meet the needs of the manufacturers.

2.3. Technical Specifications

- The defective film on solar cell silicon wafers is partially or entirely removed to reduce manufacturing costs.
- The customized recycling lines shall meet the manufacturers' needs for the recycling of defective wafers. In addition, the recycling lines shall help reduce cost and conserve material while providing complete recycling and reducing pollution.

3. Design Process

This study applies to microstructure removal (μm). The experimental setup is shown in Figure 1 and was derived by design analyses. This was taken as a basis for the development of a process combining microelectroetching and ECM of solar-cell silicon wafers to remove the defective thin film from the surface of the wafers. Conventional 6" solar-cell silicon wafers were used in these experiments.

4. Experimental Setup and Parameters

The workpieces used were solar-cell silicon wafers 6" in diameter and 0.2 mm thick and were immersed in electrolyte in the tank for the recycling process. The equipment used for the precision removal of the composite epoxy and Si_3N_4 layers using magnetic assistance in ultrasonic electrochemical micromachining (UEMM) included two magnets,

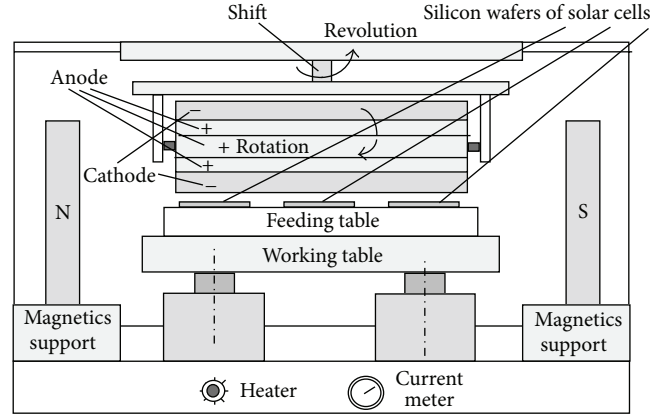


FIGURE 2: Configuration of the magnetic assistance mechanism.

an ultrasonic generator, a DC power supply, a heater, a pump, a flow meter, an electrolyte tank, and a filter. The experimental setup of the recycling system is schematically illustrated in Figure 1. The configuration of the magnetic-assistance mechanism is shown in Figure 2. The configuration of tool module with rotation and revolution (shift) is shown in Figure 3(a). The configuration of the newly designed tool and workpiece (solar-cell silicon wafers) is shown in Figure 3(b). During the current experiment, the tool was supplied with continuous DC. The process removed $8\ \mu\text{m}$ of epoxy film and $0.2\ \mu\text{m}$ of Si_3N_4 from the surface of the silicon wafers. The electrolyte used was 15% wt NaNO_3 and 5% wt PO4-3-P phosphoric acid. The temperature of the electrolyte was 60°C . The continuous DC current (I) was 150 A and the voltages (E) used were 40, 60, 80, or 100 V. The feed rate of the workpiece (solar-cell silicon wafers) ranged from 50 to 500 mm/min. The noncontact distance (y) from the anode to the epoxy film surface was 6, 7, 8, 9, or 10 mm. The combination of frequency, ultrasonic power, and flow rate of the electrolyte used was (50 kHz/50 W, 10 L/min), (50 kHz/100 W, 20 L/min), (100 kHz/100 W, 30 L/min), and (100 kHz/150 W, 40 L/min). The combination of magnetic strength (magnetic field intensity) and the distances between the two magnets was (1000 Gauss, 1000 mm), (2000 Gauss, 1200 mm), (3000 Gauss, 1400 mm), and (4000 Gauss, 1600 mm). The combination of tool revolution (shift) and tool rotational speeds used was (200 rpm, 300 rpm), (400 rpm, 500 rpm), (600 rpm, 700 rpm), and (800 rpm, 900 rpm). The combination of the anode radius (r_a) and the cathode radius (r_c) was (10 mm, 10 mm), (15 mm, 15 mm), (20 mm, 20 mm), and (25 mm, 25 mm). The diameter (D_c) of the cathode was 74 mm (with a 4 mm gap between anode and cathode), 72 mm (with a 5 mm gap between anode and cathode), 70 mm (with a 6 mm gap between anode and cathode), or 68 mm (with a 7 mm gap between anode and cathode). All workpieces were cleaned in water after the recycling process and dried in air. The thickness of epoxy and Si_3N_4 nanostructures removed was determined by measurements made at more than two locations on the wafer using a NanoSpec Film Thickness Measurement System (Nanospec Film Analyzer 3000).

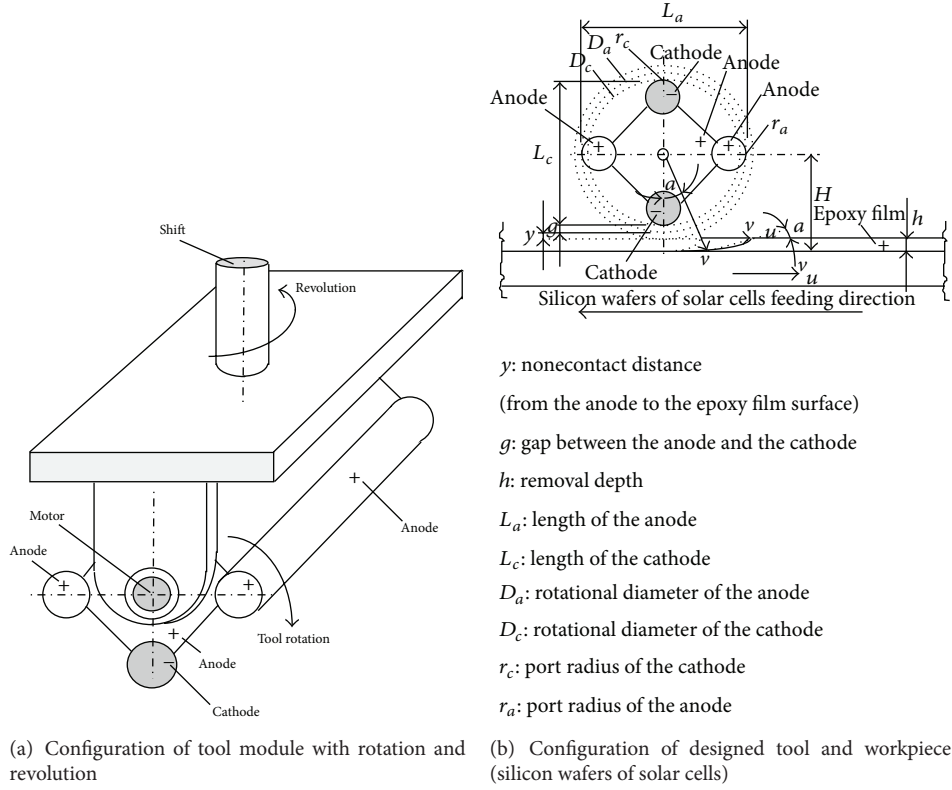


FIGURE 3: Geometry of the designed tool.

5. Results and Discussion

Figure 4 shows a high removal rate for the composite layers of silicon nitride (Si_3N_4) and epoxy using different combinations of frequency, ultrasonic power, and flow rate of the electrolyte. It can clearly be seen that the effect of ultrasonics on the electrochemical micromachining process (UEMM) is to improve the removal rate. The higher the frequency/power or electrolyte flow rate, the better the removal effect. The reason could be that the ultrasonic vibration energy and a high electrolyte flow rate facilitates the discharge of dregs from the tight machining gap.

Figure 5 shows the results of a test of different combinations of magnetic strength (magnetic field intensity) and the distance between the two magnets. The results show that the combination of high magnetic strength and short distance between the two magnets corresponds to a higher removal rate of the composite layers of epoxy and silicon nitride (Si_3N_4). It is also likely that the high intensity magnetic field facilitates dregs discharge. A combination of high magnetic field strength and small distance also allows a higher workpiece feed rate with a resultant reduction of machining time and cost.

As shown in Figure 6 an appropriate workpiece (solar-cell silicon wafer) feed rate and a sufficient current flow ensure that the composite layers of epoxy and Si_3N_4 are completely removed. A high feed rate reduces the power transmission efficiency per unit area of wafer surface, while a lower rate increases it. In a case where the feed rate is high, it may

be that there is insufficient electrolytic power for complete removal of the layers. But if the feed rate is too low this will increase processing time and also result in higher costs. The experimental results show that, for effective and complete removal of the epoxy and silicon nitride layers from the wafers, several combinations of settings for feed rate and continuous DC voltage have been found to give optimum results: 40 V with 300 mm/min, 60 V with 325 mm/min, 80 V with 350 mm/min, and 100 V with 375 mm/min.

According to the formula for the theoretical removal rate of a pure metal derived from Faraday's Law [16, 26],

$$W = \frac{ITM}{Fn}, \quad (1)$$

where I is the current, T is the time, and F is the Faraday constant.

From Figure 4, for an alloy, let $R = W/AT$ and $\omega = R/\rho$; then

$$\Delta X = \frac{E\sigma\Delta t}{\rho F(n/M)X},$$

$$\frac{E\sigma}{\rho Fn} = C,$$

$$\Delta X = \frac{C\Delta t}{X},$$

$$XdX = Cdt,$$

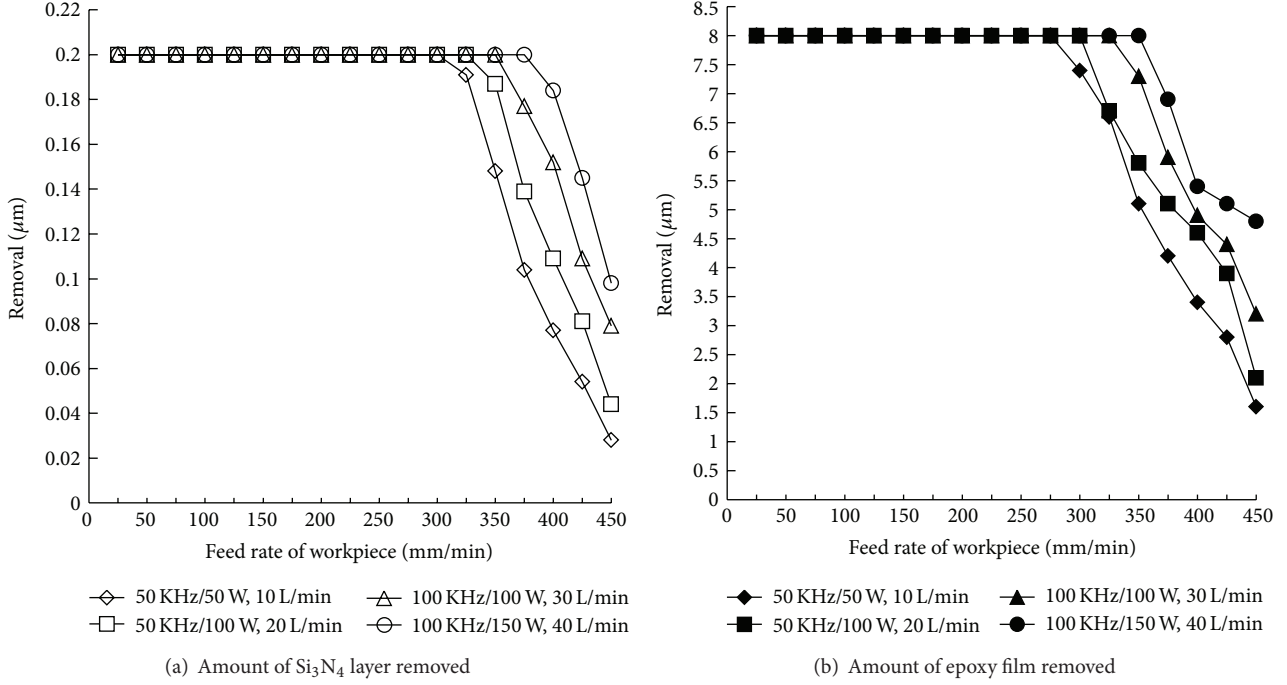


FIGURE 4: Amount of Si₃N₄ layer and epoxy film removed using different combinations of frequency, ultrasonic power, and electrolyte flow rate (phosphoric acid, NaNO₃ 15% wt, PO₄-3-P 5% wt, 60°C, continuous DC, 150 A, 80 V, 4000 Gauss, shift 800 rpm, and tool 900 rpm).

$$\int_{g+y}^{g+y+h} X dX = \int_0^t C dt,$$

$$[g+y+h]^2 - (g+y)^2 = \frac{2ET\sigma}{\rho F(n/M)},$$

$$[g+y+h] = \left[\frac{2ET\sigma}{\rho F(n/M)} + (g+y)^2 \right]^{1/2},$$

$$h = \left[\frac{2ET\sigma}{\rho F(n/M)} + (g+y)^2 \right]^{1/2} - (g+y). \quad (2)$$

From Figure 4, for an alloy,

$$h = \left[\frac{2ET\sigma}{\rho F((n_A/M_A)a_A + (n_B/M_B)a_B + \dots)} + (g+y)^2 \right]^{1/2} - (g+y),$$

$$h = \left[\frac{2T(I/A)(g+y)}{\rho F((n_A/M_A)a_A + (n_B/M_B)a_B + \dots)} + (g+y)^2 \right]^{1/2} - (g+y),$$

$$= \left\{ (g+y) \left[\frac{2TI_A}{\rho F((n_A/M_A)a_A + (n_B/M_B)a_B + \dots)} + (g+y) \right] \right\}^{1/2} - (g+y), \quad (3)$$

where n_i is the atomic number, a_i is the proportion of composition, M_i is the atomic mass, A is the electrochemical etching area, ρ is the density of the workpiece, E is the voltage across the gap, σ is the reciprocal resistance of the electrolyte, and ω is the etching rate in the longitudinal direction. From the above equations, the theoretical feed rate of the workpiece for a given material can be calculated.

From Figure 4,

$$H = \frac{L_c}{2} + (g+y) + h, \quad (4)$$

where g is the width of the gap between the circular-rhombus tool and the surface of the solar-cell silicon wafer, D_c is the length of the major axis of the cathode, and h is the microelectroetching removal depth:

$$\cos \alpha = \frac{H-h}{H} = \frac{(L_c/2) + (g+y)}{(L_c/2) + (g+y) + h}, \quad (5)$$

$$\omega \csc \alpha = \omega_0.$$

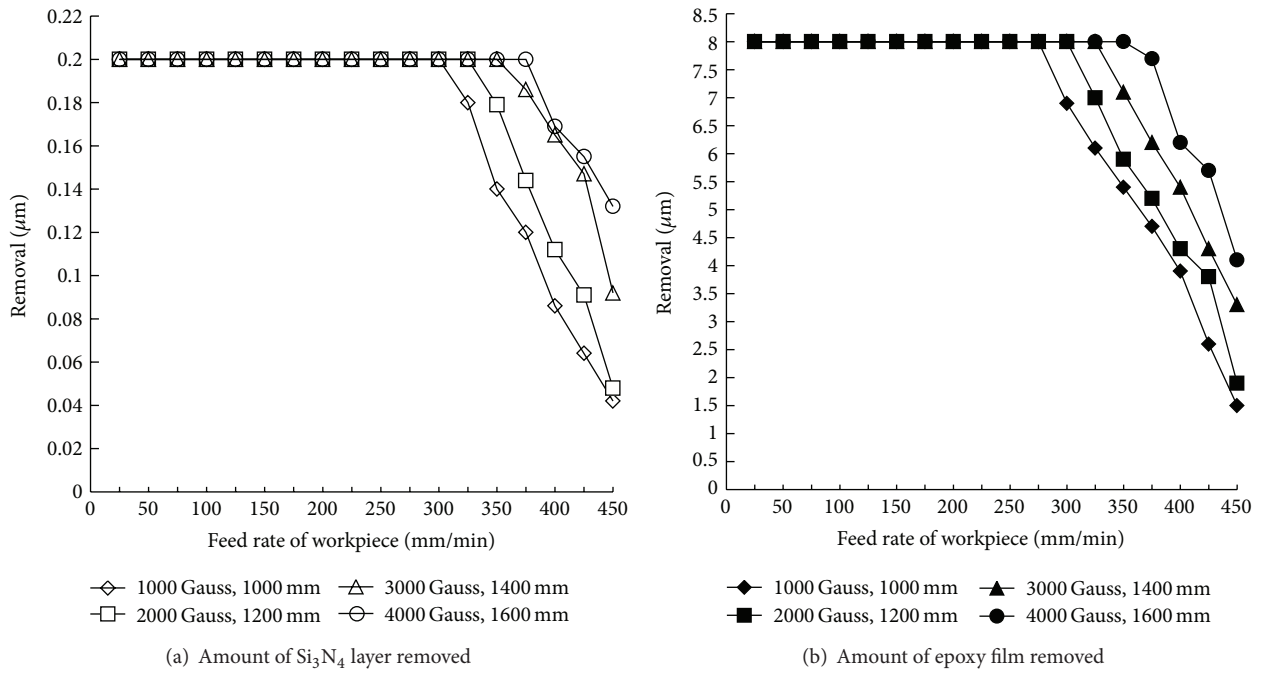


FIGURE 5: Amount of Si_3N_4 layer and epoxy film removed using different combinations of magnetic field strength and distance between the two magnets (phosphoric acid 25% wt, NaNO_3 15% wt, $\text{PO}_4\text{-3-P}$ 5% wt, 60°C , 40 L/min, continuous DC, 150 A, 80 V, 100 kHz/150 W, shift 800 rpm, and tool 900 rpm).

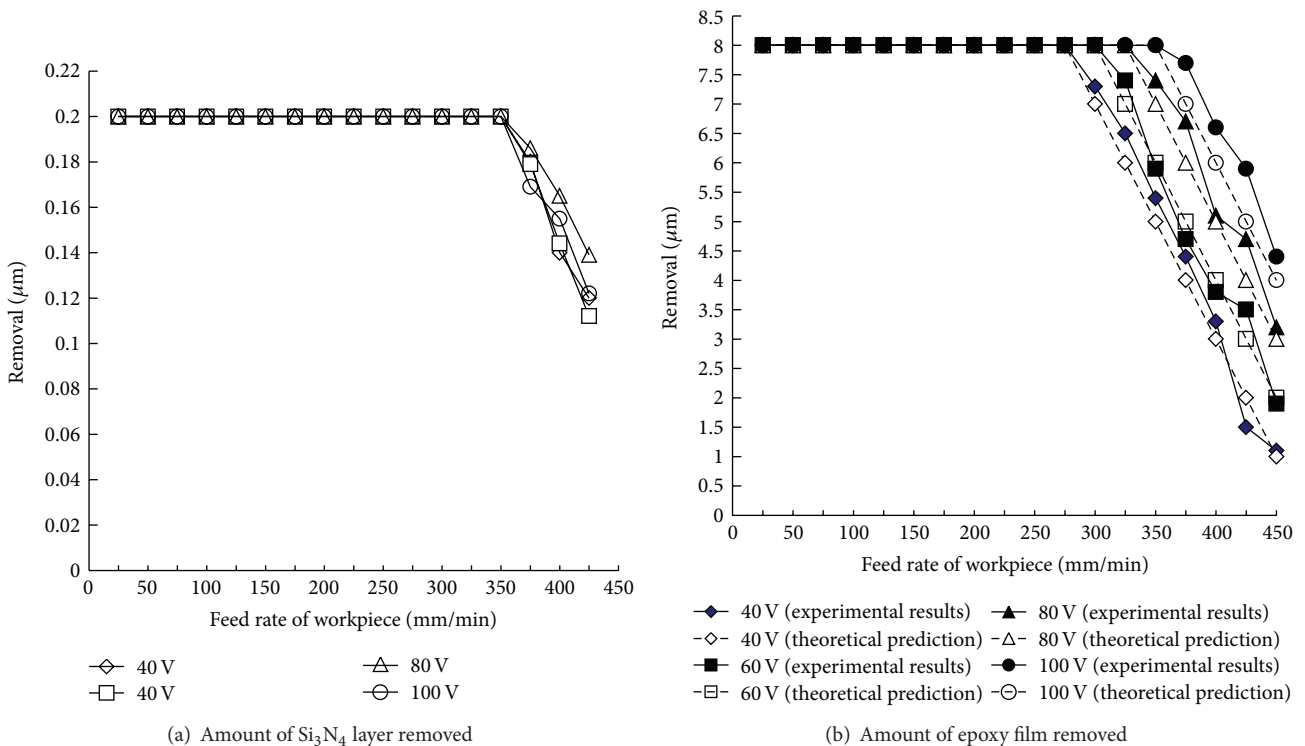


FIGURE 6: Amount of Si_3N_4 layer and epoxy film removed at different workpiece feed rates using different currents (phosphoric acid 25% wt, NaNO_3 15% wt, $\text{PO}_4\text{-3-P}$ 5% wt, 60°C , 40 L/min, continuous DC, 150 A, 100 kHz/150 W, 4000 Gauss, shift 800 rpm, and tool 900 rpm).

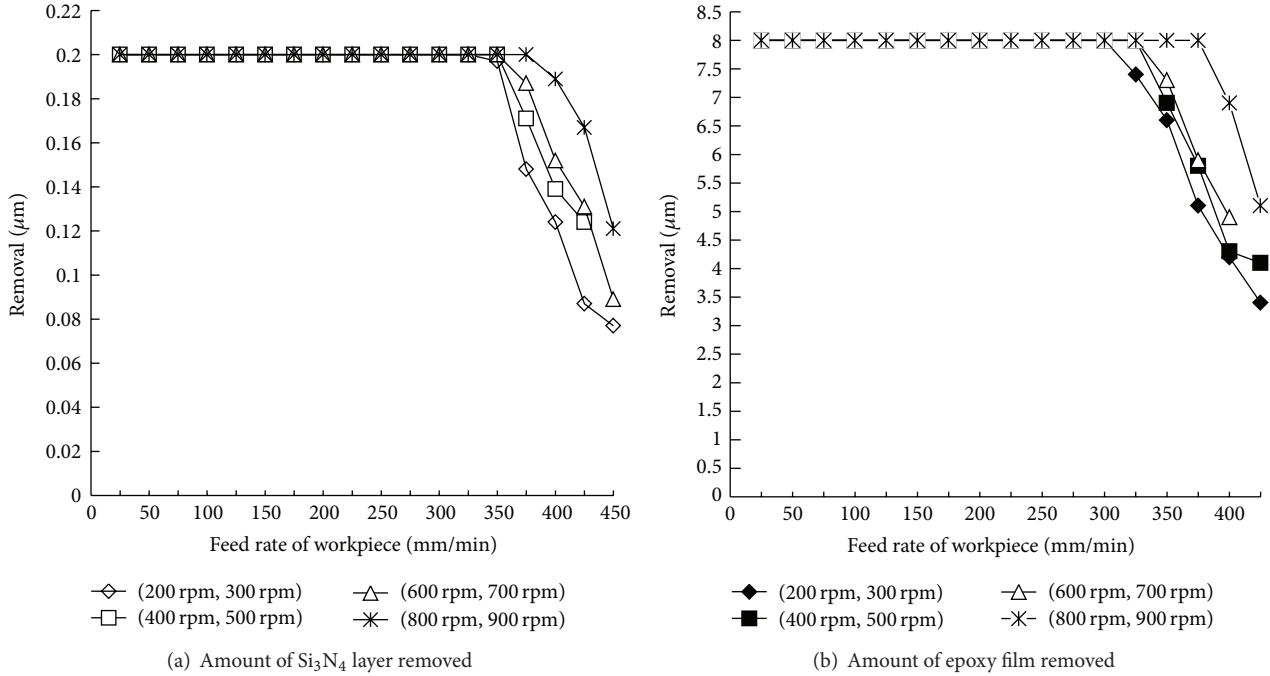


FIGURE 7: Amount of Si_3N_4 layer and epoxy film removed at different feed rates of workpiece using different combinations of tool revolution speed (shift) and tool rotational speed (phosphoric acid 25% wt, NaNO_3 15% wt, PO4-3-P 5% wt, 60°C, 40 L/min, continuous DC, 150 A, 100 kHz/150 W, and 4000 Gauss).

Squaring and simplifying (5),

$$h = \frac{[L_c + 2(g + y)] \omega^2}{4(\omega_v^2 - \omega^2)}, \quad (6)$$

where ω_v is the feed rate of the workpiece and ω is the removal rate in the longitudinal direction. From (6),

$$h = \left(\frac{L_c + 2(g + y)}{(g + y)^2} \right) \times \left[\frac{E\sigma}{F\rho((n_A/M_A)a_A + (n_B/M_B)a_B + \dots)} \right]^2 \times \left(4\omega_v^2 - \frac{4}{(g + y)^2} \right) \times \left[\frac{E\sigma}{F\rho((n_A/M_A)a_A + (n_B/M_B)a_B + \dots)} \right]^2)^{-1}. \quad (7)$$

From (7) it can be seen that the experimental results agree with the theoretical prediction (see Figure 6(b)). The experimental results show that the removal amount is directly proportional to the DC electric voltage (E) and is inversely proportional to the feed rate of the workpiece (ω_v), which agrees with the theoretical prediction (see Figure 6(b)).

Figure 7 shows that the combination of high speed revolution (shift) with high speed rotation of the tool increases the

discharge mobility and improves the removal effect required for a high feed rate of the workpiece. The high revolution (shift) speed and the higher rotational speed provide more kinetic energy to the electrolyte for dregs discharge and produce a better electrochemical micromachining and removal effect. In this system the ultrasonic vibration, electromagnetic forces, the higher revolution (shift), and rotational speeds combine to produce an efficient and complete discharge of the dregs.

Figure 8 shows the effects of the combination of the anode radius (r_a) and cathode radius (r_c) on the removal process. Decreasing these radii results in more open space which in turn reduces the resistance to dregs discharge and results in a more effective flushing path along the features of the tool and the silicon wafer surface and consequently also reduces the time required for removal of a given amount of epoxy and Si_3N_4 thin film.

Figure 9 shows the effects of different diameters (D_c) of cathode on the removal process. Figure 9(a) shows that a small diameter (D_c) cathode and a large gap between the cathode and the silicon wafer surface reduce the time taken for the removal process. Once again it can be demonstrated that the electrochemical reaction products (dregs) are more easily discharged from a large machining gap. The results in Figure 9(b) illustrate that a large diameter (D_c) cathode and a small gap between the cathode and the silicon wafer surface reduce the time required for removal of a given amount of epoxy nanostructure since the microelectroetching effect is more easily developed with an adequate supply of electrochemical power. The experimental results show that small

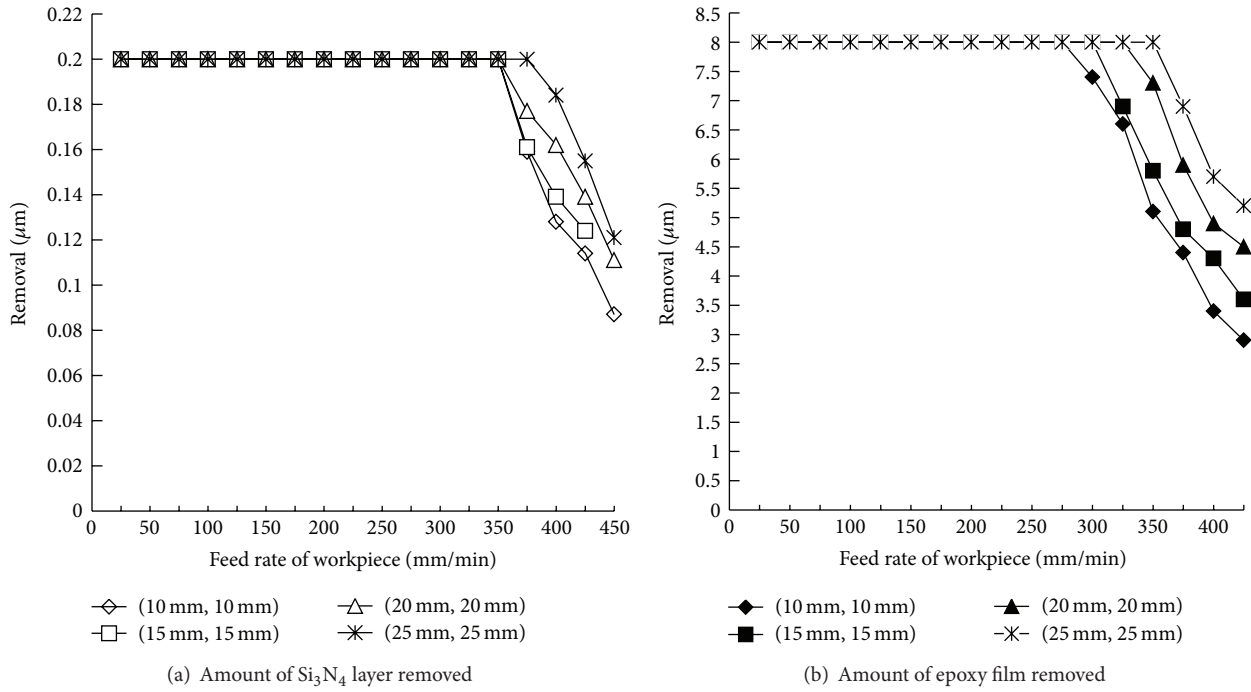


FIGURE 8: Amount of Si_3N_4 layer and epoxy film removed at different workpiece feed rates using different combinations of anode radius (r_a) and cathode radius (r_c) (phosphoric acid 25% wt, NaNO_3 15% wt, PO4-3-P 5% wt, 60°C, 40 L/min, continuous DC, 150 A, 100 kHz/150 W, 4000 Gauss, shift 800 rpm, and tool 900 rpm).

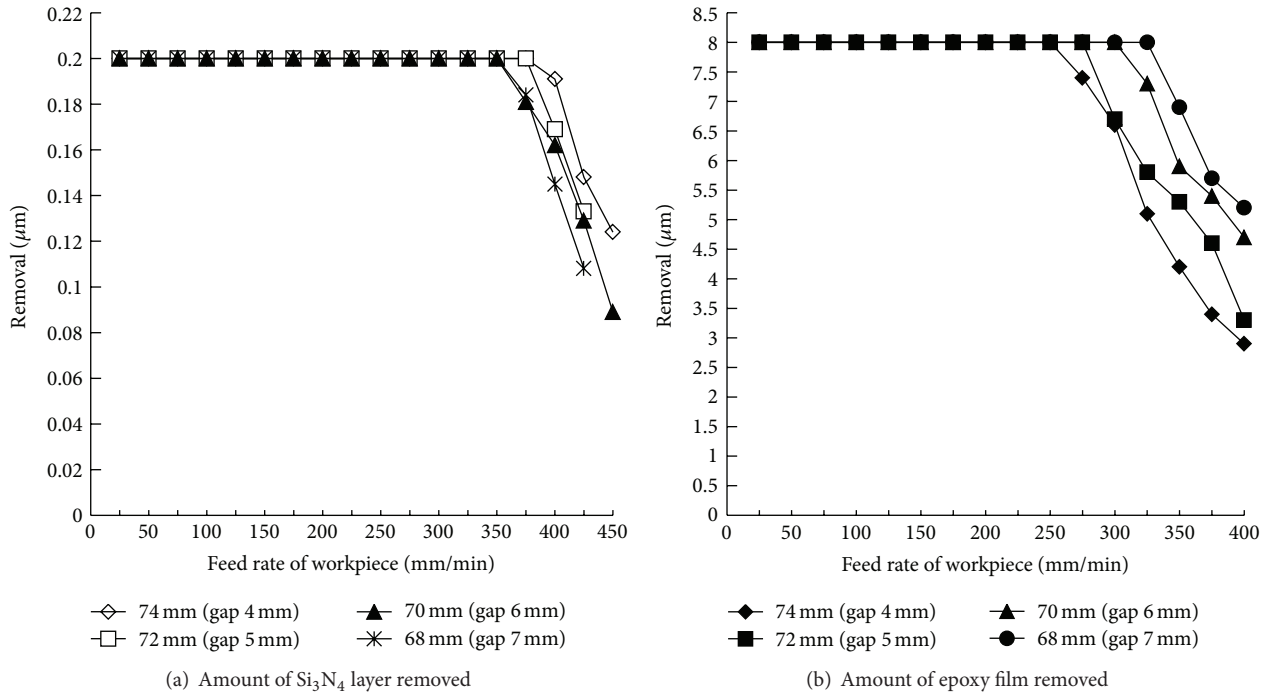


FIGURE 9: Amount of Si_3N_4 layer and epoxy film removed at different feed rates of workpiece using different diameters (D_c) of cathode and different sizes of gap between the anode and cathode (phosphoric acid 25% wt, NaNO_3 15% wt, PO4-3-P 5% wt, 60°C, 40 L/min, continuous DC, 150 A, 100 kHz/150 W, 4000 Gauss, shift 800 rpm, and tool 900 rpm).

gaps (4 mm) combined with a high continuous DC voltage and a high workpiece feed rate reduce microelectroetching time. However, discharge of the dregs from a small gap is difficult. To ensure stable operation of a microelectroetching and ECM process, a gap of 5 mm was found to be optimal.

In the current study, (7) can also be used to explain how controlling the stable reciprocal resistance (σ) can improve the finishing effect. Increased discharge mobility (shift revolution, tool rotation, ultrasonic vibration, magnetic force, etc.), guiding discharge transport, and the provision of a clear flushing path will establish reciprocal resistance (σ) stability. High speed revolution (shift) and rotation of the newly designed tool; high frequency and high power ultrasonics and a high rate of electrolyte flow; high magnetic field strength from magnets that are close together; and small anode and cathode radii all lead to better removal of the epoxy film and Si_3N_4 layers.

6. Conclusions

The newly designed tool and process achieve the precise recycling of solar-cell silicon wafers by removing the hybrid composites coatings of epoxy and silicon nitride Si_3N_4 from the surface of the wafer cleanly and easily. This precise process facilitates the recycling of defective or used wafers in the solar optoelectronic industry making it possible to return defective and used wafers to production. A large cathode rotation diameter provides a small gap between the anode and cathode to give a high rate of layer removal. High frequency and high power ultrasonics and a large electrolyte flow rate, high magnetic field strength from magnets that are close together, or small anode and cathode radii all increase dregs discharge and reduce the time taken to cleanly remove the composite layers of epoxy and Si_3N_4 . Dregs discharge is also improved by high speed revolution (shift) and rotation of the tool. This increased rate of discharge combined with a high continuous DC current flow results in a higher removal rate and consequently also allows a higher feed rate to be used. The study successfully demonstrates practical recycling of the defective wafers produced in the solar-cell silicon wafer process and their return to production. The proposed approach not only avoids the loss of silicon, since there is no abrasion, but also lowers costs and raises efficiency.

Acknowledgments

This study was supported by Ben Ten The Co. and by the National Science Council, Contracts 101-2221-E-152 -002 and 102-2221-E-152-005.

References

- [1] E. Mathioulakis and V. Belessiotis, "A new heat-pipe type solar domestic hot water system," *Solar Energy*, vol. 72, no. 1, pp. 13–20, 2002.
- [2] H. J. Moller, *Semiconductors for Solar Cells*, vol. 35, Artech House, Norwood, UK, 1993.
- [3] M. F. Turner, "How does your company measure up," *Black Enterprise*, vol. 32, no. 4, pp. 52–53, 2001.
- [4] A. W. Czanderna and F. J. Pern, "Encapsulation of PV modules using ethylene vinyl acetate copolymer as a pottant: a critical review," *Solar Energy Materials and Solar Cells*, vol. 43, no. 2, pp. 101–181, 1996.
- [5] E. Radziemska and P. Ostrowski, "Recycling of silicon in the PV industry," *Ecology and Technology*, vol. 17, no. 2, pp. 47–52, 2009.
- [6] R. Ewa, O. Piotr, C. Adam, and S. Mirosław, "Chemical, thermal and laser processes in recycling of photovoltaic silicon solar cells and modules," *Ecological Chemistry and Engineering S*, vol. 17, no. 3, pp. 385–391, 2010.
- [7] M. Badelt, C. Beerwald, A. Brosius, and M. Kleiner, "Process analysis of electromagnetic sheet metal forming by online-measurement and finite element simulation," in *Proceedings of the 6th International Conference on Materials Forming (ESAFORM '03)*, pp. 123–126, Salerno, Italy, 2003.
- [8] D. Wei, X. Lu, Z. Lu, and J. Gu, "Performance analysis and optimization of Organic Rankine Cycle (ORC) for waste heat recovery," *Energy Conversion and Management*, vol. 48, no. 4, pp. 1113–1119, 2007.
- [9] Y. H. Zou and T. Shinmura, "Mechanism of a magnetic field assisted finishing process using a magnet tool and magnetic particles," *Key Engineering Materials*, vol. 339, pp. 106–113, 2007.
- [10] J. Unger, M. Stiemer, B. Svendsen, and H. Blum, "Multifield modeling of electromagnetic metal forming processes," *Journal of Materials Processing Technology*, vol. 177, no. 1–3, pp. 270–273, 2006.
- [11] R. W. Wood and A. L. Loomis, "The physical and biological effects of high-frequency sound-waves of great intensity," *Philosophical Magazine*, vol. 4, no. 22, pp. 417–436, 1927.
- [12] L. D. Rozenberg, V. F. Kazemtsev, L. O. Makrov, and D. F. Yakhimovich, *Ultrasonic Cutting*, Consultants Bureau, New York, NY, USA, 1964.
- [13] B. L. Anantha Ramu, R. Krishnamurthy, and C. V. Gokularathnam, "Machining performance of toughened zirconia ceramic and cold compact alumina ceramic in ultrasonic drilling," *Journal of Mechanical Working Technology*, vol. 20, pp. 365–375, 1989.
- [14] R. Gilmore, "Ultrasonic machining: a case study," *Journal of Materials Processing Tech*, vol. 28, no. 1-2, pp. 139–148, 1991.
- [15] B. H. Amstead, F. Philip, F. Ostwald, and L. Myron, *Manufacturing Processes*, John Wiley & Sons, New York, NY, USA, 1977.
- [16] J. A. McGeough, *Principles of Electrochemical Machining*, Chapman and Hall, London, UK, 1974.
- [17] V. K. Jain and V. N. Nanda, "Analysis of taper produced in side zone during ecd," *Precision Engineering*, vol. 8, no. 1, pp. 27–33, 1986.
- [18] M. Datta and D. Landolt, "Electrochemical machining under pulsed current conditions," *Electrochimica Acta*, vol. 26, no. 7, pp. 899–907, 1981.
- [19] B. H. Kim, S. H. Ryu, D. K. Choi, and C. N. Chu, "Micro electrochemical milling," *Journal of Micromechanics and Micro-engineering*, vol. 15, no. 1, pp. 124–129, 2005.
- [20] H. Hocheng and P. S. Pa, "Continuous secondary ultrasonic electropolishing of an SKD61 cylindrical part," *International Journal of Advanced Manufacturing Technology*, vol. 21, no. 4, pp. 238–242, 2003.
- [21] P. S. Pa, "Design of effective plate-shape electrode in ultrasonic electrochemical finishing," *International Journal of Advanced Manufacturing Technology*, vol. 34, no. 1-2, pp. 70–78, 2007.
- [22] P. S. Pa, "Design of thread surface finish using ultrasonic-aid in electrochemical leveling," *International Journal of Advanced Manufacturing Technology*, vol. 36, no. 11-12, pp. 1113–1123, 2008.

- [23] P. S. Pa, "Synchronous finishing processes using a combination of grinding and electrochemical smoothing on end-turning surfaces," *International Journal of Advanced Manufacturing Technology*, vol. 40, no. 3-4, pp. 277-285, 2009.
- [24] P. S. Pa, "Continuous finishing processes using a combination of burnishing and electrochemical finishing on bore surfaces," *International Journal of Advanced Manufacturing Technology*, vol. 49, no. 1-4, pp. 147-154, 2010.
- [25] H. Xiao, *Introduction to Semiconductor Manufacturing Technology*, Prentice Hall, New York, NY, USA, 2001.
- [26] Z. J. Pei and A. Strasbaugh, "Fine grinding of silicon wafers: designed experiments," *International Journal of Machine Tools and Manufacture*, vol. 42, no. 3, pp. 395-404, 2002.
- [27] M. H. Nagel, "Environmental supply-chain management versus green procurement in the scope of a business and leadership perspective," in *Proceedings of the IEEE International Symposium on Electronics and the Environment (ISEE '00)*, pp. 219-224, San Francisco, Calif, USA, October 2000.